

# IAN: Iterated Adaptive Neighborhoods for manifold learning and dimensionality estimation

Luciano Dybala, Steven W. Zucker

August 22, 2022

## Abstract

Invoking the manifold assumption in machine learning requires knowledge of the manifold's geometry and dimension, and theory dictates how many samples are required. However, in applications data are limited, sampling may not be uniform, and manifold properties are unknown and (possibly) non-pure; this implies that neighborhoods must adapt to the local structure. We introduce an algorithm for inferring adaptive neighborhoods for data given by a similarity kernel. Starting with a locally-conservative neighborhood (Gabriel) graph, we sparsify it iteratively according to a weighted counterpart. In each step, a linear program yields minimal neighborhoods globally and a volumetric statistic reveals neighbor outliers likely to violate manifold geometry. We apply our adaptive neighborhoods to non-linear dimensionality reduction, geodesic computation and dimension estimation. A comparison against standard algorithms using, e.g.,  $k$ -nearest neighbors, demonstrates their usefulness.

# 1 Introduction

A starting point for many algorithms in data science, from clustering to manifold inference, is knowing the neighbor relationships among the data points. Clustering, for example, often begins with the “ $k$ -nearest neighbor graph,” while manifold inference involves a kernel, i.e., a measure of similarity between data points. In the first case the neighborhoods are local and discrete; in the second they are global and continuous, with concentration of influence controlled by kernel bandwidth or scale. Knowing neighbor relationships is fundamental to defining a topology. Dimensionality estimation involves the rate of change in the density of points within a ball, that is, within a neighborhood, with respect to the radius of such ball. It is helpful when the number of data points is large, a requirement that grows with dimensionality. Asymptotic analysis is often favored by theoreticians.

In practice, however, we are rarely given enough data points to satisfy asymptotic bounds, nor are we given the global number  $k$ , the precise number of neighbors each point should have. We often make the manifold assumption—that the data points are drawn randomly from on (or near) a manifold, but rarely proceed to questions about the manifold: what is its dimension, what is the probability distribution of points over it, and what is the sampling density. All of these could influence  $k$ . In practice we rarely try to assess the basic properties of the manifold assumed by theorists, e.g., its curvature, medial axis or reach (defined in the next section). Instead, we rely on different visualization algorithms, such as spectral methods, Isomap, t-SNE, or UMAP (references in the next section), to find a pleasing organization of the data. This is dangerous, of course, because these algorithms have free parameters. Central to this paper, most require specifying the number of neighbors,  $k$  (or its equivalent): changing  $k$  or the parameters changes the result. Unless one knows the answer, one is caught in a chicken-and-egg conundrum: imposing a prior belief amounts to “fixing” the solution (examples of changing  $k$  are shown later in the paper).

This gap between theory and practice shows up right from the start. If the manifold is not pure, i.e., if it consists of a union of manifolds of possibly different dimensionality, then there may be no global  $k$  that suffices; furthermore, the manifold may have a boundary. Even if it is pure and without boundary, the temptation to choose  $k$  large is common. But this can fill in the open space around curved manifolds incorrectly (“folding”), linking distant points that are not neighbors. On the other hand, choosing  $k$  small can induce holes and break connectivity; see Fig. 1. As we shall demonstrate, sampling issues and manifold geometry interact in causing such phenomena. Moreover, for real datasets the appropriate number of neighbors may differ from data point to data point. This final point is a principal motivation for this paper.

We present an algorithm to estimate the functional neighborhood—the immediate neighbors, or scale of a similarity kernel—around each point. We seek to identify those nearest neighbors that are “correct” in the sense that they support dimensionality and volume estimates, and manifold inference, without covering holes or filling in concavities. It is inspired by the philosophical position that views discrete and continuous mathematics as ‘two sides of the same,’ as argued by Lovász ([75]), and iterates between them.

Our algorithm builds from a conservative initial estimate of neighbors (based a discrete construct, the Gabriel graph) to a more refined one, based on continuous estimates from a Gaussian kernel. The discrete and continuous volume estimates must be consistent, however, and this provides the glue for our iteration. Since not all of the initial “closest” neighbors are actually closest

neighbors, those putative neighbors that violate the volume relationship are pruned, and the process repeats until the two perspectives agree. Our algorithm, then, can be considered an iterative graph sparsification. Technically, it involves two different graphs: a discrete one, that links only putative nearest neighbors (pairs of points defining the diameter of an otherwise empty ball), and a weighted one, structured by a multi-scale Gaussian kernel, whose individual scales must cover the neighborhood given in the discrete graph. Keeping the two graphs consistent is another way to think about our iteration. Each resulting graph can be applied to many different algorithms for data visualization, dimensionality reduction, and manifold inference.

Our approach to the problem is in the spirit of *exploratory data analysis*; it works with the available data. This provides another view regarding the interaction between sampling and geometry: one can only do as well as the available data allow; see Fig. 2. The situation is analogous to that in learning theory, where there is a trade-off between the accuracy of the learner and the coarseness of the hypothesis class over which she is learning [2]. Here, the space of manifolds over which inferences are made is dictated by the available samples.

An overview of the paper is as follows. In the next section we review the background in some detail, covering both the zoo of similarity kernels that exist in the literature plus several relevant tutorial notions, such as manifold reach, that are well studied in the theory literature. The discussion is organized to emphasize the centrality of scale, or neighborhood, in all of these papers. In Sec. 3 we provide an overview of our algorithm. It includes a brief sketch of both the two graphs with which we work, plus the connection back to manifolds. Pseudocode for the algorithm is given in 1, which also includes pointers to where those functions are developed.

We then expand on the algorithm. In Sec 3.3 we study the Gabriel graph and putative neighbors. Two features are emphasized: scale-free neighborhoods and the relationship between node degree and local dimensionality. A structural criterion is revealed, showing how putative edges between neighbors "fill volumes" that block others from being neighbors. This graph serves as an initialization. It is refined iteratively in several steps. First, continuous scales are computed from the discrete, putative ones; these continuous scales are then related to kernel scales. A linear program relaxation bridges local scales to a global cover, in which each node's weighted degree is comparable to the number of its neighbors. In other words, each neighborhood radius should not cover too many outside points. If it does, then it indicates that the neighborhood itself should be refined. That is, some putative scales are likely wrong, in the sense that their neighborhood contains an extreme outlier. This leads directly to a volumetric statistic (Sec. 3.5.1, and to a pruning technique for sparsifying the discrete graph. The process iterates until there are no outliers to sparsify. In the end both the discrete neighborhood graph, the continuous weighted graph and the scale associated with each node are returned.

Since the paper is largely algorithmic, we evaluate the results for estimating manifold dimension, geodesics, and low-dimensional embeddings. Comparisons against standard algorithms, such as UMAP and t-SNE, illustrate the power of the approach. In the end we demonstrate that it is possible to infer local scales from data given by similarity kernels that remain consistent with geometric and topological properties of manifolds.

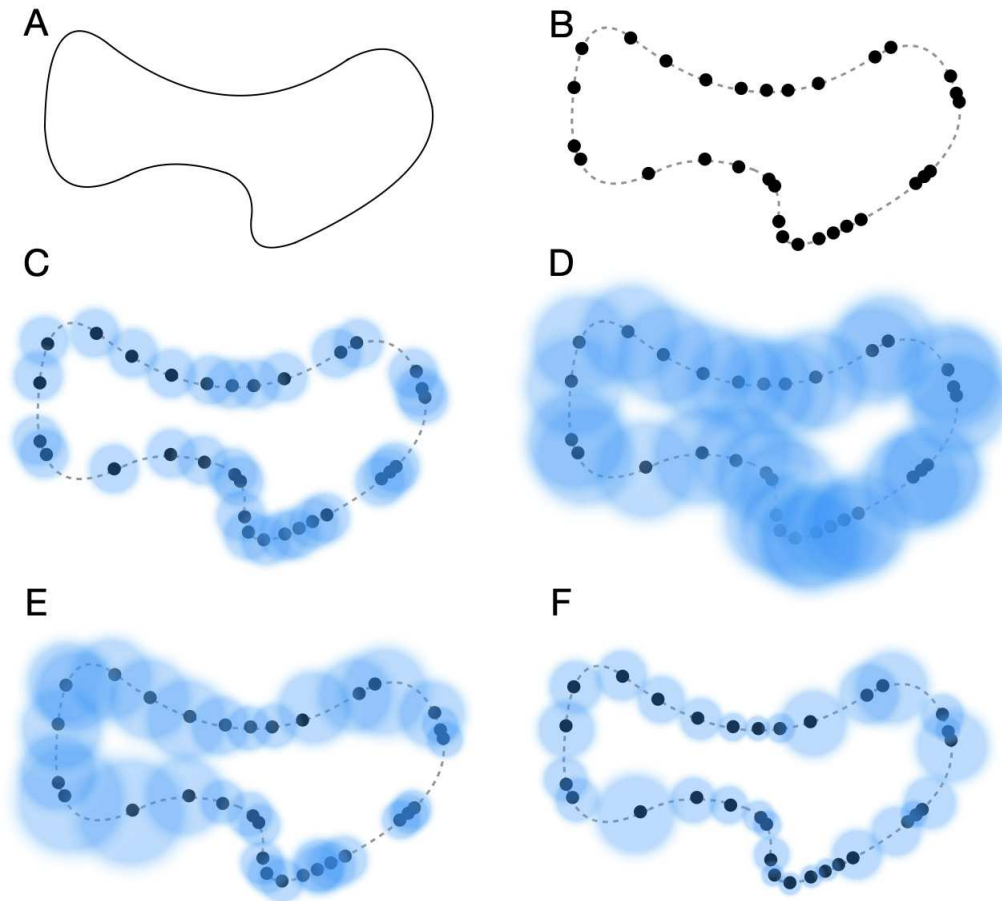


Figure 1: Inferring the geometry of manifolds requires neighborhoods around each given data point. Getting the scale for these neighborhoods, shown as balls, is fundamental. **(A)** Example of a one-dimensional manifold,  $\mathcal{M}$ . **(B)** Collection of points sampled from an unknown distribution over  $\mathcal{M}$ . Their pairwise distances are the only available data; properties of  $\mathcal{M}$  are not given *a priori*. **(C–D)** Using a global kernel scale: if it is too small (left), the manifold will appear disconnected, artificially producing clusters (poor sampling, good reach); notice how some balls do not touch. If too big (right), the manifold may collapse giving rise to incorrect geometry/topology (good sampling, poor reach). Notice how the balls overlap (covering dimension). **(E)** The use of local scales based on a global number of nearest neighbors (in this example,  $k = 2$ ) is still susceptible to the problems above. **(F)** Our approach computes locally adaptive neighborhood sizes, resulting in scales that conform to the local geometry and sampling.

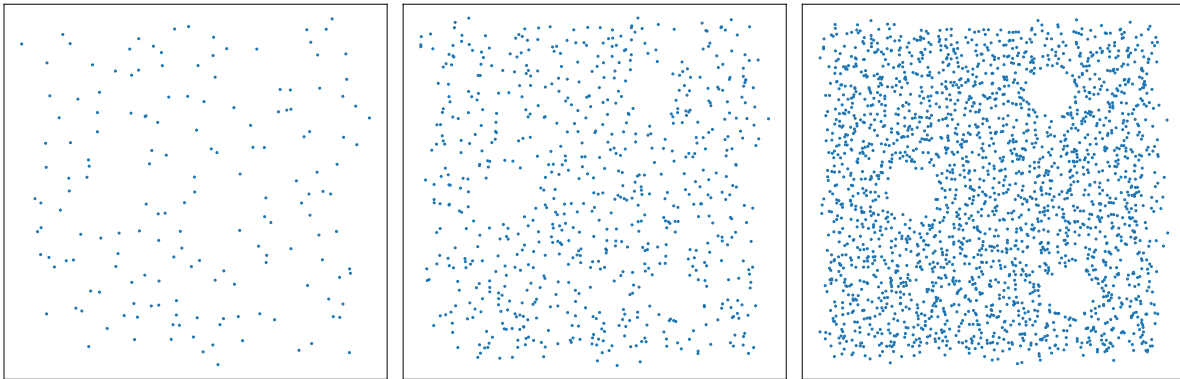


Figure 2: The available data constrain manifold complexity: *sampling Swiss cheese*. Viewed from left to right, as the number of sample points increases, the apparent manifold goes from a plane to a plane with holes. The central panel indicates roughly where the holes in the manifold become distinguishable from holes due to sampling. The result of our algorithm on these examples is shown in Fig. 23.

## 2 Background

Manifold learning is a vast area of machine learning in which high-dimensional data are analyzed based on the assumption that the data were sampled from a low-dimensional manifold  $\mathcal{M}$  [44], i.e., when geodesic distances over  $\mathcal{M}$  provide a better description of the relationships between data points than Euclidean distances in ambient space [11]. The manifold assumption finds applications in non-linear dimensionality reduction [102], de-noising[57], interpolation[23], dimensionality estimation[25], computational geometry [33], and many others.

Since  $\mathcal{M}$  locally resembles Euclidean space, it is standard to define a similarity kernel to define (possibly weighted) neighborhoods around each point  $\mathbf{x}_i$  in terms of other points. This naturally leads to a graph having data points as nodes and similarity values as edge weights. Then, computing the graph Laplacian, one can apply a variety of methods from spectral graph theory[94]. Formal analysis involves the limit as the number of data points grows large; the practical success of such methods on real samples depends on how well graph neighborhoods capture the topology and geometry of  $\mathcal{M}$ .

We here review the many approaches to specifying a kernel or a local neighborhood. We work with a  $d$ -dimensional manifold  $\mathcal{M}$  in ambient space  $\mathbb{R}^n$ . When only pairwise distances are known, an intuitive approach is to define the neighbors of a point  $\mathbf{x}_i$  as those within a certain distance threshold, or, equivalently, inside an  $n$ -dimensional ball around  $\mathbf{x}_i$ . A kernel function assumes the role of this “ball,” by assigning values to neighboring points as a function (discrete or continuous) of how close they are to  $\mathbf{x}_i$ . The question becomes: what kernel sizes should be used for each point?

### 2.1 Similarity kernel

Consider a set of points  $\mathcal{X} \in \mathbb{R}^n$ . Typically, a symmetric, positive semi-definite similarity kernel is chosen to determine weighted connections between data points based on the ambient Euclidean distances between them. For each pair of data points  $\mathbf{x}_i, \mathbf{x}_j \in \mathbb{R}^n$ , it returns a number between 0 and 1 which determines how close, or strongly connected, they are. This effectively defines a neighborhood around each point.

#### 2.1.1 Discrete kernels

Possibly the simplest choice for a kernel is the  $\varepsilon$ -neighborhood[10]:

$$K_{ij}(\varepsilon) = \begin{cases} 1, & \text{if } \|\mathbf{x}_i - \mathbf{x}_j\| < \varepsilon \\ 0, & \text{otherwise.} \end{cases} \quad (1)$$

This results in discrete-like neighborhoods whose sizes may be quite sensitive to the choice of  $\varepsilon$ , so implicit is the assumption that sampling is approximately uniform.

Instead of defining a neighborhood radius, a more common approach is to specify the number of neighboring points,  $k$ . Letting  $\mathcal{N}_k(\mathbf{x}_i)$  be the set containing the  $k$  points closest to  $\mathbf{x}_i$  in  $\mathbb{R}^n$  (not

including  $\mathbf{x}_i^1$ ), a  $k$ -nearest-neighbor kernel can be defined as:

$$K_{ij}(k) = \begin{cases} 1, & \text{if } \mathbf{x}_j \in \mathcal{N}_k(\mathbf{x}_i) \\ 0, & \text{otherwise.} \end{cases} \quad (2)$$

which is commonly symmetrized by making  $K_{ij}(k) = 1$  if  $\mathbf{x}_j \in \mathcal{N}_k(\mathbf{x}_i) \vee \mathbf{x}_i \in \mathcal{N}_k(\mathbf{x}_j)$ .

### 2.1.2 Continuous kernels – global scale

To have the kernel values decrease with increasing distance between data points, a Gaussian kernel is frequently used:

$$K_{ij}(\sigma) = \exp\left(\frac{-\|\mathbf{x}_i - \mathbf{x}_j\|^2}{\sigma^2}\right), \quad (3)$$

where  $\|\cdot\|$  is the Euclidean norm in  $\mathbb{R}^n$ . This gives a continuous similarity scale from 1 (when  $\mathbf{x}_i$  and  $\mathbf{x}_j$  are identical) down to some predetermined cutoff below which the kernel is considered to be zero (meaning no connection in the data graph). Such a threshold is typically chosen due to be a very small value, often at the limit of numerical precision, and is required to ensure compactness of the kernel.

One would like  $\sigma$  to be just large enough to be able to capture local manifold patches. There are several heuristics for finding such a scale: the median of all pairwise distances in  $\mathcal{X}$  (or another percentile), the mean (or median) of the distances to each point's  $k^{\text{th}}$  nearest neighbor [67], or a multiple of the maximal distance from a point to its nearest neighbor in the data [60]. Also common is to choose a scale so that each data point is sufficiently connected to at least one other point[68].

A different approach is based on inspection of the curve given by the sum of pairwise kernel values [31]. When the double-sum  $\sum_{i,j} K_{ij}(\sigma)$  is plotted against  $\sigma$  on a log-log scale, the slope

$$\frac{d \log \sum_{i,j} K_{ij}(\sigma)}{d \log \sigma} \quad (4)$$

is proportional to the intrinsic dimensionality of the data. A global scale is then chosen from within a linear region of such curve.

In [53], a similar procedure is proposed that considers, instead, the curve given by the weighted average of the degrees  $Z_i(\sigma)$  (i.e. sums of kernel values  $K_{ij}$ ) of each data point, after taking the logarithm:

$$\langle \log Z_i(\sigma) \rangle = \frac{\sum_i \log Z_i(\sigma) \cdot (1/Z_i(\sigma))}{\sum_i (1/Z_i(\sigma))}, \quad (5)$$

where  $Z_i(\sigma)$  is the degree of  $\mathbf{x}_i$ . This weighted average (using the inverse of each point's degree as weights) is intended to compensate for density heterogeneities. The choice of  $\sigma$  is then made precise by choosing the argmax of the slope of  $\langle \log Z_i(\sigma) \rangle$  plotted against  $\log \sigma$ , which in many cases should occur near the center of the linear region of eq. 4. One complication occurring in both approaches, however, is that more than one linear section may exist (and, equivalently, more than one local maximum of the slope), requiring that additional criteria be defined to make the choice of  $\sigma$  truly automated.

---

<sup>1</sup>Throughout, when referring to a point's set of  $k$ -nearest neighbors we will not include the point itself, unless otherwise stated, and further assume that no two points are identical.

### 2.1.3 Continuous kernels – multi-scale

A more localized strategy is a *multi-scale* kernel, where each point has an individual scale or bandwidth. Instead of a single, global scale, there are now  $N$  parameters, which has the advantage that, if the scale selection were adequate, the kernel could capture the characteristics of more complex datasets and manifolds (i.e., non-uniform sampling and geometry).

In the self-tuning method [111], the local scales are used in a Gaussian kernel by replacing the global scale  $\sigma$  in eq. 3 by  $\sqrt{\sigma_i \sigma_j}$ , where  $\sigma_i$  and  $\sigma_j$  are the scales assigned to  $\mathbf{x}_i$  and  $\mathbf{x}_j$ , respectively. This results in the symmetric kernel

$$K_{ij}(\sigma) = \exp\left(\frac{-\|\mathbf{x}_i - \mathbf{x}_j\|^2}{\sigma_i \sigma_j}\right), \quad (6)$$

Each scale  $\sigma_i$  is commonly set to be the distance to the  $k^{\text{th}}$  nearest neighbor of  $\mathbf{x}_i$ , using  $k = 7$  [111, 80].

In [16, 17], a multi-scale kernel was proposed that combines the use of local bandwidths with a global scale parameter  $\epsilon$ . The kernel then takes the form:

$$K_\epsilon(\mathbf{x}_i, \mathbf{x}_j) = \exp\left(\frac{-\|\mathbf{x}_i - \mathbf{x}_j\|^2}{4\epsilon(q_\epsilon(\mathbf{x}_i)q_\epsilon(\mathbf{x}_j))^\beta}\right), \quad (7)$$

where  $q_\epsilon$  is a local density function and  $\beta$  an additional (non-positive) parameter. An initial estimate for the local bandwidth around each point  $\mathbf{x}_i$  is set as the square-root of the mean squared distance to the  $k$ -nearest neighbors of  $\mathbf{x}_i$ , with  $k = 8$ . Finally,  $\epsilon$  is automatically tuned as the argmax of eq. 4 from [31]; however, the authors do not consider cases in which than one local maximum may exist.

Other methods also adopt individual bandwidth parameters, but use asymmetric kernels that are symmetrized *a posteriori*. In t-SNE [101], the single-scale Gaussian kernel

$$K_{ij}(\sigma_i) = \exp\left(\frac{-\|\mathbf{x}_i - \mathbf{x}_j\|^2}{2\sigma_i^2}\right) \quad (8)$$

gives a measure of affinity, or similarity, between pairs of points. It is then normalized as

$$p_{j|i}(\sigma_i) = \frac{K_{ij}(\sigma_i)}{\sum_{k \neq i} K_{ik}(\sigma_i)} \quad (9)$$

to yield transition probabilities, and finally symmetrized as

$$p_{ij}(\sigma_i, \sigma_j) = \frac{1}{2N} (p_{j|i}(\sigma_i) + p_{i|j}(\sigma_j)), \quad (10)$$

Each  $\sigma_i$  is fit to  $\mathbf{x}_i$  so that the distribution of  $p_{j|i}, \forall j$  attains entropy  $H_i$  such that its perplexity,  $2^{H_i}$  (a real-valued number representing the ‘effective number of neighbors’), approximates some prespecified value  $k$ . The authors recommend a value for  $k$  between 5 and 50.



In UMAP[78], an exponential kernel is used instead of the typical Gaussian. Using a prespecified neighborhood size  $k$ , let  $\mathcal{N}_k(i)$  be the set of  $k$ -nearest neighbors of  $\mathbf{x}_i$ . With  $\rho_i$  the distance to the nearest neighbor of  $\mathbf{x}_i$ , the kernel has the form

$$K_{ij}(\sigma_i) = \exp\left(\frac{-\max\{0, \|\mathbf{x}_i - \mathbf{x}_j\| - \rho_i\}}{\sigma_i}\right), j \in \mathcal{N}_k(i), \quad (11)$$

and is symmetrized as

$$U_{ij}(\sigma_i, \sigma_j) = K_{ij}(\sigma_i) + K_{ji}(\sigma_j) - K_{ij}(\sigma_i)K_{ji}(\sigma_j), \quad (12)$$

so it can be seen as a hybrid between continuous and discrete, since  $U_{il}$  is set to zero for any point  $l$  not in  $\mathcal{N}_k(i)$ . Each  $\sigma_i$  is fit to  $\mathbf{x}_i$  so that  $\sum_j K_{ij}(\sigma_i)$  approximates  $\log_2 k$  (in some sense analogous to the perplexity approach from t-SNE).

### 2.1.4 Adaptive neighborhood size methods

A different class of methods attempt to automatically find optimal neighborhoods. Most of these are based on determining an optimal  $k$  for a  $k$ -nearest neighbors ( $k$ -NN) graph; this can be done either globally or by selecting a local neighborhood size  $k_i$  around each point  $\mathbf{x}_i$  (adaptive neighborhood selection [102]).

Some approaches optimize a global  $k$  based on its performance in a specific embedding algorithm. E.g., [92] is tailored to Isomap[96] and [66, 3] to LLE[89]. In [3], a local method is additionally proposed that produces a nearest-neighbor graph with variable  $k_i$ , under the assumption that the manifold is connected.

Others are based on estimating the local tangent space around each point, then setting  $k_i$  to include as neighbors those points that are close to it. Such methods include [79] and [106], and require positional information for the tangent space computation (usually via SVD).

Also available are methods that are not based on the nearest-neighbors concept. In computational geometry, the idea of refining an initial estimate of connectivity from a simplicial mesh has been used before, usually specific to the case when  $d = 2$  and  $n = 3$  (surfaces in 3-D space) [4, 5, 14, 12]. Other approaches extend this idea to arbitrary dimensionality (e.g., [19, 13], but still require knowledge of  $d$ . Most of the algorithms in this class use point clouds as input, so they can exploit positional information to decide on the appropriate neighborhood/connectivity.

Among these myriad ways of estimating neighborhoods, there is little agreement on which is most successful (see [72] for a review). Before proceeding to our algorithm, then, it is helpful to first understand what makes this such a hard problem. How can it fail, and what requirements must it fulfill in order to properly capture the topology and geometry of  $\mathcal{M}$ ? This brings us to the geometry of manifolds.

## 2.2 Reach and the geometry of manifolds

The neighborhoods implied by a kernel should agree with  $\mathcal{M}$ , or at least approximate a tubular neighborhood of it. As we showed (Fig. 1), if neighborhoods are too small, the implied manifold may be disconnected (i.e., falsely divided into disjoint sub-manifolds, or clusters[92]); if too large, they may cause  $\mathcal{M}$  to self-intersect, to collapse “bottlenecks” or curved regions, or cause

“smoothing,” or “folding.” Such shortcomings are well-known in the manifold inference literature—while the former case typically occurs due to non-uniform sampling, the latter is mainly caused by an incompatibility between the sampling rate and the *reach*, or condition number, of  $\mathcal{M}$  [42, 97]. We now expand these points.

Letting the *medial axis* of  $\mathcal{M}$  be the set of points in  $\mathbb{R}^n$  with at least two closest points in  $\mathcal{M}$ , the reach  $\tau$  can be defined as the minimum distance from  $\mathcal{M}$  to its medial axis. Locally, it is constrained by the minimal radius of curvature (i.e., maximal curvature of a geodesic though  $\mathcal{M}$ ); globally, it is constrained by presence of bottlenecks (Fig. 3). The reach encodes essential geometric properties of  $\mathcal{M}$ , and has been widely used in the manifold learning community [83, 84, 1, 74, 4, 50, 43, 20, 19, 12]. It approximates the size of the largest ball in ambient  $\mathbb{R}^n$  such that points in  $\mathcal{M}$  can be seen as lying in Euclidean space  $\mathbb{R}^d$  [18]. A related concept, the *local feature size* of a point  $\mathbf{x}_i \in \mathcal{M}$ , is the smallest distance between  $\mathbf{x}_i$  and the medial axis of  $\mathcal{M}$ , so  $\tau$  can be seen as the infimum of the local feature size anywhere on  $\mathcal{M}$ . [13]

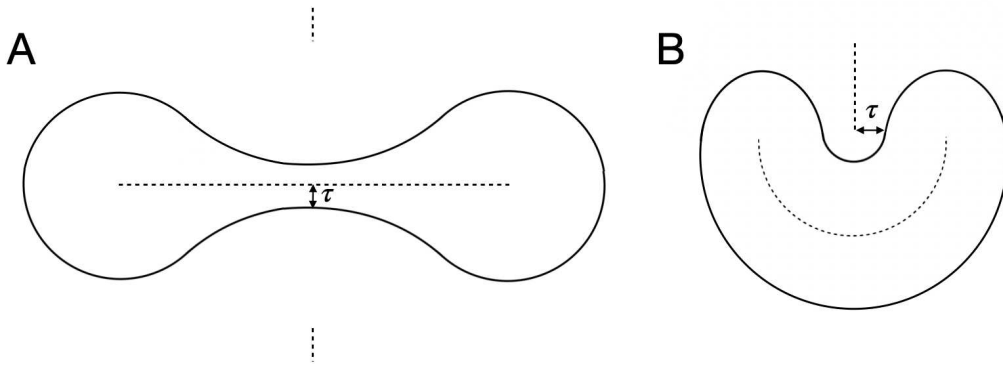


Figure 3: The reach,  $\tau$  is a measure of the shape of a manifold. **(A)** A 1-dimensional manifold  $\mathcal{M}$  with a bottleneck; the reach (double arrow) is the smallest distance between  $\mathcal{M}$  and its medial axis (dashed curve). **(B)** A highly curved manifold; now the reach indicates the high curvature region.

When  $\tau$  is positive, it provides a measure of the “local distortion” [18]; the larger it is, the easier inference becomes. Some authors, e.g. [82, 44], assume large reach in order to test the manifold hypothesis and to find bounds on the required sample size. In [18], the reach is used when establishing bounds on the quality of an intrinsic dimensionality estimation based on  $k$ -nearest neighbors.

Obtaining a good representation of  $\mathcal{M}$ , therefore, requires consideration of its reach. In terms of our problem of finding an appropriate neighborhood kernel, this effectively means that no edge segment  $\ell_{ij}$  between two points  $\mathbf{x}_i$  and  $\mathbf{x}_j$  that are considered neighbors should cross the medial axis of  $\mathcal{M}$ .

Sampling is a further complication, and essentially what makes this a hard problem—when it is nonuniform and sparse (common in real-life datasets), it is not always clear whether the space between points constitutes an undersampled piece of  $\mathcal{M}$ , a hole, or a gap between disjoint sub-manifolds (cf. Fig. 2). The latter two conditions, of course, relate to reach. Narayanan et al. [82] prove that the number of required samples depends polynomially on the curvature, exponentially on intrinsic dimension, and linearly on intrinsic volume. Aspects of our algorithm address each of these during the iteration process.

In all such cases, choosing a globally-fixed radius is likely to be problematic. While defining neighborhood size based on a fixed number  $k$  of neighbors can be helpful to deal with nonuniform density (since the neighborhood radius adapts to the local pairwise distances), it is bound to violate the reach if  $k$  is too large. It will also be a problem when the intrinsic dimensionality is not constant throughout  $\mathcal{M}$ , as higher dimensions require exponentially more neighbors.

The authors in [79] point out the lack of a principled way for setting this parameter, which in practice is often tuned empirically based on prior knowledge of the desired output. As put by [106], the effectiveness of manifold learning algorithms depends on how nearby neighborhoods overlap and on the interplay between the curvature of the manifold and sampling density.

In terms relevant to this paper, the kernel's neighborhood radius should be smaller than the local feature size, but large enough to account for sampling variability and local dimensionality. We propose an iterative approach to developing the kernel, so that it can adapt appropriately to the neighborhood characteristics around each point.

### 3 The algorithm

We here overview our algorithm for finding the neighborhood scale around each point in a manner that makes it globally consistent as a covering of the data points. As is common in ML, we start with the distance matrix between data points, not the points themselves. This distance matrix normally derives from a kernel. The first step is to build a graph in which each datum is connected to an appropriate neighborhood of other data points. This data graph defines a topology; in the end we refer to it as the *neighborhood graph*. As we reviewed above, in the discrete case one might choose  $k$ -nearest neighbors, while in the continuous kernel case there is a bandwidth parameter that effectively defines a “ball of influence” around each point. *Scale* is the radius of that ball; a level set of the kernel function that essentially contains those neighbors whose weights are non-trivial. Our goal, then, is to find those scales – or that neighborhood graph – that support non-linear dimensionality reduction, geodesic estimation and, in general, manifold inference algorithms from the given distances. We do not have sampling guarantees, so will develop a statistic to check whether reach and curvature constraints might be violated.

#### 3.1 Subtleties of Scale

Since scale may not be constant across the data set, we argue that it should be the first property to infer from the data. We start by imposing the manifold assumption, but from an empirical perspective. Unlike most theoretical studies, we do not assume the manifold is pure—i.e., has constant dimension. In a simple case, the data may be drawn from a union of different manifolds, whose dimensions are not known *a priori* (such datasets have been considered infrequently, although exceptions exist, e.g., [54, 74]). Second, we do not know the sampling rate, or density. Rather, we build it up, conservatively, with putative nearest neighbors to each data point, by imposing a necessary (but not sufficient) condition. These putative neighbors will be refined as the algorithm iterates, to achieve sufficiency. While the manifold assumption does imply the existence of local neighborhoods, their size may vary over the dataset; we require that the sampling be nearly constant over each of them. In effect the density of points must be determined locally while respecting the global manifold geometry.

We illustrate the complexity of this situation in Fig. 4. Shown is a data sphere with an apparent spike emerging from it. On one hand, such complex datasets could derive from two unrelated systems, which only appear to connect through their embeddings. On the other hand, the data could derive from a non-linear system that includes two regimes, one responsible for the spherical data and the other for the spike. To handle the first situation, we must allow datasets to consist of unions of manifolds. This suggests the interpretation in Fig. 4(b), where the separation is obscured by sampling. Since manifolds with boundary and high curvature are also possible, the situation in Fig. 4(c) arises. Here there is an apparent change in *intrinsic dimension* due to the small reach in the spike and the large boundary curvature. Because the (2-D) spike is so narrow, sampling suggests it is 1-dimensional while the bulk of the points derive from a 2-D manifold.

We submit that such situations occur in real datasets and, since the data are fixed, we cannot appeal to knowing the sampling density or the manifold dimensions and reach. Instead we address the interplay between manifold reach and sampling density pragmatically. “Standing” on the spike, the data appear to be 1-D; on the ball, 2-D. We seek a neighborhood graph that supports these inferences, so “most” points enjoy a neighborhood that agrees with their apparent dimension. At

the join, or the high-curvature neck, it is unclear. Moving from the spike to the ball suggests that dimension should be increasing; from the ball to the spike it should be decreasing. For the neighborhood graph, most points along the spike should see  $\sim 2$  neighbors, and most points in the ball should see  $\sim 4$  neighbors; the problematic points should see something intermediate. Such results will be shown to follow from our algorithm.

We claim that either of the alternatives is worse; one should not impose an apparent dimensionality (or connectivity in the neighborhood graph) globally. To wit, if small numbers of neighbors (appropriate for the spike) are enforced on the ball, then holes are likely to be introduced. Or if too many neighbors are enforced on the spike, it will collapse on itself. (These situations are illustrated later, in Fig. 25.) Both change the topology drastically.

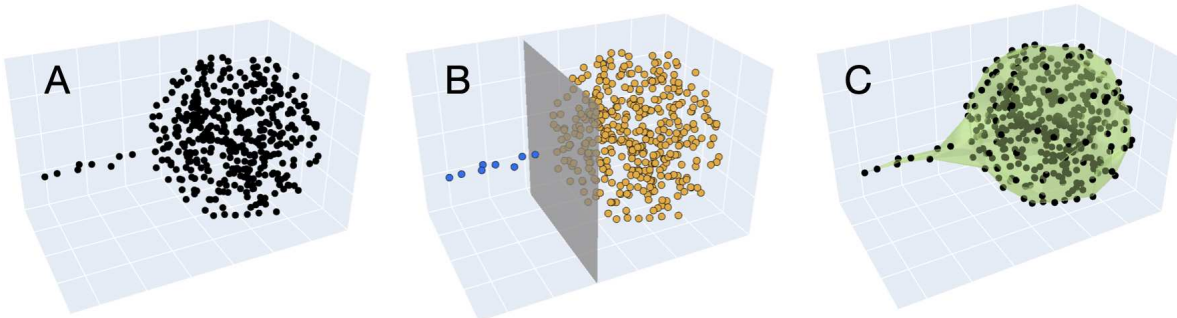


Figure 4: The ‘manifold’ subtleties of complex datasets. **(A)** A sampled data from a non-linear system that includes two regimes. **(B)** It may be the case that the data in each regime define a manifold, and they are actually separate (indicated by the plane). After sampling, however, the evidence for the plane is absent. **(C)** Or the data may be drawn from a single, connected manifold whose geometric properties change rapidly.

### 3.2 Overview of algorithm

Notation: Let the dataset  $\mathcal{X}$  be a sampling of a (possibly non-pure) manifold  $\mathcal{M} = \cup_{\alpha} \mathcal{M}_{\alpha}$ , with  $\dim \mathcal{M}_{\alpha} = d_{\alpha}$ . The dataset  $\mathcal{X}$  consists of  $N$  points  $\mathbf{x}_i$  in the ambient space  $\mathbb{R}^n$ ,  $n > d_{\alpha}, \forall \alpha$ . The manifold may have a boundary. The number of components,  $\alpha$ , is not known a priori.

We work with two graphs, the first unweighted and the second with edge weights given by a kernel. Denote the (unweighted) graph  $G = (V, E)$  with  $|V| = N$  and adjacency matrix  $A$  with entries  $a_{ij}$ , where to each point  $\mathbf{x}_i$  is associated a node  $i \in V$ . We begin with a conservative estimate of  $G^{(0)}$ ; successive refinements are indicated  $G^{(t)}$  until convergence ( $G^{*}$ ).

Our strategy: after obtaining a coarse initial estimate of the discrete neighbor graph, we extend it to a global weighted graph that suggests an estimated manifold covering. The validity of this extension is evaluated by a measure of volume in both graphs; an iterative algorithm to estimate local scales for each point  $\mathbf{x}_i$ . Before presenting the algorithm, we introduce the two graphs.

Since we seek a scale for each data point, we work with a multi-scale Gaussian similarity kernel defined as in Sec. 2.1:

$$K_{ij} = \exp\left(\frac{-\|\mathbf{x}_i - \mathbf{x}_j\|^2}{\sigma_i \sigma_j}\right). \quad (13)$$

The kernel value  $K_{ij}$  is therefore symmetric and equivalent to that of a traditional Gaussian kernel using the geometric mean of  $\sigma_i$  and  $\sigma_j$  as its scale or bandwidth. Notice, in particular, how the scales and the kernel values are coupled: setting the scale incorrectly could make distant points  $\mathbf{x}_i$  and  $\mathbf{x}_j$  appear close in similarity.

Given a set of individual point scales  $\sigma_i$  (sometimes collected into the vector  $\boldsymbol{\sigma} \in \mathbb{R}^N$ ), we define a second, weighted graph  $\mathcal{G} = (V, \mathcal{E}, W)$  as the complete graph on all pairs of data points in  $\mathcal{X}$ . Its weighted adjacency matrix,  $W$ , has entries  $w_{ij} = K_{ij}$ . While the unweighted graph will be related to nearest neighbors and computational geometry, the weighted graph will be related to spectral methods on manifold inference. In particular, we expect the Laplacian of  $\mathcal{G}$  to approximate the Laplace-Beltrami operator on  $\mathcal{M}$ , subject to the number of data points and their sampling.

The algorithm is initialized by computing a coarse estimate of  $G$ . As described in section 3.3, this is achieved by exploiting the geometry of medial balls between pairs of points to produce a *Gabriel graph* [49, 77]. The main advantages of the Gabriel graph as a starting point are: (i) it is scale invariant, so a prespecified  $\varepsilon$ -neighborhood (eq. 1) is not required; and (ii) neither are neighborhoods determined by a number  $k_i$  of nearest neighbors, which allows for connections to “jump across” sampling gaps while keeping the data graph sparse.

However, as described above, obtaining a good inference of  $\mathcal{M}$  really means finding reasonable estimates of its reach. For that to occur, no edge segment  $\ell_{ij}$  between any two points  $\mathbf{x}_i$  and  $\mathbf{x}_j$  should cross a medial axis of  $\mathcal{M}$ . As the examples that follow will show, there are several cases in which the Gabriel graph will violate this. Therefore, additional steps are necessary to refine it. The Gabriel graph provides a necessary condition (all the correct connections are present, but possibly others as well); the refinement moves toward sufficiency.

In order to estimate  $\mathcal{G}$ —the weighted counterpart of  $G$ —we will use the weights that are obtained by applying a continuous kernel over the points in  $\mathcal{X}$ . Such a kernel requires scales, or bandwidths,  $\boldsymbol{\sigma}$  that must be estimated from  $G$ . These will be obtained from an optimization procedure that finds the smallest such scales that ensure all discrete edges have a minimum kernel value as weight. At this point, a weighted graph  $\mathcal{G}$  can be obtained from  $\boldsymbol{\sigma}$ .

At this point it is helpful to articulate the geometry more carefully; see Fig. 5, which illustrates how the discrete connectivity relates to the manifold geometry. In particular, for a real dataset, the few closest points surrounding  $\mathbf{x}_i$  are the best candidates for ‘nearest’ neighbors—this is all that can be asserted locally. Now, let  $\mathbf{p}_i$  and  $\mathbf{p}_j$  be the projections of  $\mathbf{x}_i$  and  $\mathbf{x}_j$  onto  $\mathcal{M}$ , respectively. If the sampling is  $\|\mathbf{p}_i - \mathbf{p}_j\|_{\mathbb{R}^n}$ -dense in  $\mathcal{M}$  between  $\mathbf{x}_i$  and  $\mathbf{x}_j$ —again, all that we can assume from our limited initial information—then there should be a geodesic between  $\mathbf{p}_i$  and  $\mathbf{p}_j$ . By further assuming  $\mathbf{x}_i \in \mathcal{M}, \forall i$  or at least that  $\|\mathbf{x}_i - \mathcal{M}\|_{\mathbb{R}^n} < \delta, \forall i$ , then  $\|\mathbf{x}_i - \mathbf{x}_j\|_{\mathbb{R}^n}$  approximates the geodesic when the curvature between  $\mathbf{p}_i$  and  $\mathbf{p}_j$  is small. Equivalently, the line segment  $\ell_{ij}$  between  $\mathbf{x}_i$  and  $\mathbf{x}_j$  lies on the tangent space  $T_p\mathcal{M}$ , where  $p$  is the midpoint between  $\mathbf{x}_i$  and  $\mathbf{x}_j$ ; see Fig. 5.

Such an “edge-centric” approach connects differential geometry to the underlying graph. In effect, we are assuming that each node  $i$  and its neighbors in  $G$  all lie near the tangent space around  $\mathbf{x}_i$ . This is shown in Fig. 5 where the kernel values are shown shading in the tangent plane. Notice how the point  $\mathbf{x}_i$  and neighbor  $\mathbf{x}_j$  both fall under the bright kernel values; i.e., they are very similar (in this measure) to each other. Stated in geometric terms, we assume that the neighbors all lie within the *injectivity radius* around  $\mathbf{x}_i$ . We will show (Fig. 14) that the value of a multi-scale kernel between two data points is equivalent to that of a rescaled kernel centered at the midpoint between those two points.

Now, the optimized scales can in turn be used to evaluate the current approximation and iden-

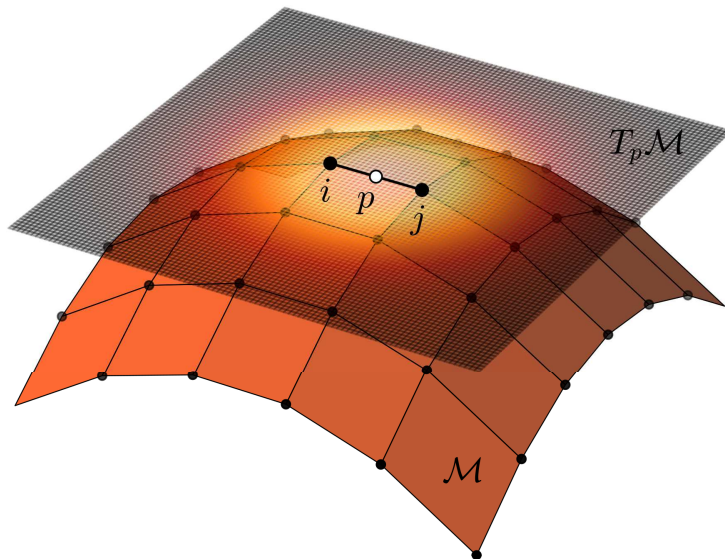


Figure 5: Relating the discrete neighborhood graph to the manifold geometry. Nearby sampled points ( $x_i$  and  $x_j$ ) on a patch of manifold  $\mathcal{M}$  lie in (or near) the tangent plane  $T_p\mathcal{M}$  to the midpoint ( $\mathbf{p}$ ). Line segments (edges) between neighboring points lift, via the exponential map, to geodesics in  $\mathcal{M}$ . The continuous kernel extends this discrete relationship to the full tangent plane. The values of the kernel centered at  $\mathbf{p}$  are shown as shading, which extends in every direction in the tangent plane. Our algorithm shall enforce this relationship; i.e., the consistency between large values of the kernel and the discrete edges.

tify the edges in  $G$  that are “too expensive;” i.e., are likely violating reach. We proceed by computing successive refinements of both  $G$  and  $\sigma$  in an iterative manner, until no further change is observed. We then return the final version of the discrete and weighted graphs (denoted  $G^*$  and  $\mathcal{G}^*$ , respectively).

One can view the computation of  $\mathcal{G}$  as a relaxation of the discrete connectivity in  $G$ . In fact, as we shall see in section 3.5, a relaxation statistic,  $\delta'_i$ , will be used to prune discrete edges that produce a poor approximation. More specifically, when a node  $i$  with degree  $\deg(i)$  in  $G$  has  $\delta'_i$  close to 1, it means  $i$  has retained the same degree in  $\mathcal{G}$ , only continuously spread as a Gaussian around it.

Each of the steps above are listed in Algorithm 1 and will be described in detail. We begin with the discrete connectivity rule (Gabriel graph); then the scale optimization is developed, followed

by the edge-pruning step. Fig. 6 illustrates the action of our algorithm on datasets for which the Gabriel graph alone cannot infer a good approximation of the manifold connectivity.

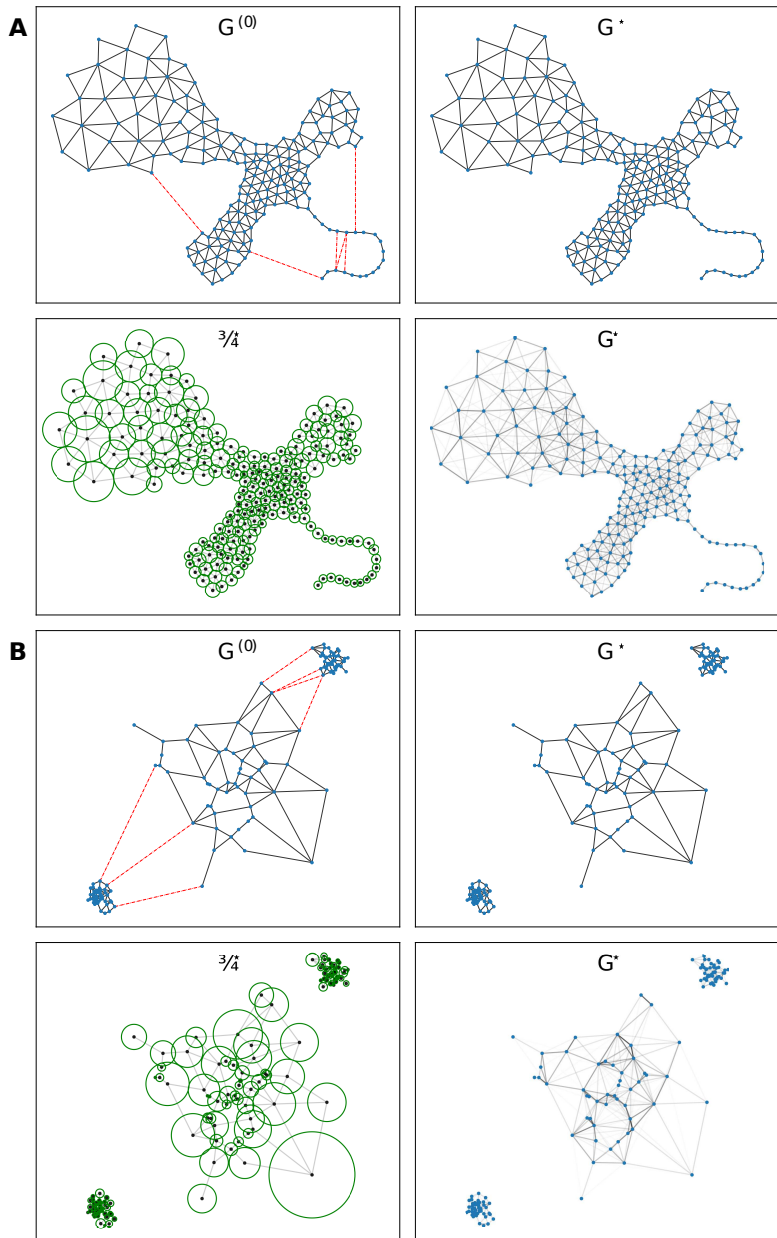


Figure 6: Steps of Algorithm 1 on toy datasets with various challenges. **(A)** Dataset with several challenges: non-uniform density, non-uniform dimensionality, and high curvature. After pruning 6 edges (dashed red lines) from the original Gabriel graph ( $G^{(0)}$ ) the algorithm converges, inferring reasonable discrete neighborhoods ( $G^*$ ); the optimal scales  $\sigma^*$  produce a weighted graph  $G^*$  whose connectivity closely approximates that of  $G^*$ . **(B)** Dataset with three Gaussian clusters of non-uniform density. The Gabriel graph approximation ( $G^{(0)}$ ) naively connects all clusters using multiple edges. After convergence, the clusters become disconnected in  $G^*$ , and its weighted version follows this by assigning negligible weights (due to  $\sigma^*$  between points from different clusters).



---

**Algorithm 1** Iterated Adaptive Neighborhoods kernel

---

```
1: procedure IANKERNEL( $D$ ) ▷ Input: distance matrix,  $D$ 
2:    $G^{(0)} \leftarrow \text{GABRIELGRAPH}(D)$  ▷ Compute initial  $G$  (sec. 3.3)
3:   repeat Iteration
4:      $\sigma^{(t)}, \leftarrow \text{OPTIMIZESCALES}(G^{(t)}, D)$  ▷ Update scales  $\sigma$  based on  $G$  (sec. 3.4)
5:      $\mathcal{G}^{(t)} \leftarrow \text{MULTISCALEKERNEL}(D, \sigma^{(t)})$  ▷ Compute weighted graph (eq. 13)
6:      $\delta, C \leftarrow \text{COMPUTE VOLUMERATIOS}(G^{(t)}, \sigma^{(t)})$  ▷ Relaxation statistic,  $\delta$  (sec. 3.5.1)
7:      $G^{(t+1)} \leftarrow \text{SPARSIFY}(G^{(t)}, \delta)$  ▷ Update  $G$  (sec. 3.5.2)
8:   until no further change in  $G$ 
9:   return  $G^*, \mathcal{G}^*, \sigma^*$  ▷ Output: final discrete and weighted graphs and optimal scales
10: end procedure
```

---

### 3.3 Nearest neighbors in a Gabriel graph

We begin by defining a set of putative neighboring points of  $x_i$  (denoted as  $\mathcal{N}(i)$ ), which uses the connectivity rule found in a *Gabriel graph* [49, 77]. It incorporates directly the observation that closest neighbors should have no points ‘between’ them.

**Definition:** two points  $i$  and  $j$  are *Gabriel-nearest neighbors* to each other if and only if they both touch the same closed ball  $\mathcal{B}_{ij}$  that is empty except for  $i$  and  $j$ .

Note that  $\mathcal{B}_{ij}$  is a *medial ball*, i.e. a ball whose center point is a medial axis, so it has at least two closest points. Thus, this connectivity criterion can be restated as creating an edge for all those medial balls (and only those) touching exclusively two points (to be clear, if a third point touches  $\mathcal{B}_{ij}$  no edge shall be formed).

Hence, to each edge  $e_{ij}$  is associated a medial ball  $\mathcal{B}_{ij}$  centered and the mid-point between  $x_i$  and  $x_j$  with radius  $\|x_i - x_j\|/2$  (Fig. 7). This is furthermore equivalent to the following alternative definitions:

**Remark 1:**  $x_i$  and  $x_j$  are Gabriel-nearest neighbors if and only if any point along the line segment  $\ell_{ij} = \overline{x_i x_j}$  in  $\mathbb{R}^n$  has either  $x_i$  or  $x_j$  as closest point (or both) and no other point.

**Remark 2:** In terms of the Voronoi diagram[45] of  $\mathcal{X}$  (with the cell around  $x_i$  denoted by  $V_i$ ),  $x_i$  and  $x_j$  are neighbors when  $\ell_{ij}$  crosses a single Voronoi hyperplane  $H_{ij}$ , namely that between the cells  $V_i$  and  $V_j$ , and the mid-point between  $x_i$  and  $x_j$  is in  $H_{ij}$ .

As a concrete example, consider two points  $i$  and  $j$  at a distance  $r_{ij}$  from each other, with midpoint  $c$ . Assume the region in the manifold between them is uniformly sampled. Now consider the ball centered at  $c$  with radius  $r_{ij}/2$ , therefore touching  $i$  and  $j$ . If it contains no points in its interior, we say  $i$  and  $j$  are nearest neighbors. Conversely, if there are other points in its interior, under our assumption of uniform density this means there is at least one other point  $k$  ‘‘between’’  $i$  and  $j$ . So we say  $i$  and  $j$  are not nearest neighbors, in the sense that connecting  $i$  and  $j$  directly would be ‘‘crossing over’’ the point  $k$ ; this implies that a direct edge  $e_{ij}$  in the resulting graph would be a poor approximation to a geodesic over  $\mathcal{M}$  (i.e., if  $\mathcal{M}$  is ‘locally uniformly sampled,’ moving

directly from  $i$  to  $j$  would be passing outside of  $\mathcal{M}$ ). Fig. 7 illustrates this procedure. Note that, even when the input to the algorithm is solely a distance matrix (i.e., with no position information), this connectivity criterion may still be evaluated by considering the triangle  $x_i-x_j-x_k$  and using Apollonius’s theorem to compute the length of the median from  $x_k$  to  $c$  (Fig. 7-A).

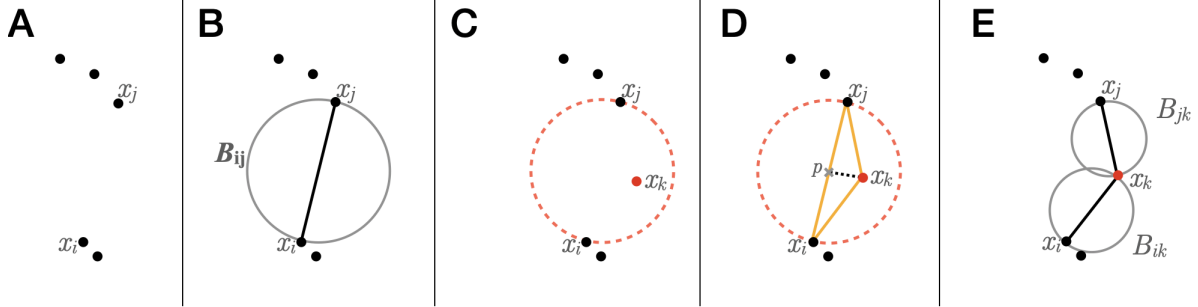


Figure 7: Connecting ‘nearest neighbors’. (A) A set of data points in space. (B) An edge can be formed between  $x_i$  and  $x_j$  because there is no other point in the interior of the ball  $\mathcal{B}_{ij}$  centered halfway between  $x_i$  and  $x_j$ . (C) In this case, because of the presence of a third point,  $x_k$ , inside  $\mathcal{B}_{ij}$ ,  $x_i$  and  $x_j$  cannot be neighbors. (D) Even in the absence of the original data point coordinates, i.e., given only the distances between all pairs of points, Apollonius’s formula can be used to determine the length of the segment  $p-x_k$ , where  $p$  is the center of  $\mathcal{B}_{ij}$ . Namely,  $p-x_k$  is a median of the triangle depicted in orange. Here, because the length of the median is less than the radius of  $\mathcal{B}_{ij}$ ,  $x_i$  and  $x_j$  cannot be neighbors. (E) Edges are drawn connecting points  $x_i$  to  $x_k$  and  $x_k$  to  $x_j$  because both  $\mathcal{B}_{ik}$  and  $\mathcal{B}_{kj}$  are empty except for those pairs of points.

The Gabriel graph is a subgraph of the Delaunay graph [38] and enjoy a number of key properties [77]. We emphasize: (1) they are scale invariant, i.e., there is no pre-specified threshold on the diameter of medial balls to form connections; (2) the guarantee that Gabriel graphs connect points to their true nearest neighbors when  $\mathcal{M}$  is uniformly sampled as grid (as in Fig. 9); and (3), Gabriel graphs provide a locally-adapted neighborhood size  $k_i$  for each point  $x_i$  based on the local geometry. They do not require an initial guess of the number of neighbors, of the intrinsic dimensionality, or of a maximum neighborhood radius.

But the neighborhoods given by the Gabriel graph as not sufficient. We now expand several properties that illustrate their limitations (these will be useful in motivating the rest of the algorithm).

### 3.3.1 Closing triangles

Here we show that the edges created using the above connectivity rule can only form acute triangles in  $\mathbb{R}^n$ . Let three points  $i, j, k$  be such that  $i$  and  $k$  are connected, as well as  $j$  and  $k$ . The rule says  $i$  and  $j$  will only be connected if  $k$  is outside the closed ball  $\mathcal{B}_{ij}$  of radius  $R = r_{ij}/2$  between  $i$  and  $j$  (where  $r_{ij}$  stands for the Euclidean distance between  $i$  and  $j$ ). Apollonius’s formula for the squared distance  $m^2$  between  $k$  and the mid-point between  $i$  and  $j$  is:

$$m^2 = \frac{1}{4}(2r_{ik}^2 + 2r_{jk}^2 - r_{ij}^2). \quad (14)$$

Then,  $k$  is inside  $\mathcal{B}_{ij}$  if and only if  $m^2 < R^2$ , so

$$\frac{1}{4}(2r_{ik}^2 + 2r_{jk}^2 - r_{ij}^2) \leq R^2 = \left(\frac{r_{ij}}{2}\right)^2 \quad (15)$$

$$r_{ik}^2 + r_{jk}^2 \leq r_{ij}^2.$$

Notice that equality will hold when  $i - j - k$  is a right triangle. Therefore,

**Remark 3:** A triangle will be closed by edges only when the triangle  $i - j - k$  is acute (Fig. 8-A).

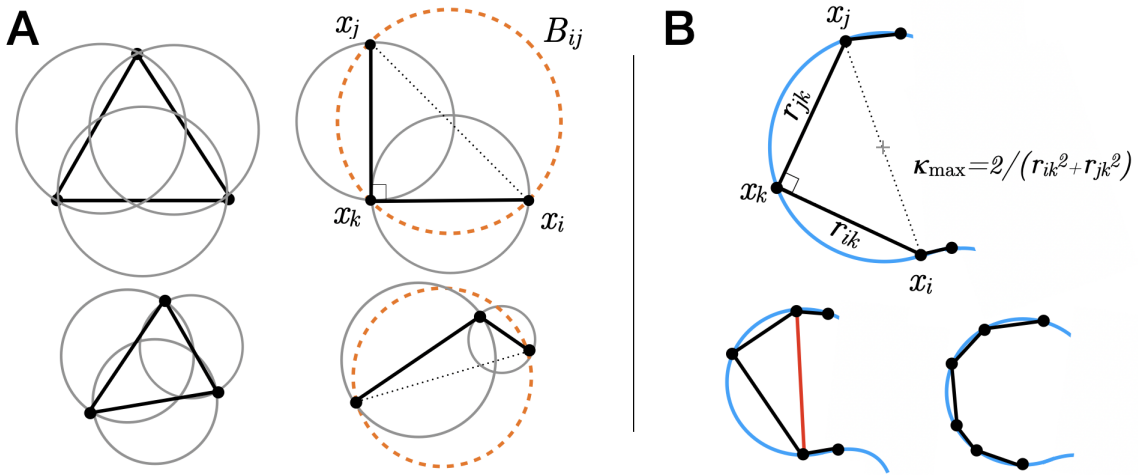


Figure 8: Implications of the connectivity rule in a Gabriel graph on closing triangles from edges and on the maximum curvature of a geodesic on  $\mathcal{M}$  that can be inferred from the resulting connectivity. **(A)** Left: three points will be mutual neighbors if and only if they form an acute triangle (left). If the angle between  $i$  and  $j$  at  $k$  is at least  $\pi/2$ , all three points will touch the ball  $\mathcal{B}_{ij}$ , so no edge is created (right). **(B)** Geodesics over a manifold (in blue). The maximum principal curvature in  $\mathcal{M}$  that can be reasonably approximated by the resulting graph geodesic is a function of the sampling interval. The limiting case occurs when three points form a right triangle (top) (see eq. 16). Closing a triangle (bottom left) prevents the graph from adequately capturing the manifold's geometry. As sampling frequency increases (bottom right), higher curvatures can be better approximated by the Gabriel graph. (Distances denoted by  $r_{..}$  are taken in ambient space.)

### 3.3.2 Maximum curvature

The above result leads to a bound on the maximum principal curvature that is allowed locally on  $\mathcal{M}$  such that  $G$  correctly approximates it (i.e., without closing a triangle). Assume  $i$ ,  $j$ , and  $k$  are points on a smooth manifold  $\mathcal{M}$  as in Fig. 8-B, up to the level that the sampling defines; then, if we assume constant curvature  $\kappa$  locally, the geodesic from  $i$  to  $j$  passing through  $k$  is an arc of a circle  $\mathcal{C}$ . Therefore, the segments  $\ell_{ik}$  and  $\ell_{kj}$  approximate geodesics on  $\mathcal{M}$ , but not  $\ell_{ij}$  (which in fact would even increase the local intrinsic dimensionality). Hence, values of curvature that can

be correctly inferred are those that do not create an edge between  $i$  and  $j$  in the Gabriel graph (i.e., those for which the ball  $\mathcal{B}_{ij}$  is non-empty), as shown in Fig. 8-B. In this case, from Eq. 15, the maximum such curvature,  $\kappa^{\max}$ , occurs when  $i$ ,  $k$ , and  $j$  form a right triangle in space (as any larger value would cause this triangle to be acute and  $i$  would be connected to  $j$ ). Then, from Thales’s theorem, the diameter  $D$  of  $\mathcal{C}$  would equal that of the hypotenuse  $\ell_{ij}$ , so

$$\kappa^{\max} = \frac{1}{D/2} = \frac{2}{D} = \frac{2}{\sqrt{r_{ik}^2 + r_{jk}^2}}. \quad (16)$$

An interesting case to consider is that when  $\mathcal{M}$  is uniformly sampled with constant interval  $T$  over arc length. Then, the arc length  $s$  between  $i$  and  $j$  is  $2T$ ; but, since  $r_{ij} = D$ ,  $s$  covers half the circle and we have  $2T = \pi D/2$ . Eq. 16 then becomes

**Remark 4:**

$$\kappa^{\max}(T) = \frac{\pi}{2T}. \quad (17)$$

These define the maximum geodesic curvature in  $\mathcal{M}$  that can be correctly inferred from a Gabriel graph. As a consequence, the reach is lower bounded by  $1/\kappa^{\max}$ .

### 3.3.3 Degree distribution in Gabriel graphs

We now study the above connectivity rule starting with flat, uniformly sampled manifolds (“grids”) to illustrate how Gabriel graphs naturally adapt to both the geometry and dimensionality of the grid. As shown in Fig. 9, in such ideal cases the degree of an interior node in the Gabriel graph agrees with the true number of (literal) nearest neighbors, i.e.: 2 for collinear points, 4 for a square grid, and 6 for a triangular grid (Fig. 9-A).

The degree corresponds to the dimension (degree  $\sim 2^d$ ) except for the (curious) triangular grid. Adding noise (Gaussian noise with standard deviation equal to half the spacing between neighboring points) supports this conjecture, as the degree then approaches 4 regardless of the original grid structure. This holds in higher dimensions as well (Fig. 9(B,C) for both normal and uniform sampling at random (Fig. 11).

**Remark 5:** The expected number of neighbors in a Gabriel graph approximately follows a distribution centered at  $2^d$  (where  $d$  is the intrinsic dimensionality of the dataset) for a variety of sampling strategies. (Fig. 9-C).

Because Gabriel graphs are inherently scale invariant, this degree distribution is largely independent of sampling density.

How to explain such remarkable regularity despite the randomness of sampling? There is a geometric view of the Gabriel graphs: each edge between data points implies an “occluding hyperplane” that blocks other points from becoming neighbors (Fig. 7). For example, when  $d = 1$ , two points necessarily occlude any additional connections, and every non-boundary point must have 2 neighbors. Now, using the diagrams in Figs. 9-D–F as reference, we find that, when  $d = 2$ , on average  $\sim 4$  points are sufficient to occlude a point  $x_i$  from all sides. For  $d = 3$ , this number is doubled again and the expected number of neighbors becomes  $\sim 8$ , revealing the trend.

Every additional dimension adds a new coordinate axis along which the previous constraints are duplicated, roughly doubling the average number of directions available for neighbors to connect from. Once  $2^d$  balls are “attached” to  $x_i$ , the space available becomes too small, and so does the probability of drawing a sample point from inside the region  $\mathcal{H}$  enclosed by the hyperplanes.

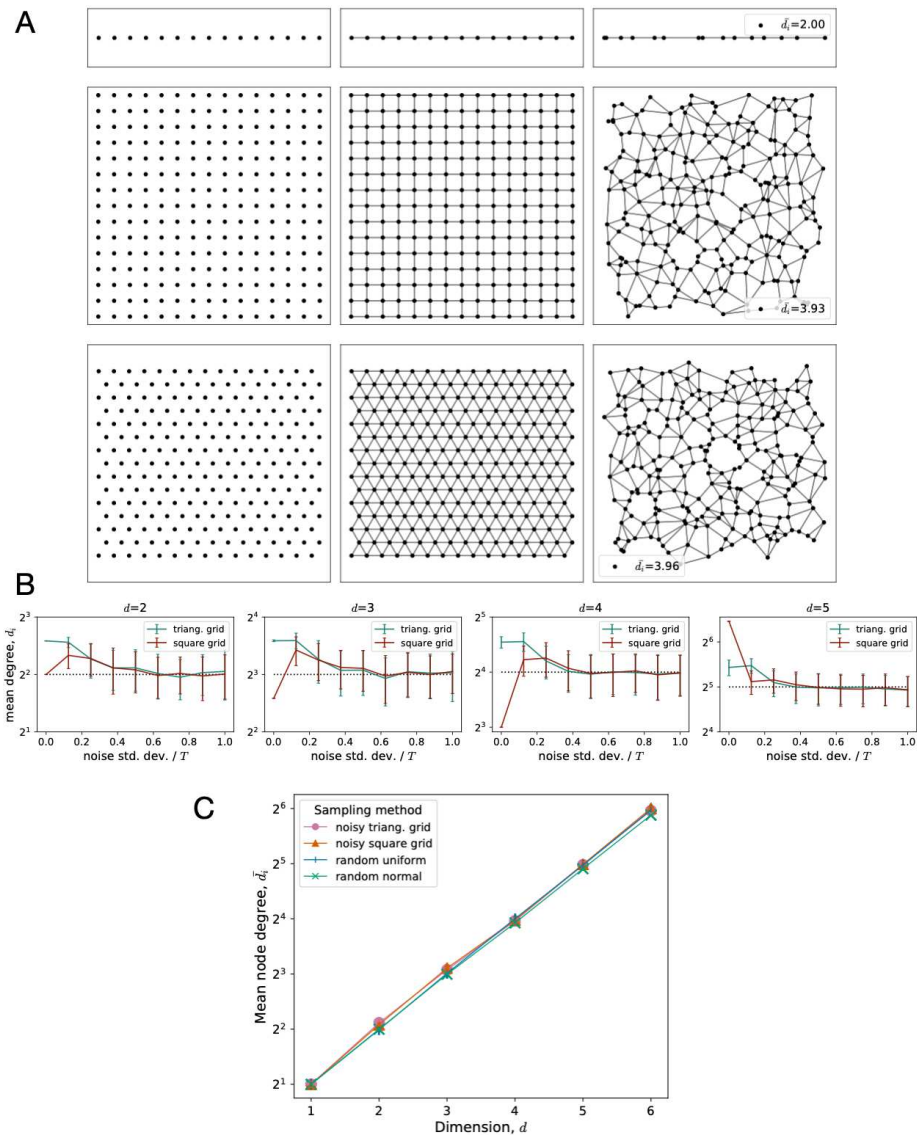


Figure 9: Gabriel graphs computed on different uniformly sampled datasets (regular grids) with various amounts of Gaussian noise and the resulting distributions of node degree,  $d_i$  (number of neighbors) for non-boundary points. **(A) Top:** A sequence of collinear points (left) produces a one-dimensional grid (center). Addition of noise (right) does not change the mean degree  $\bar{d}_i$  (a constant 2 for interior points). **Middle:** A square grid (left) result in a quadrilateral mesh with with constant degree 4 in its interior. Although the addition of noise considerably scrambles the points, the mean degree is approximately unchanged. **Bottom:** Points arranged as a triangular grid (left) result in a triangular mesh where every interior node has degree 6. Its noisy version looks similar to a noisy square grid, with its mean degree decreasing to about 4 as well. (Cont. next page.)

Figure 9: (Cont. from previous page.) (B) Change in degree distribution for interior points of  $d$ -dimensional triangular and square grids upon addition of Gaussian noise with increasing standard deviation (as a scalar multiple of the original sampling interval,  $T$ ). Moderate amounts of noise are sufficient to make the mean degrees be approximately  $2^d$ . Error bars indicate standard deviation; dotted lines show constant  $2^n$  values for reference. Noise applied to grids in (A) has  $0.5T$  std. dev. (C) Mean node degree of  $n$ -dimensional manifolds sampled using different strategies: uniformly at random, normally at random, and as jittered versions of regular triangular and square grids (added Gaussian noise with std. dev.  $0.5T$ ). Remarkably, mean degree grows approximately as  $2^n$  regardless of the sampling strategy.

When the neighbors are regularly spread around  $x_i$ , by construction this region  $\mathcal{H}$  is equivalent to a  $d$ -dimensional orthoplex<sup>2</sup> (or cross-polytope). A  $d$ -orthoplex has  $2^d$  facets (or  $(d - 1)$ -faces), and it is one of the three regular, convex polytopes that exist in dimension higher than 4 (hypercubes and simplices). Naturally, when sampling is not uniform, we should find irregular orthoplexes instead. While this geometric construction supports our empirical results, and implies they should hold in higher dimensions, it also suggests:

---

<sup>2</sup>An orthoplex is a line segment in 1-D, a square in 2-D, a regular octahedron in 3-D, and a 16-cell in 4-D.

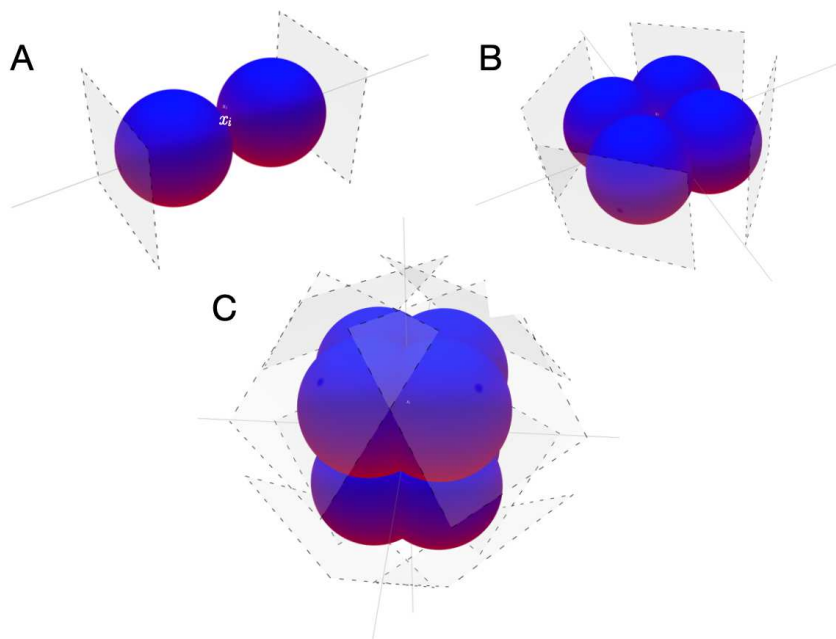


Figure 10: A central point  $x_i$  and the occlusion planes due to neighbors (Fig. 7) in dimensions 1, 2, and 3 (panels A–C, respectively). Every additional dimension adds a new coordinate axis along which the previous constraints are duplicated, roughly doubling the average amount of directions available for neighbors to connect from. Once  $2^d$  balls are “attached” to  $x_i$ , the remaining space is greatly reduced, and so is the probability of drawing a sample point from inside the region enclosed by the hyperplanes.

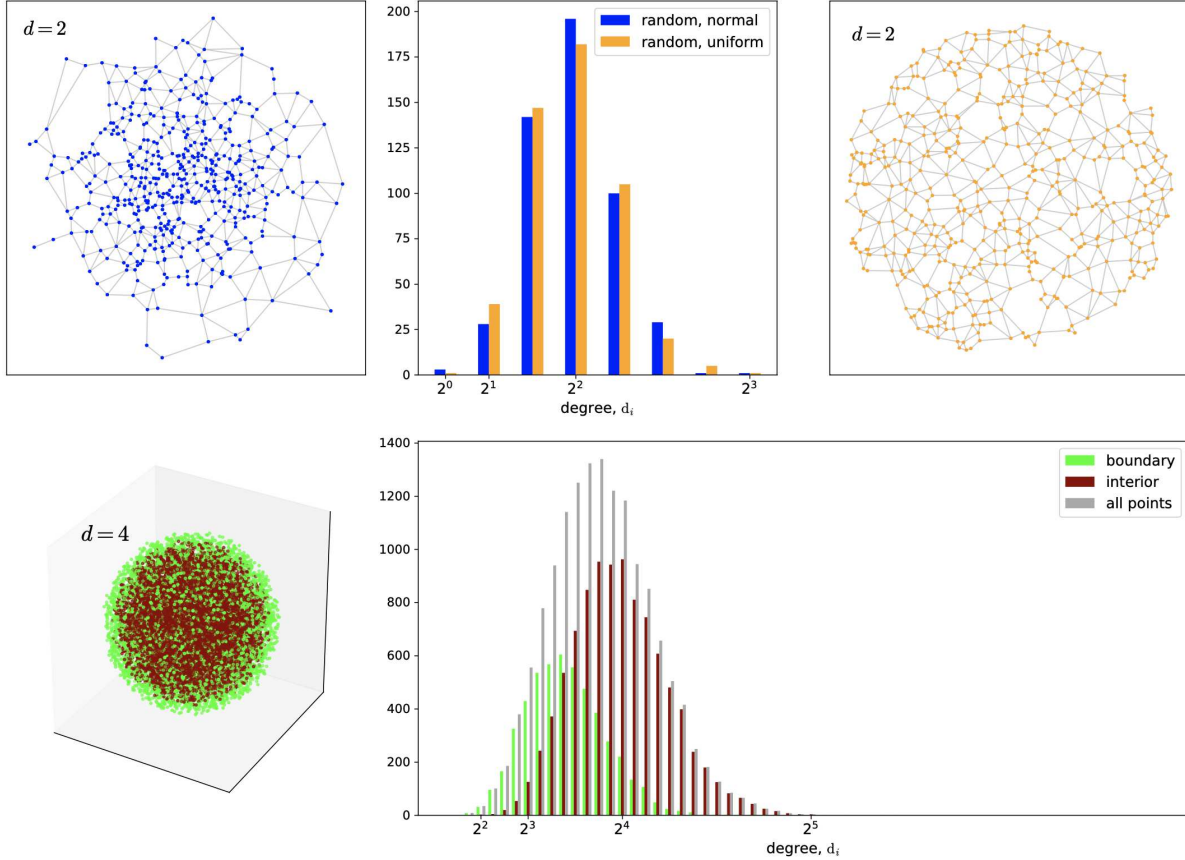


Figure 11: Distribution of node degree  $\deg(i)$  in the Gabriel graph of datasets with different sampling strategies and dimensionalities. *Top:* Points sampled normally (orange) or uniformly (blue) at random from a two-dimensional ball result in similar degree distributions centered at  $2^2$ . *Bottom:* In higher dimensions, interior points continue to follow this pattern. On the left, a 4-dimensional unit ball sampled uniformly at random is shown projected onto first 3 coordinates, with boundary points labeled as those with vector norm  $> 0.9$  (edges omitted for clarity). It produces a Gabriel graph where interior points have degree distribution centered at  $\sim 2^4$ , and the mean degree of boundary points is closer to  $2^3$ .

**Remark 6:** The organization of randomly scattered neighbors around a point is more similar to facets of an orthoplex than to those of a hypercube or of a simplex (these latter two correspond to square grids and triangular grids, respectively, and are too sparse and non-generic to correctly describe random points).

The Gabriel graph enjoys many attractive properties, and provides the starting point for our algorithm. The above arguments show how the space is largely filled by Gabriel balls within the manifold, but Gabriel balls may also fill space across holes and reaches. Curvature must be dealt with. This was illustrated in Fig. 6, where we showed that Gabriel connections can arise incorrectly and must be removed. To do so one must ‘look’ in every direction (of the tangent plane), and one must look past immediate neighbors. For this we now develop the weighted graph counterpart to the Gabriel graph, exploiting the kernel to extend local information globally. This begins to connect the graph construction more directly to manifold properties.

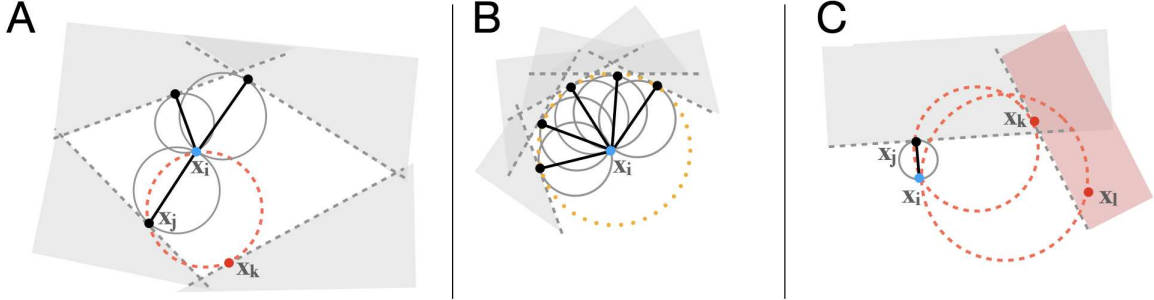


Figure 12: (A) A central point  $x_i$  (in blue) and its neighbors (in black). Every neighbor  $x_j$  that  $x_i$  has “occludes” the entire area behind a hyperplane tangent to  $\mathcal{B}_{ij}$  at  $x_j$  (dashed lines). That is, no point inside the occluded areas (shaded region) can form a connection with  $x_i$ . Here, the dashed ball  $\mathcal{B}_{ik}$  does not form a connection because  $x_j$  lies exactly on its boundary; despite this,  $x_k$  still contributes with an occluding hyperplane, preventing farther points from forming a connection with  $x_i$ . (B) In principle there is no limit to the number of neighbors a point in ambient space  $\mathbb{R}^n$  may have (when  $n \geq 2$ ), since any point on the hypersphere of radius  $r_{ij}$  around  $x_i$  (dotted curve in orange) will not be occluded. Sets of nodes with connectivity such as this are termed “wheels” in graph theory, and the more points they contain the more unlikely to occur they become in real datasets. In this example, any appreciable variability in the distances from  $x_i$  to its neighbors would occlude one (or several) of the others. (C) Even points inside occluded areas can contribute with additional occluding hyperplanes. Here, although  $x_k$  lies inside the region occluded by  $x_j$  (and therefore cannot form a connection with  $x_i$ ), it produces further occlusion behind a hyperplane of its own (region shaded in red). So  $x_l$  cannot connect to  $x_i$  either, due to the presence of  $x_k$  (even though it is not occluded by  $x_j$ ).

### 3.4 Multi-scale optimization

We now begin to develop the iteration in Algorithm 1, given the initial Gabriel neighborhood graph  $G^{(0)}$ . Assuming (temporarily) that this gives correct local neighborhoods, what should the corresponding scales be for a Gaussian kernel? In effect this is an extension of  $G$  into a weighted counterpart,  $\mathcal{G}$ . From Fig. 5, this weighted graph is also a type of approximation of (aspects of) the continuous manifold. Because density is not necessarily uniform, different points might have different neighborhood radii, so a multi-scale Gaussian similarity kernel (eq. 13) is used. Each point  $x_i$  has its own associated scale,  $\sigma_i$ . To develop this scale, we now move into the continuous domain and exploit the geometric notion of a cover.

#### 3.4.1 Covering criterion

A criterion for separability between two Gaussians has been developed in the mixture-of-Gaussians literature. [34, 7, 103]: two spherical Gaussians  $i$  and  $j$  can be distinguished (in the sense of solving a classification problem) with reasonable probability when they have a separation of at least

$$\|\boldsymbol{\mu}_i - \boldsymbol{\mu}_j\| > C \max\{\sigma_i, \sigma_j\}, \quad (18)$$

at which the overlap in their probability mass is a constant fraction [103]. We flip this around, by using Gaussians centered at midpoints to indicate when neighboring points should be connected,



not separated (Fig. 5 illustrates this construction directly). Furthermore, because we use a multi-scale kernel, the (non-normalized) density is a function of  $\sqrt{\sigma_i\sigma_j}$ . Hence we obtain a criterion for what we term *C-connectivity*:

**Definition:** Two neighbors  $i$  and  $j$  in the discrete graph  $G = (E, V)$  are  $C$ -connected by the multi-scale kernel when the geometric mean of their individual scales is at least the distance between  $\mathbf{x}_i$  and  $\mathbf{x}_j$  scaled by a positive constant  $C$ :

$$C\|\mathbf{x}_i - \mathbf{x}_j\| \leq \sqrt{\sigma_i\sigma_j}. \quad (19)$$

The constant,  $C$ , plays a role in normalizing for unknown density. It will be developed in Sec. 3.5.2. For now, we illustrate its role in the connection from graphs to manifolds. Fig. 13 shows the graph over a set of data points, and the local scales obtained (by the algorithm below) for different values of  $C$ . Choosing  $C$  too large yields scales (and hence Gaussians) that are too large; that is, their overlap has peaks. Choosing it too small yields scales that introduce holes. Choosing it correctly (in this case,  $C = 0.9$ ) shows how the Gaussians form a covering of the manifold that approximates a partition of unity. Such partitions of unity are used in differential geometry to extend local information (in our case, the scales) to global information (a covering of the manifold).

By choosing appropriate scales, i.e. scales that meet our criterion for all edges in  $E$ , we also ensure a covering of the edges, in the following sense. The value of the multi-scale kernel  $K_{ij}$  between  $\mathbf{x}_i$  and  $\mathbf{x}_j$  is identical to that of a kernel re-centered at the midpoint  $\mathbf{p} \equiv (\mathbf{x}_i + \mathbf{x}_j)/2$  and re-scaled using half the geometric mean of  $\sigma_i$  and  $\sigma_j$  as its scale  $\sigma_{\mathbf{p}}$ :

$$K_{ij} = \exp \frac{-\|\mathbf{x}_i - \mathbf{x}_j\|^2}{\sigma_i\sigma_j} = \exp \frac{-\|(\mathbf{x}_i - \mathbf{x}_j)/2\|^2}{\sigma_i\sigma_j/2^2} = \exp \frac{-\|(\mathbf{p} - \mathbf{x}_i)\|^2}{\sigma_{\mathbf{p}}^2} \quad (20)$$

with  $\sigma_{\mathbf{p}} \equiv \sqrt{\sigma_i\sigma_j}/2$ .

**Remark 7:** We say a  $C$ -covering is attained when every pair  $(i, j) \in E$  is  $C$ -connected (eq. 19). Additionally, when the spacing between neighboring points is approximately uniform locally, the pointwise summation over all Gaussian kernel bumps given by the individual scales provides an (un-normalized) partition of unity of  $\mathcal{M}$ .

We now use the covering constraints to solve for the set of scales  $\sigma$ . It is desirable to have the scales be small (respecting the reach), while at the same time maintaining the connectivity in  $\mathcal{G}$  close to that of  $G$ . Thus, one idea is to find scales such that the sum of edge weights in  $\mathcal{G}$  incident to a node  $i$  from its neighbors in  $G$  is approximately equal to the degree of  $i$  in  $G$ , for all  $i$ , while at the same time ensuring a  $C$ -covering. This, however, amounts to a non-convex problem in which the cost function involves a summation of multi-scale kernel values. We are unable to solve this efficiently. Instead, we find the smallest individual scales such that our covering criterion is satisfied for all edges (a ‘minimal covering’), and later address the quality of the relaxation by using a statistical pruning (edge sparsification). This can be transformed into a convex, linear program with linear constraints by which all scales can be solved for simultaneously, as we now show.

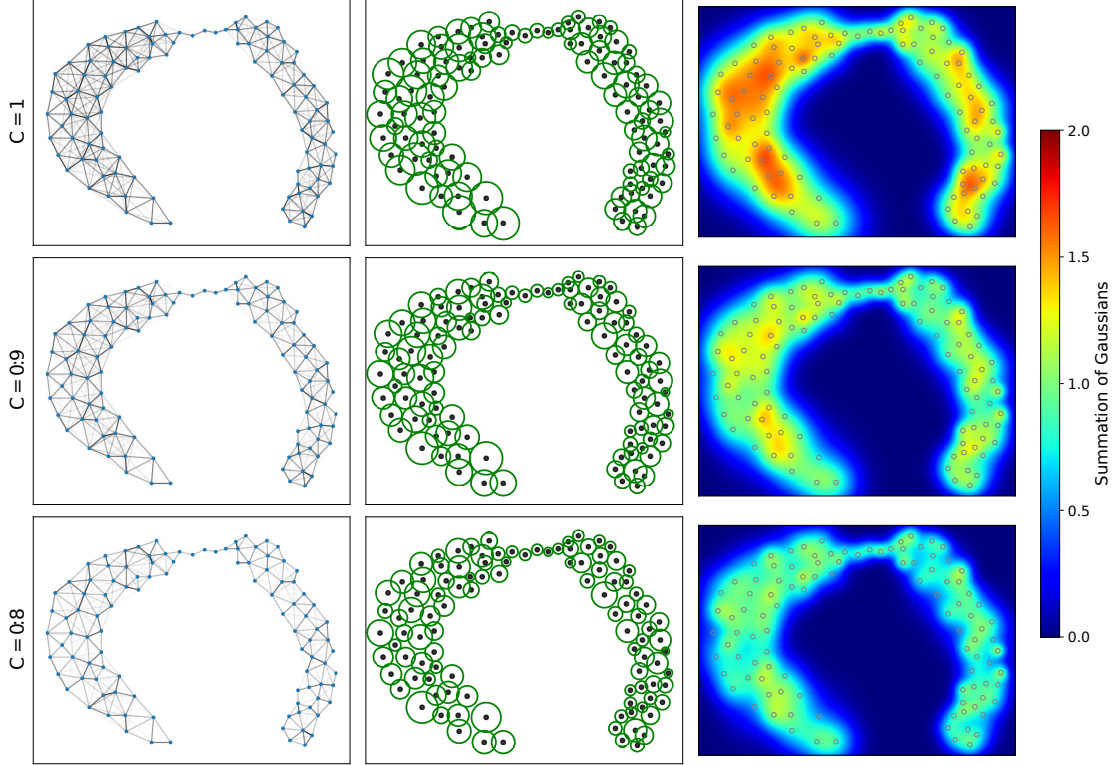


Figure 13: Effect of hyperparameter  $C$  from eq. 19 on the resulting weighted graph (left), optimal scales (middle), and manifold approximation (right, shown as the resulting summation over the Gaussian kernels around each point using their individual scales). For  $C = 1$  (top), the scales overlap too much and as a result the Gaussian summation (right) is highly non-uniform. For  $C = 0.8$  (bottom), the scales are not sufficiently large to properly cover the underlying manifold, resulting in holes (right). When  $C = 0.9$ , there is a good compromise between covering and keeping a uniform density, so the Gaussian summation approximates a partition of unity (summing to  $\sim 1$  everywhere) when the scales correctly conform to the local sampling characteristics. Our approach will allow us to tune  $C$  based on a relaxation statistic,  $\delta$ .

### 3.4.2 Linear program relaxation

To achieve a minimal covering one might minimize  $\sum_i \sigma_i$  (or, equivalently, the 1-norm of the vector  $\sigma$ , since scales are positive) subject to the covering constraint<sup>3</sup>. This suggests the following:

**Optimization Problem:**

$$\begin{aligned}
 \min_{\sigma} \quad & \mathbf{1}^\top \sigma \\
 \text{s.t.} \quad & (i, j) \text{ is } C\text{-connected } \forall (i, j) \in E \\
 & \sigma_i \text{ is bounded, } \forall i \in V
 \end{aligned} \tag{21}$$

<sup>3</sup>Another possibility is to use a weighted sum  $\sum_i \nu_i \sigma_i$  while keeping the same constraints, thus still guaranteeing a covering. The weights  $\nu_i$  add a bias to how the length of an edge is split between its two incident nodes (by balancing their individual scales). One interesting option is to set  $\nu_i = r_i^{\text{non}} / r_i^{\text{FN}}$ , i.e. the ratio between the distance to the nearest non-neighboring point,  $r_i^{\text{non}}$ , and the farthest neighbor,  $r_i^{\text{FN}}$ .

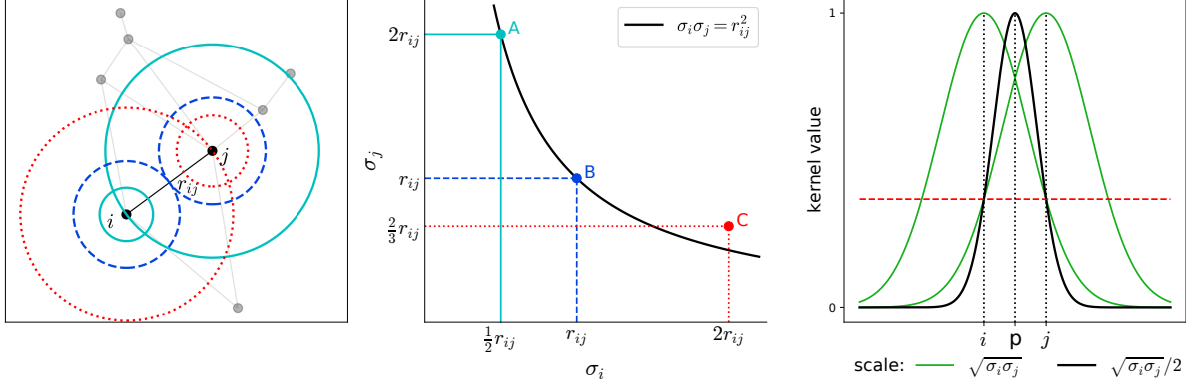


Figure 14: Covering constraint for the multi-scale kernel of eq. 13. *Left:* A graph  $G$  with two nodes  $i$  and  $j$  at a distance  $r_{ij}$  from each other in  $\mathbb{R}^n$ . Since they are connected, their assigned individual scales  $\sigma_i$  and  $\sigma_j$  must satisfy  $\sigma_i \sigma_j \geq r_{ij}^2$  to satisfy the covering constraint (here we assume  $C=1$ ). *Center:* All feasible pairs  $(\sigma_i, \sigma_j)$  lie inside the region above a positive hyperbola, three of which are indicated as colored points; the pairs A and B satisfy exactly, while C satisfies in excess. Each one is also depicted as a pair of circles on the left plot using the same color code, each one centered at its corresponding node (radii are set to half the scale, for clarity). Although pairs A and B differ in their ratio  $\sigma_i/\sigma_j$ , both result in the same multi-scale kernel value for the edge  $(i, j)$  since the product  $\sigma_i \sigma_j$  is the same (pair C will yield a slightly higher value). This illustrates the freedom that might exist in choosing an optimal combination of scales for all nodes (i.e., a covering). *Right:* multi-scale kernel ( $K_{ij}$ ) values centered at either  $i$  or  $j$  (shown in green) are symmetric (with scale  $\sqrt{\sigma_i \sigma_j}$ ). Horizontal axis represents position over the line in  $\mathbb{R}^n$  passing through  $i$  and  $j$ . A kernel centered at the midpoint  $\mathbf{p}$  between  $i$  and  $j$  using half the scale (black curve) attains the same values as  $K_{ij}$ . Dashed red line indicates the common value between all three kernels.

where  $\boldsymbol{\sigma}$  is the vector of individual scales  $\sigma_i$  and  $\mathbf{1}$  the all-ones vector. Now it remains to represent the  $C$ -covering requirement with a set of constraints.

Looking in detail at  $C$ -connectedness (eq. 19) as a function of  $\sigma_i$  and  $\sigma_j$ , observe that it represents a region delimited by a single-branched hyperbola (since the distance and scales are positive):

$$\sigma_i \sigma_j \geq (C r_{ij})^2, \quad \sigma_i > 0, \sigma_j > 0, \quad (22)$$

where  $r_{ij} \equiv \|\mathbf{x}_i - \mathbf{x}_j\|$ ). Each  $\sigma_i$  is naturally bounded above by the distance to  $i$ 's farthest neighbor,  $r_i^{\text{FN}}$ :

$$\sigma_i \leq r_i^{\text{FN}}, \quad (23)$$

beyond which all neighbors are satisfied<sup>4</sup>, so further increasing either scale would make the weights to non-neighbors larger than strictly necessary (thereby hurting the kernel graph relaxation). These bounds, combined, specify a bounding box for each edge that must necessarily be crossed (or at least touched) by the hyperbola since  $r_{ij} > 0$ .

Due to the hyperbolae, this amounts to a non-linear, non-convex set of constraints. However, we can convexify the feasible set by considering, for each edge  $(i, j)$ , the line(s) passing through

<sup>4</sup>That is assuming  $C \leq 1$  (a natural choice, as explained above). If for some reason one needs  $C > 1$ , then the upper bounds must be scaled by  $C$  in order to ensure feasibility.

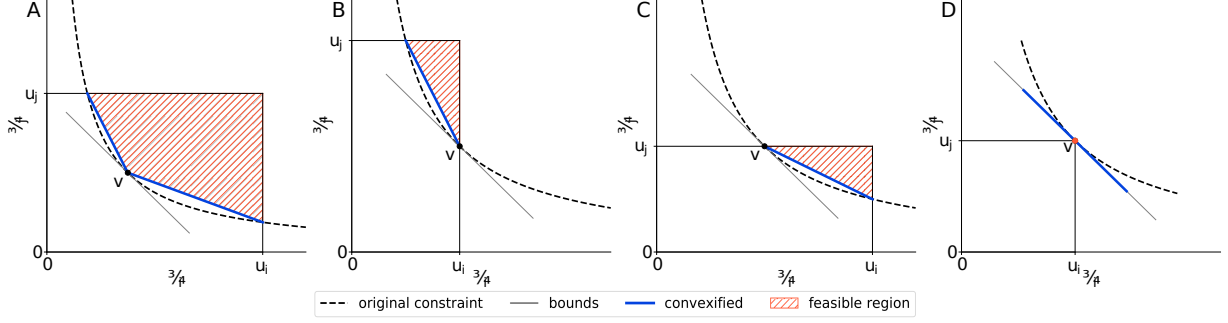


Figure 15: Examples of constraints introduced by an edge  $e_{ij}$  in  $G$ . The  $C$ -connectivity rule, i.e., the hyperbola given by  $\sigma_i \sigma_j = (C \|\mathbf{x}_i - \mathbf{x}_j\|)^2$  (dashed curve), when convexified may give rise to 1 or 2 linear constraints depending on whether the hyperbola’s vertex  $v$  (point where  $\sigma_i = \sigma_j$ ) intersects the bounding box given by the lines  $\sigma_i = 0, \sigma_j = 0, \sigma_i = u_i$ , and  $\sigma_j = u_j$ . Hatched area (in orange) shows feasible region using convexified constraints; tangent line at  $v$  is shown in gray. When  $v$  is interior to the bounding box (A), two secants (in blue) define the feasible region (namely the lines passing through  $v$  and the points where the hyperbola intersects the lines  $\sigma_i = u_i$  and  $\sigma_j = u_j$ ); when either  $v = u_i$  (B) or  $v = u_j$  (C), only one secant is necessary; when  $v$  coincides with both  $u_i$  and  $u_j$  (D), i.e.,  $(C \|\mathbf{x}_i - \mathbf{x}_j\|)^2 = u_i u_j$  (which may occur if  $C$  is set to 1), again only one inequality is necessary, namely tangent line at  $v$ .

the hyperbola’s vertex (the point at which  $\sigma_i = \sigma_j = Cr_{ij}$ ) and the points where the hyperbola intersects the bounding box (the four possibilities are shown in Fig. 15). The feasible region for each edge, therefore, is bounded by a convex envelope given by such line(s) and those defined by the upper bounds to  $\sigma_i$  and  $\sigma_j$ . Such envelopes for all edges, combined, define the boundaries of a convex polytope. Note that this convexification is conservative in the sense that only the objective is relaxed—the feasible scales are always at least as large as required by the original non-convex problem, therefore our covering requirement is not relaxed. (Because of the presence of a later pruning stage in the algorithm, it is better to over-connect here than to inadvertently disconnect nodes that should otherwise be connected.)

Letting  $m \leq 2|E|$  be the total number of linear constraints obtained as above and  $N$  the number of nodes in  $G$ , we define the  $m \times N$  matrix  $\Lambda$  and the  $m \times 1$  vector  $\mathbf{b}$ . Now, for each edge  $e_{ij}$ , let its two possible constraints be expressed as

$$\sigma_j \geq \alpha_{ij}^{(1)} \sigma_i + \beta_{ij}^{(1)} \quad (24)$$

$$\sigma_j \geq \alpha_{ij}^{(2)} \sigma_i + \beta_{ij}^{(2)} \quad (25)$$

with  $\alpha_{ij}$  and  $\beta_{ij}$  denoting, respectively, the slope and intercept of the corresponding line(s) forming its convex envelope. Rearranging, we obtain  $\alpha_{ij} \sigma_i - \sigma_j \leq -\beta_{ij}$  for each line, which is encoded as a row in  $\Lambda$  with values  $\alpha_{ij}$  and  $-1$  at columns  $i$  and  $j$ , respectively (with zeros everywhere else) and an entry in  $\mathbf{b}$  with value  $-\beta_{ij}$ :

$$\begin{array}{ccccccc}
& & & & \Lambda & & & & & & \mathbf{b} \\
& & \dots & & & \dots & & & & & \\
& & & i & & & j & & & & \\
\vdots & & \vdots & & \vdots & & \vdots & & \vdots & & \\
e_{ij}^{(1)} & \left[ \begin{array}{cccccccc} 0 & \dots & \alpha_{ij}^{(1)} & \dots & 0 & \dots & -1 & \dots & 0 \end{array} \right. & \sigma & \leq & \left[ \begin{array}{c} \vdots \\ -\beta_{ij}^{(1)} \\ -\beta_{ij}^{(2)} \\ \vdots \end{array} \right] \\
e_{ij}^{(2)} & \left[ \begin{array}{cccccccc} 0 & \dots & \alpha_{ij}^{(2)} & \dots & 0 & \dots & -1 & \dots & 0 \end{array} \right. & & & \\
\vdots & \left. \begin{array}{cccccccc} \vdots & & \vdots & & \vdots & & \vdots & & \vdots \end{array} \right] & & & \\
& & & & m \times N & & & & N \times 1 & & m \times 1
\end{array}$$

**Remark 8:** The convex envelope defining the constraints can be expressed by the linear inequalities:

$$\begin{aligned}
\Lambda \sigma &\leq \mathbf{b} \\
\mathbf{0} &< \sigma \leq \mathbf{r}^{\text{FN}}
\end{aligned} \tag{26}$$

where  $\mathbf{r}^{\text{FN}}$  is the vector of distances to each node’s farthest neighbor.

Hence the problem now amounts to a convex, linear program with linear constraints:

**LP Relaxation:**

$$\begin{aligned}
\min_{\sigma} \quad & \mathbf{1}^\top \sigma \\
\text{s.t.} \quad & \Lambda \sigma \leq \mathbf{b} \\
& \mathbf{0} < \sigma \leq \mathbf{r}^{\text{FN}}
\end{aligned} \tag{27}$$

which can be readily solved by a variety of methods (see, e.g., [21]). Figs. 19 , 21 , 20 show the results of running this optimization on different examples.

### 3.5 Sparsification

To recap: the Gabriel graph provides an initial estimate of neighbors; the LP optimization provides minimal scales for a continuous kernel to cover these connections. However, since the initial estimate of the discrete graph might contain incorrect connections, its resulting optimal scales might also be inadequate. An example of this can be seen in Fig. 19: initially, two pairs of nodes are connected across the central gap since a medial ball exists between them. This will cause very large scales to be necessary to “cover” these edges. Furthermore, the Gabriel graph is based on a local connectivity rule. However, as illustrated in Fig. 16, decisions about connecting nodes across a gap should not be local. We here address both of these issues, by introducing a global statistics based on how frequently such a gap occurs in the dataset. In terms of Algorithm 1 1, we are now at steps 6 and 7.

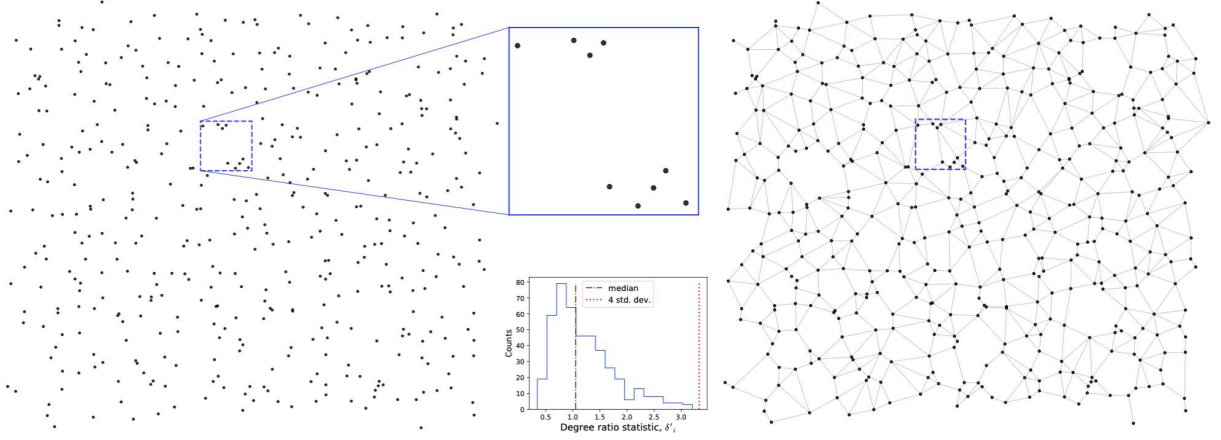


Figure 16: Local vs. global assessment of neighborhoods. *Left:* The points inside the cropped window appear to form two well-defined clusters when looked up close (local estimation). However, when considered in the context of the full dataset (global estimation), the apparent gap between the top and bottom groups “disappears,” i.e., it is well within the range of gaps observed throughout the data. More precisely, it does not significantly deviate from the average sampling interval. *Right:* The converged graph  $G$  indeed connects the two groups by edges, and the distribution of degree ratios,  $\delta'_i$  (lower inset), confirms that all edges are reasonable up to 4 standard deviations from the median.

### 3.5.1 Volume ratio

Because incorrect connections can be given by Gabriel balls lying in the free space between parts of a manifold, i.e. across the reach, it is tempting to simply prune the longest connections. Note, however, that the size of a scale by itself is not necessarily telling: in both examples shown in Fig. 6, the non-uniform density causes scale sizes to vary, and some of the large ones are appropriate. That is, the largest scale is consistent with the distances to its neighbors. Conversely, and importantly, large scales that are excessive will likely cover “too many” points. That is, the scale will suggest neighbors in excess of the number of discrete neighbors to its corresponding node in  $G$ . We quantify this notion by observing that the individual scale  $\sigma_i$  should produce kernel values whose sum is comparable to the discrete degree  $d_i$  of node  $i$  in  $G$ . As we shall show, after proper normalization this also means  $\sigma_i$  relates to a local volume element around  $\mathbf{x}_i$ , or the inverse of the local density. Since each connection in  $G$  can be seen as having unit weight, a Gaussian kernel around  $\mathbf{x}_i$  with scale  $\sigma_i$  should distribute that same amount,  $d_i$ , only continuously over ambient space.

We start our derivation with a definition, for non-isolated nodes  $x_i$ :

**Definition:** let  $w_{ij}^{(\sigma_i)}$  be the Gaussian kernel value between  $\mathbf{x}_i$  and  $\mathbf{x}_j$  using scale  $\sigma_i^t$  at iteration  $t$ . A (non-isolated) node’s *volume ratio* at iteration  $t$ ,  $\delta_i^{(t)}$ , is

$$\delta_i^{(t)} \equiv \frac{\sum_{j \in V} w_{ij}^{(\sigma_i^t)}}{\sum_{j \in V} a_{ij}}, \quad (28)$$

i.e., the ratio between node  $i$ ’s weighted degree due to  $\sigma_i^{(t)}$  and its discrete degree in  $G^{(t)}$ . (Hence-

forth we suppress the iteration dependency ( $t$ ) to simplify notation.) Here an individual-scale Gaussian kernel is needed in order to correctly assess the impact of  $\sigma_i$  on the relaxation from the perspective of  $i$  alone—a multi-scale kernel may artificially increase the weighted degree of  $i$  when other nodes (even non-neighbors of  $i$ ) have incorrect scales. (However, as discussed below, a corresponding ratio using the actual weights in  $\mathcal{G}$  may be used for convergence purposes.)

Now, using a mean-value integral (as in [31]), the numerator approximates the volume under the continuous Gaussian kernel over  $\mathcal{M}$ , and can be further approximated by

$$\sum_j w_{ij}^{(\sigma_i)} = \sum_j w_{ij}^{(\sigma_i)} \approx \frac{N}{\text{vol}(\mathcal{M})} \int_{\mathcal{M}} \exp\left(\frac{-\|\mathbf{x}_i - \mathbf{x}_j\|^2}{\sigma_i^2}\right) d\mathbf{x}_j \quad (29)$$

when  $\mathcal{M}$  has uniform density and low curvature. In practice, the kernel will have compact support due to numerical precision (i.e., its values become effectively zero for sufficiently large distances), so by defining the volume element  $dV_i \equiv \text{vol}(\mathcal{N}(\mathbf{x}_i))/|\mathcal{N}(\mathbf{x}_i)|$  of a continuous neighborhood  $\mathcal{N}(\mathbf{x}_i) \in \mathcal{M}$  around  $\mathbf{x}_i$ , we may rewrite eq. 29 as

$$\sum_j w_{ij}^{(\sigma_i)} dV_i \approx \int_{\mathcal{M}} \exp\left(\frac{-\|\mathbf{x}_i - \mathbf{x}_j\|^2}{\sigma_i^2}\right) d\mathbf{x}_j \quad (30)$$

when the sampling is approximately locally uniform. By further assuming that  $\sigma_i$  is small, and that  $\mathcal{M}$  can be well-approximated locally by its tangent space  $\mathbb{R}^d$ , then

$$\int_{\mathcal{M}} \exp\left(\frac{-\|\mathbf{x}_i - \mathbf{x}_j\|^2}{\sigma_i^2}\right) d\mathbf{x}_j \approx \int_{\mathbb{R}^d} \exp\left(\frac{-\|\mathbf{x}_i - \mathbf{x}_j\|^2}{\sigma_i^2}\right) d\mathbf{x}_j = (\sqrt{\pi}\sigma_i)^d, \quad (31)$$

so

$$\sum_j w_{ij}^{(\sigma_i)} dV_i \approx (\sqrt{\pi}\sigma_i)^d, \quad (32)$$

as shown in Fig. 17.

An analogous derivation for the discrete degree summation is as follows. First, note that the edge weight now is a constant = 1; it remains to determine its support over  $\mathcal{M}$ . From section 3.3.3, we know that, for simple manifolds with random sampling, the node degree  $\text{deg}(i)$  in a Gabriel graph is approximately  $2^{d_i}$  within a region of constant intrinsic dimensionality (where  $d_i$  denotes the local intrinsic dimensionality around  $\mathbf{x}_i$  (possibly different around other points in  $\mathcal{X}$ )<sup>5</sup>. In more general manifolds, we expect the converged graph  $G^*$  instead to approach such a property. This means  $\sum_j a_{ij} \approx 2^{d_i}$  will approximate the volume of a hyperrectangle (or box) of height = 1 and having a  $d_i$ -dimensional hypercube of side 2 as its base<sup>6</sup>. So, defining  $\rho_i$  as the radius of the local volume element  $dV_i$  (such that  $\rho_i = \sqrt{dV_i^d}$ ), then we may write:

$$\sum_j a_{ij} dV_i \approx \int_{-\rho_i}^{\rho_i} \cdots \int_{-\rho_i}^{\rho_i} 1 dx_{j_1} \cdots dx_{j_d} = (2\rho_i)^{d_i}, \quad (33)$$

<sup>5</sup>We abuse notation, therefore, when referring to a “ $d$ -dimensional manifold”, or when using the expression “ $\mathcal{M} \in \mathbb{R}^d$ ”.

<sup>6</sup>This agrees with our observation (section 3.3.3) that the unoccluded region around  $x_i$  is similar to a  $d$ -orthoplex: by placing a vertex (i.e., a neighbor) in each of its  $2^d$  facets we obtain a  $d$ -hypercube, which is the dual polytope of an orthoplex.

as illustrated in Fig. 17. Hence  $\rho_i$  is a kind of “neighborhood radius” of node  $i$ .

From eqs. 32 and 33, eq. 28 becomes

$$\frac{\sum_j w_{ij}^{(\sigma_i)}}{\sum_j a_{ij}} = \frac{\sum_j w_{ij}^{(\sigma_i)} dV_i}{\sum_j a_{ij} dV_i} \approx \left( \frac{\sqrt{\pi}\sigma_i}{2\rho_i} \right)^{d_i}, \quad (34)$$

representing the ratio between the volume of a Gaussian with scale  $\sigma_i$  and that of a box of side  $2\rho_i$  and height 1 (Fig. 17). As the algorithm approaches convergence, we expect  $\sigma_i \approx \rho_i$  (scales are compatible with neighborhood radius) and  $\deg(i)$  should approach the empirically-observed value  $2^{d_i}$  (number of neighbors in  $G$  is compatible with dimensionality of  $\mathcal{M}$ ), resulting in

$$\frac{\sum_j w_{ij}^{(\sigma_i)}}{\sum_j a_{ij}} \approx \left( \frac{\sqrt{\pi}}{2} \right)^{d_i}. \quad (35)$$

Finally, we can estimate  $d$  as

$$\tilde{d}_i \equiv \log_2 \sum_j a_{ij}, \quad (36)$$

based on the empirical distribution of node degrees in  $G^{(t)}$ . From this, we can compute a *normalized* volume ratio,  $\delta_i^{(t)}$ , by dividing  $\delta_i^{(t)}$  by the value from eq. 35:

$$\delta_i^{(t)} \equiv \frac{\sum_j w_{ij}^{(\sigma_i)}}{\sum_j a_{ij}} \left( \frac{2}{\sqrt{\pi}} \right)^{\tilde{d}_i}. \quad (37)$$

Nodes whose degree deviate from exactly  $2^{d_i}$  will, likewise, under- or overestimate the local dimensionality, so reasonable volume estimates are still obtained regardless. However, in order to avoid dimensionality less than 1 for connected nodes, in practice when  $\deg(i) = 1$  we replace  $\sum_j a_{ij}$  with  $\max\{2, \sum_j a_{ij}\}$ .

Thus, we expect  $\delta_i' \approx 1$  for points obeying  $\sigma_i \approx \rho_i$  and  $\tilde{d}_i \approx d_i$ . Crucially, points for which these conditions are not met (i.e., those having “wrong” neighbors in the original Gabriel graph  $G^{(0)}$ ) will depart from this by having  $\delta_i' > 1$ . In the next section, we shall use this quantity to guide a sparsification of edges in  $G^{(0)}$ .

Interestingly,  $\delta_i'$  can also be interpreted as measuring how well the scale  $\sigma_i$  fits the local volume element  $dV_i$  (or, equivalently, how it counteracts the local sampling density,  $1/dV_i$ ). Since  $dV_i = \rho_i^d$  (from the definition of  $\rho_i$ ), we may rewrite eq. 34 as:

$$\frac{\sum_j w_{ij}^{(\sigma_i)}}{\sum_j a_{ij}} \approx \frac{(\sqrt{\pi}\sigma_i)^{d_i}}{2^{d_i} dV_i}. \quad (38)$$

Finally, when  $\tilde{d}_i \approx d_i$  and relaxing the assumption  $\sigma_i \approx \rho_i$ , and summarizing the above we have:

**Remark 9:** A node’s *normalized volume ratio* at iteration  $t$ , is

$$\delta_i^{(t)} \equiv \frac{\sum_j w_{ij}^{(\sigma_i)}}{\sum_j a_{ij}} \left( \frac{2}{\sqrt{\pi}} \right)^{\tilde{d}_i} \approx \frac{(\sqrt{\pi}\sigma_i)^{d_i}}{2^{d_i} dV_i} \left( \frac{2}{\sqrt{\pi}} \right)^{\tilde{d}_i} \approx \frac{\sigma_i^{d_i}}{dV_i} \quad (39)$$

Therefore,  $\delta_i'$  can be thought of as the product between kernel scale and local density. When  $\sigma_i$  is optimal, it should be approximately equal to the inverse of the local density, so  $\delta_i' \approx 1$ .



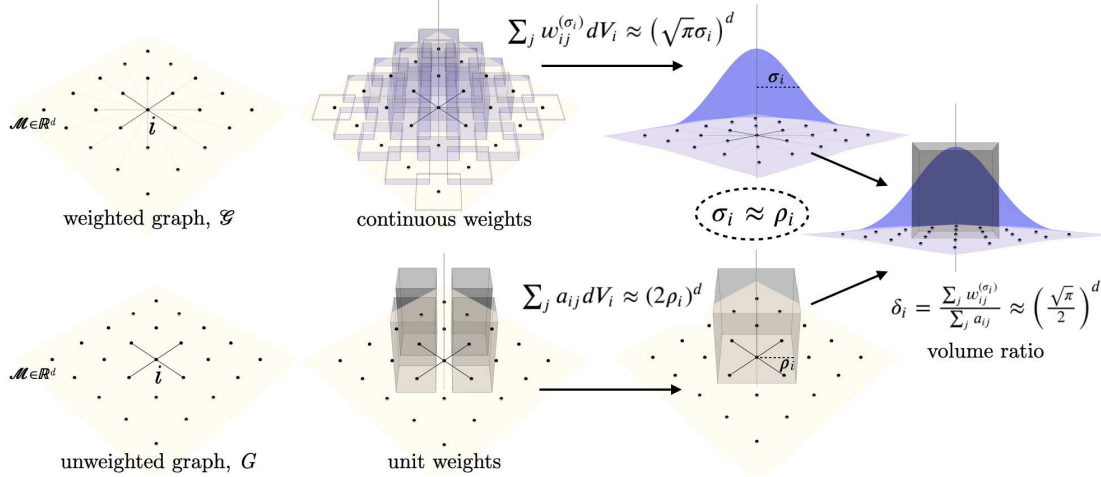


Figure 17: Computing the volume ratio between continuous and discrete degrees of a node  $i$  with neighboring points sampled uniformly over a  $d$ -dimensional manifold  $\mathcal{M}$ . *Top row*: Using a Gaussian kernel, the weighted degree of  $i$  (sum of kernel values  $\sum_j w_{ij}^{(\sigma_i)}$ ) in  $\mathcal{G}$  approximates the volume of a Gaussian with scale  $\sigma_i$  when sampling is locally uniform (eq. 32). *Bottom row*: The number of edges adjacent to  $i$  in  $G$  (sum of unit weights) approximates the volume of a box with unit height and a hypercube of side  $2\rho_i$  as its base, where  $\rho_i$  is the radius of a local volume element of  $\mathcal{M}$  around  $x_i$  (eq. 33). *Right*: When the scale  $\sigma_i$  is compatible with  $\rho_i$ , the volume ratio,  $\delta_i$ , is expected to be approximately  $\sqrt{\pi}/2$ , therefore it is a dimensionless and scale-invariant quantity.

### 3.5.2 Uniformity of sampling and edge pruning

Since  $\delta_i^{(t)}$  is evaluated for every node  $x_i$ , we can collect it across nodes and view it as a statistic. This has two consequences: (i) it can be used to enforce consistency in sampling and (ii) outliers in this statistic are likely candidates for edge pruning. We address consistency of sampling first.

We have several times stated that sampling is required to be locally uniform, although the rate may change over the manifold. Examples of this were shown in e.g. Fig. 11, where the sampling was denser in the center of the Gaussian than in the periphery. This example differs from the tessellations, in which all nearest neighbors had exactly the same distance. Putting this together, we have

**Remark 10: Locally Uniform Sampling** Let a node  $i$  have  $k_i$  neighbors in  $G^{(t)}$ . Among these, let  $r_i^{\text{FN}}$  denote the distance from  $i$  to its furthest neighbor, and  $r_i^{\text{NN}}$  to its nearest neighbor. When  $r_i^{\text{FN}} \approx r_i^{\text{NN}}$  for all points  $x_i$  in the dataset, we say the sampling is locally uniform.

This is useful because a departure from the assumption that sampling is locally uniform will cause  $\delta_i'$  to be on average greater than 1 throughout the dataset. To see this, when sampling is not uniform, we have  $r_i^{\text{FN}} > r_i^{\text{NN}}$ . Now, since  $\sigma_i$  is optimized to cover all of  $i$ 's neighbors, it will have in most cases the same order of magnitude as  $r_i^{\text{FN}}$  (minus some possible slack due to the multi-scale interaction). Therefore, the higher the variability in the neighbors' distances, the larger the difference between  $r_i^{\text{FN}}$  and  $r_i^{\text{NN}}$  making, in turn,  $\sigma_i$  larger than the distance to most neighbors of  $i$ .

Ultimately this will increase  $\sum_j w_{ij}^{(\sigma_i)}$  beyond what we would have in a uniform-sampling scenario (in which  $r_i^{\text{FN}} \approx r_i^{\text{NN}}$ ).

When data are acquired using a global sampling strategy, this variability in the neighbors' distances should be roughly constant throughout the dataset (rather than the distances). So we use the scalar parameter  $C$  from eq. 19 to correct for this “bias” and bring the median of the distribution of  $\delta_i^{(t)}$  (denoted as  $\langle \delta_i^{(t)} \rangle$ ) close to 1<sup>7</sup>.

**Remark 11:** Let the tuned  $C^{*(t)}$  be that which causes  $\langle \delta_i^{(t)} \rangle$  to be closest to 1.

Typically,  $C^{(t)} < 1$ , which, in the scale optimization procedure, means the covering constraints (eq. 22) are being relaxed using the distribution of  $\delta_i'$  as a guide (Fig. 18). (Although the tuning of  $C$  is not necessary for finding candidates for sparsification, it attributes a quantitative meaning to the value of  $\delta_i'$ , so any  $\delta_i' \gg 1$  is guaranteed to indicate the need for edge pruning.)

Such tuning should be performed at  $t = 0$ , and repeated as needed over the iterations whenever  $\langle \delta_i^{(t)} \rangle$  deviates too much from unity (which may happen after several edges have been pruned). Most commonly, we find  $0.5 < C^{*(t)} < 1$ .

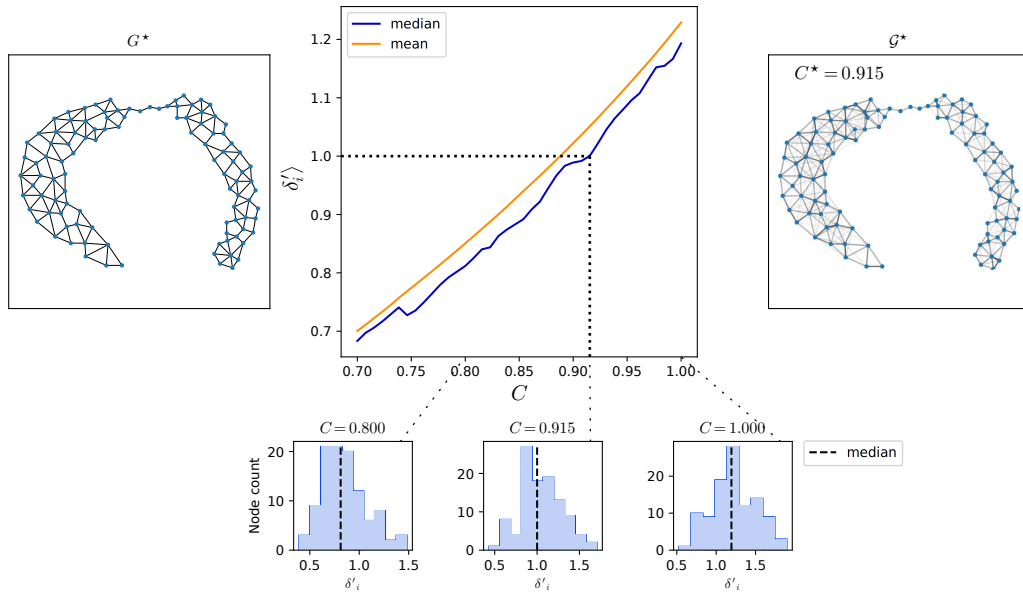


Figure 18: Tuning the hyperparameter  $C$  based on the median of the distribution of normalized volume ratios,  $\langle \delta_i' \rangle$ . *Left:* Converged unweighted graph  $G^*$  obtained for the dataset from Fig. 19. *Center:* After computing  $\langle \delta_i' \rangle$  for a range of values of  $C \leq 1$ , the optimal  $C^*$  is that resulting in a  $\langle \delta_i' \rangle$  closest to 1. Histograms below show distribution of  $\delta_i'$  for different values of  $C$ , including  $C^* = 0.915$ . *Right:* The resulting weighted graph  $G^*$  after  $C$ -tuning typically exhibits a more uniform connectivity throughout (see Fig. 13).

Thus we have a data-driven way of finding an appropriate value for  $C$ . Because it is a global constant applied to all connection constraints, it shifts the distribution of  $\delta_i'$  to a median around 1

<sup>7</sup>Although the mean typically gives smoother tuning curves (see Fig. 18), the median is more robust. This matters, because of the possible outlying  $\delta_i'$  values.

without changing its general shape. This leads us to the second use of the  $\delta'$  statistic: a node whose variability of neighbor distances is much greater than the median (i.e., has a farthest neighbor considerably more distant than their median neighbor) will still have  $\langle \delta_i'^{(t)} \rangle \gg 1$ , but will have significant outliers. It is these outliers that are candidates for having edges that need to be pruned in the sparsification step.

**Remark 12:** Nodes that are robust outliers in the  $\delta$  statistic have an overly distant neighbor, relative to the other neighbors for that node, and hence are likely to be in violation of reach or other geometric constraints. These *relatively distant neighbors* are candidates for pruning.

Given the distribution of normalized volume ratios, robust statistics suggest models for spread and outliers. We take this to define a threshold, and nodes with  $\delta_i'$  above such threshold should have their connection to farthest neighbors deleted. Ideally, only one such connection should be pruned after each iteration; however, should that become impractical with datasets, a compromise is to limit the pruning, at each iteration, to a single edge from each node that is above the threshold.

It is possible that datasets with a large number of problematic connections will exhibit a heavy tail or may look like a mixture of two distributions (cf. example in Fig. 22), so using the distribution's quartiles may give a more robust result. One option that seems to work particularly well is to use estimates of the mean and standard deviation from the quartiles, as in [105] – throughout, we make use of the C3 method derived therein. Finally, we note that our algorithm can be run interactively, so the user can analyze the histogram of the distribution after each iteration to judge whether the choice of threshold is reasonable and thus be confident in the results.

### 3.5.3 Convergence

The algorithm converges at iteration  $t$  when no point  $x_i$  has an outlying  $\delta_i'^{(t)}$  (i.e., greater than a statistical threshold). This implies that no edges will be pruned, so  $G^{(t+1)} = G^{(t)}$  and therefore no further changes can occur to either  $\sigma^{(t)}$  or  $\mathcal{G}^{(t)}$ . Note that convergence is guaranteed—since at every iteration  $t$  an edge is removed, the algorithm must necessarily reach a certain  $t$  at which all outliers (if there were any to begin with) have been pruned.

If one is solely interested in obtaining  $\mathcal{G}^*$  (i.e., not interested in  $G^*$ ), an alternative convergence condition may be adopted that looks at the distribution of the (normalized) *multi-scale volume ratio*,  $\delta_{i_{\text{MS}}}^{(t)}$ :

$$\delta_{i_{\text{MS}}}^{(t)} \equiv \frac{\sum_j w_{ij}}{\sum_j a_{ij}} \left( \frac{2}{\sqrt{\pi}} \right)^{\bar{d}_i}, \quad (40)$$

analogous to eq. 37 but using the weights from  $\mathcal{G}^{(t)}$  directly. Since the multi-scale kernel values take into account the interaction between individual scales, the distribution of  $\delta_{i_{\text{MS}}}^{(t)}$  will be typically tighter than that of  $\delta_i'$  (i.e., some of the excessively large scales might be compensated by small neighboring scales). Therefore, one may wish to allow for an earlier convergence when there are no remaining outliers in the distribution of  $\delta_{i_{\text{MS}}}^{(t)}$ .

In closing this section, we return to the introductory examples and show the graphs for the *sampling Swiss cheese* patterns (Fig. 2) in Fig. 23. Finally, should it be required that  $G^*$  be connected,

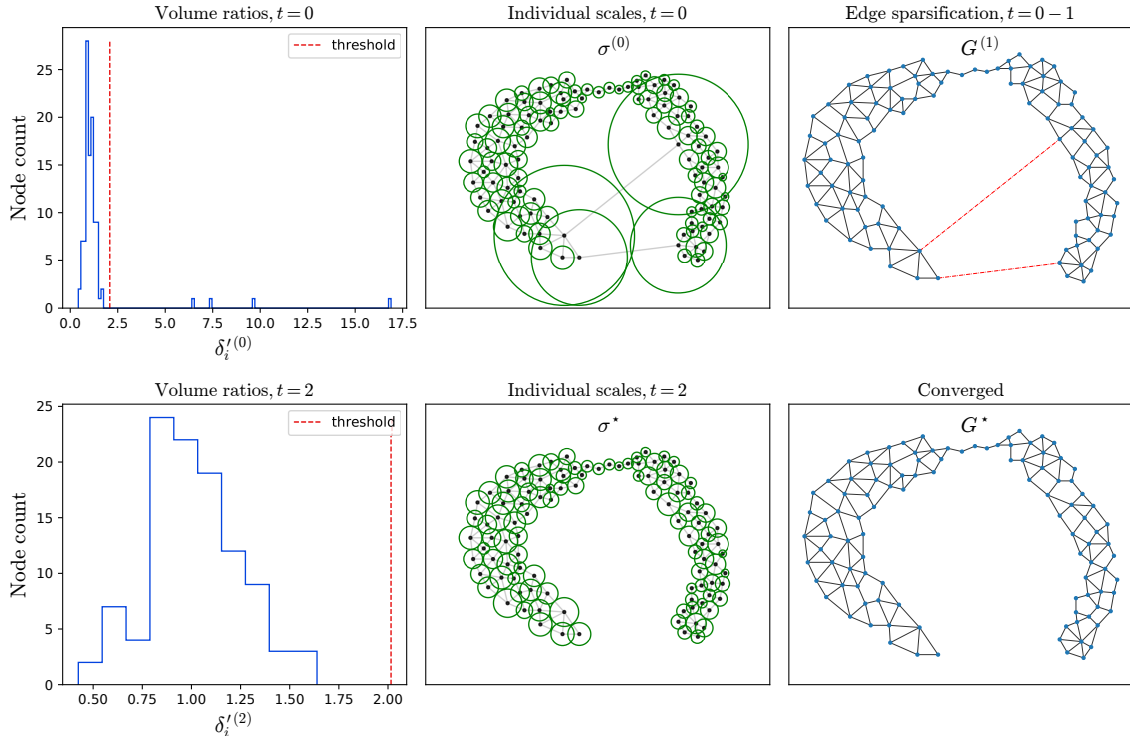


Figure 19: Optimal scales and associated normalized volume ratios at iterations 0 and 2 of Algorithm 1 on the horseshoe dataset (see Fig. 13). Top row: the  $\delta_i$  statistic has median around 1 and several outliers. These are caused by the long edge (and huge scales) (middle). Right column:  $G^{(t)}$  after iteration 1, with edges deleted so far shown in red (top), and after iteration 2 (bottom).

pruning can be stopped at that point. Naturally,  $\mathcal{G}^*$  is always connected up to machine precision, or some numerical tolerance.

### 3.6 Comparison with other kernel methods

Here we compare the data graphs obtained using our method (IAN) with those from other popular manifold learning methods. To start we introduce a synthetic “stingray” dataset that exhibits a transition of apparent dimensionality from 2 (body) to 1 (tail), cf. Fig. 4. Points were uniformly sampled with 20% deleted at random.

Our unweighted graph  $G^*$  can be compared with the  $k$ -NN graph (bottom row in Fig. 24), used in a variety of methods including Isomap[96], which will be further examined in section 4. When  $k = 2$ , the tail exhibits perfect connectivity, but the body is too sparse. If  $k = 4$ , the body is more properly connected but the tail is overly connected, and “short-circuits” start to appear. Finally, for  $k \geq 8$  the connectivity is inappropriate as the tip of the tail connects directly to the body.

In contrast,  $G^*$  manages to retain a minimally-connected tail while covering the body almost everywhere, creating edges across many of the sampling gaps (compare with the holes that remain in the  $k$ -NN graph with  $k = 4$ , some of which are present even when  $k = 8$ ).

Our weighted graph  $\mathcal{G}^*$  can be compared against methods that use a Gaussian-like kernel, and where each point has an individual scale. These methods were described in Sec. 2.1: t-SNE [101],

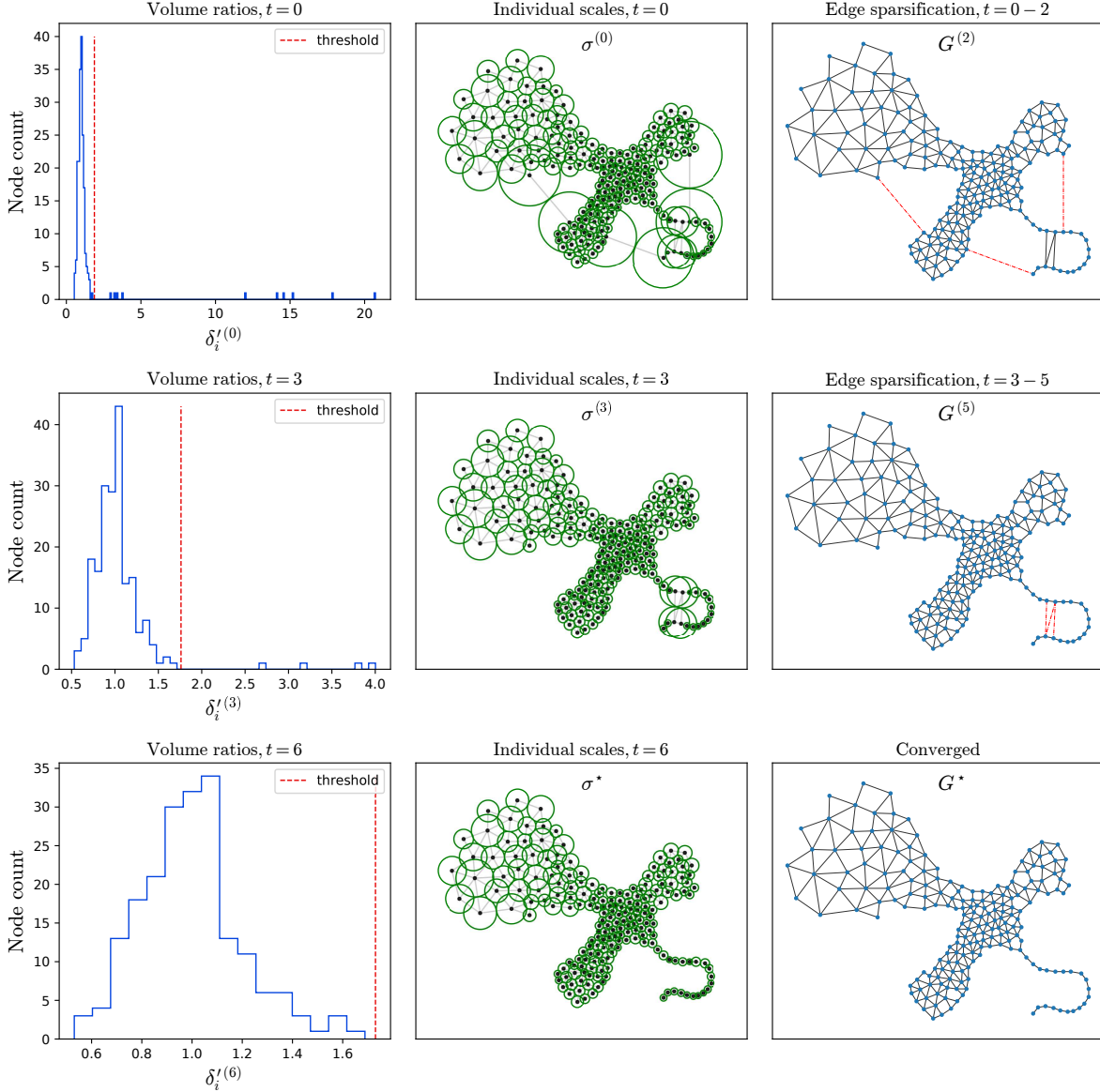


Figure 20: Optimal scales and associated normalized volume ratios at different iterations of Algorithm 1 on the “limbs” dataset from Fig. 6. The distribution of  $\delta'_i$  (left) indicates those connections that are least likely to represent (reasonable) geodesics over the underlying manifold. Right column shows  $G^{(t)}$  after iterations 2, 5 and 6 (deleted edges in red).

UMAP [78], self-tuning[111], and variable-bandwidth[16, 17]; their resulting connectivity can be visualized in Fig. 24, where edges have transparency proportional to their weight.

We also plot the respective individual scales resultant from each method (Fig. 25). They are represented, around each point  $i$ , as level set corresponding to a kernel value of 0.75. For the asymmetric kernels of t-SNE and UMAP this is straightforward; for the multi-scale kernels (self-tuning, variable-bandwidth, and our own), we replace the product  $\sigma_i \sigma_j$  by  $\sigma_i^2$ .

At the top of both Fig. 25, we see that the scales found by our method seem to nicely conform to the space between each point and its neighbors. Especially illuminating is what happens along

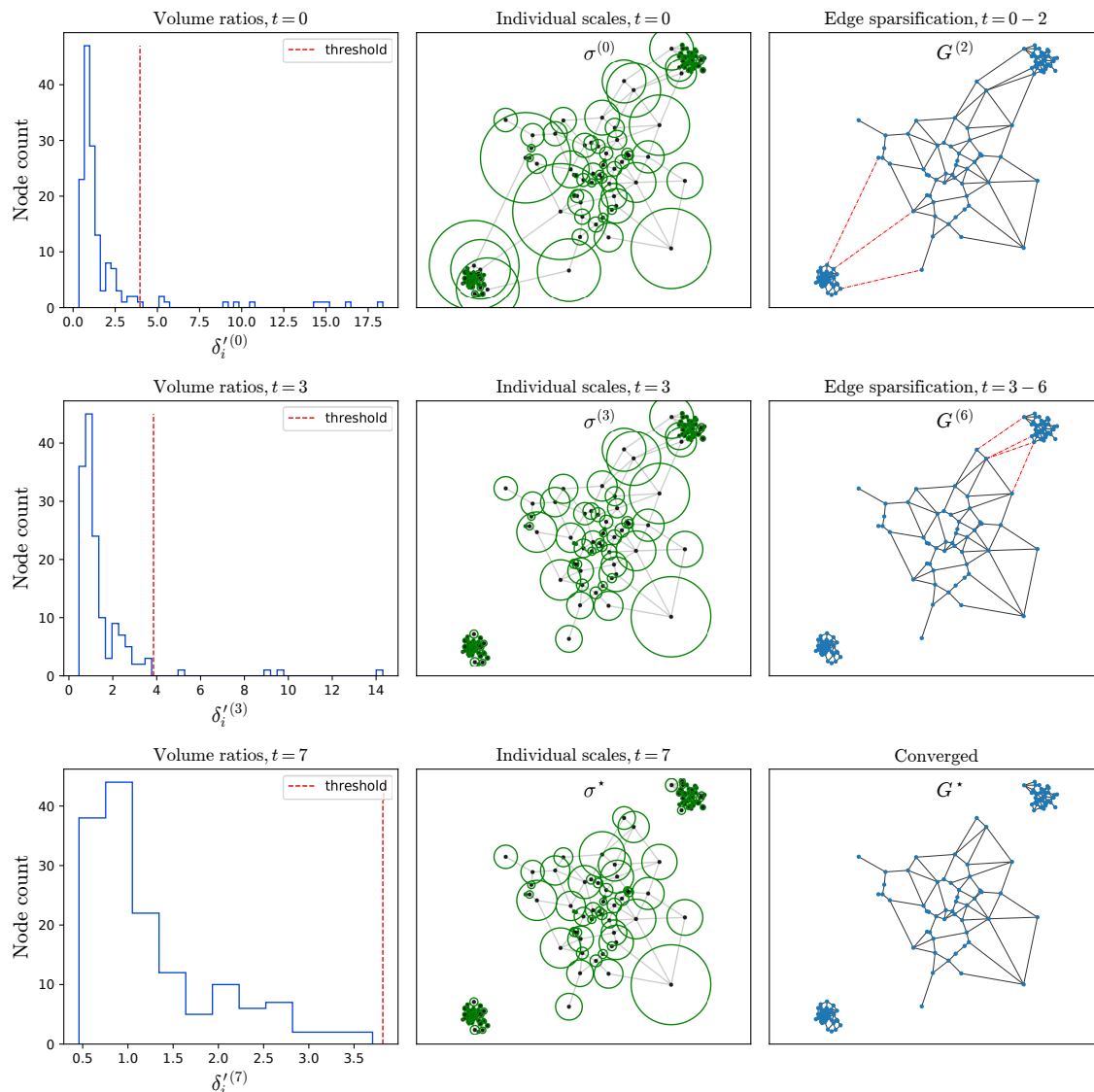


Figure 21: Optimal scales and associated volume ratio statistics at different iterations of Algorithm 1 on the clustered dataset from Fig. 6. Pruned edges (in red) are precisely those connecting the three clusters.

the tail, where scales either “expand” or “shrink” so as to minimally cover the spaces between neighboring points, thus illustrating what our scale optimization achieves.

Among the other methods, with few exceptions the scales seem to cover either too much (collapsing the tail on itself) or too little (leaving holes in the body). The weighted graphs in Fig. 24 reveal the result of the interaction between these individual scales (namely, the edge weights). Our  $G^*$  (top right) manages to cover almost the entire body with edges, while keeping the tail minimally connected—in fact, resembling the unweighted version in  $G^*$ , and therefore respecting the original curvature and reach. Other methods, in contrast, have a hard time achieving both things with a single value for  $k$ . In t-SNE, the scales over the body are much too small when  $k \leq 4$ ; so its weighted graph look too sparse; for  $k \geq 8$  the scales over the tail become too large, and therefore

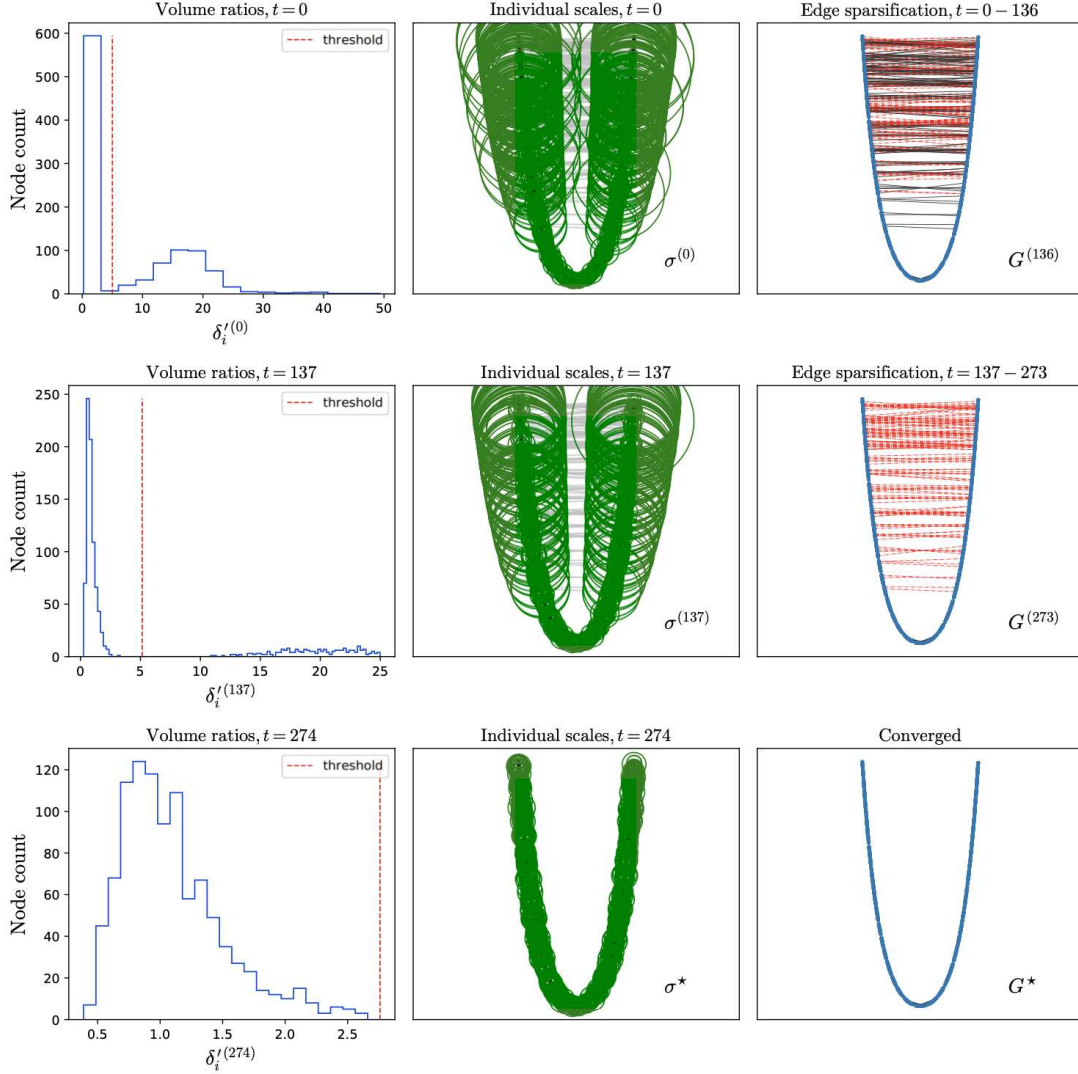


Figure 22: Optimal scales and associated normalized volume ratios  $\delta'_i$  after each iteration of the algorithm on the bent plane dataset used in Fig. 28 (here, seen from a lateral view). The number of initial connections in  $G^{(0)}$  (Gabriel graph) is very large, so initial distribution of  $\delta'_i$  shows two modes. However, ratios in right-side peak are very high, and are therefore easily identified as outliers when compared to the mean. The algorithm terminates soon after all edges crossing the gap are eliminated.

strong edges appear connecting it to the body. In UMAP, the scales do not grow as much with increasing  $k$ , but at  $k = 4$  the body in the weighted graph is still too sparse, while for  $k \geq 8$  the tail is strongly connected to the body. With self-tuning, scales seem to grow faster with  $k$ , while with variable-bandwidth this growth is somewhat counteracted by the action of their global scale  $\epsilon$  (eq. 7). In fact, the graph that most resembles our own  $G^*$  is the one using the variable-bandwidth kernel with  $k = 2$ , the main difference being that the big sampling gap near the tip of the body is poorly connected, while in our case it is slightly overly connected (due to connections in  $G^*$  crossing that gap).

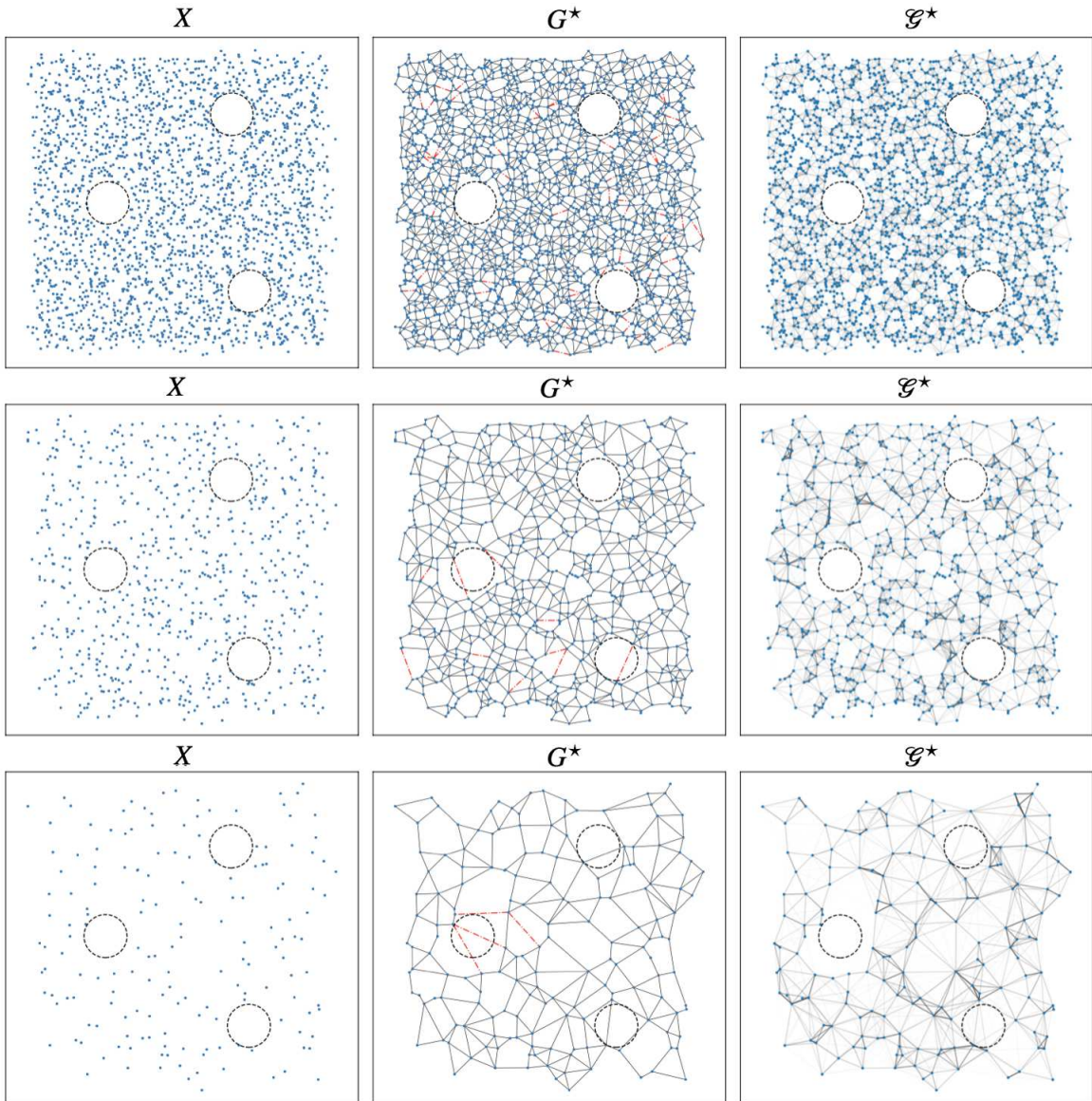


Figure 23: Sampled Swiss cheese results (cf. Fig. 2). The original sampled points (holes outlined) are shown, together with the converged graphs. In the sparse case the sampling is locally uniform, and no holes are visible, while in the dense case no holes are violated.



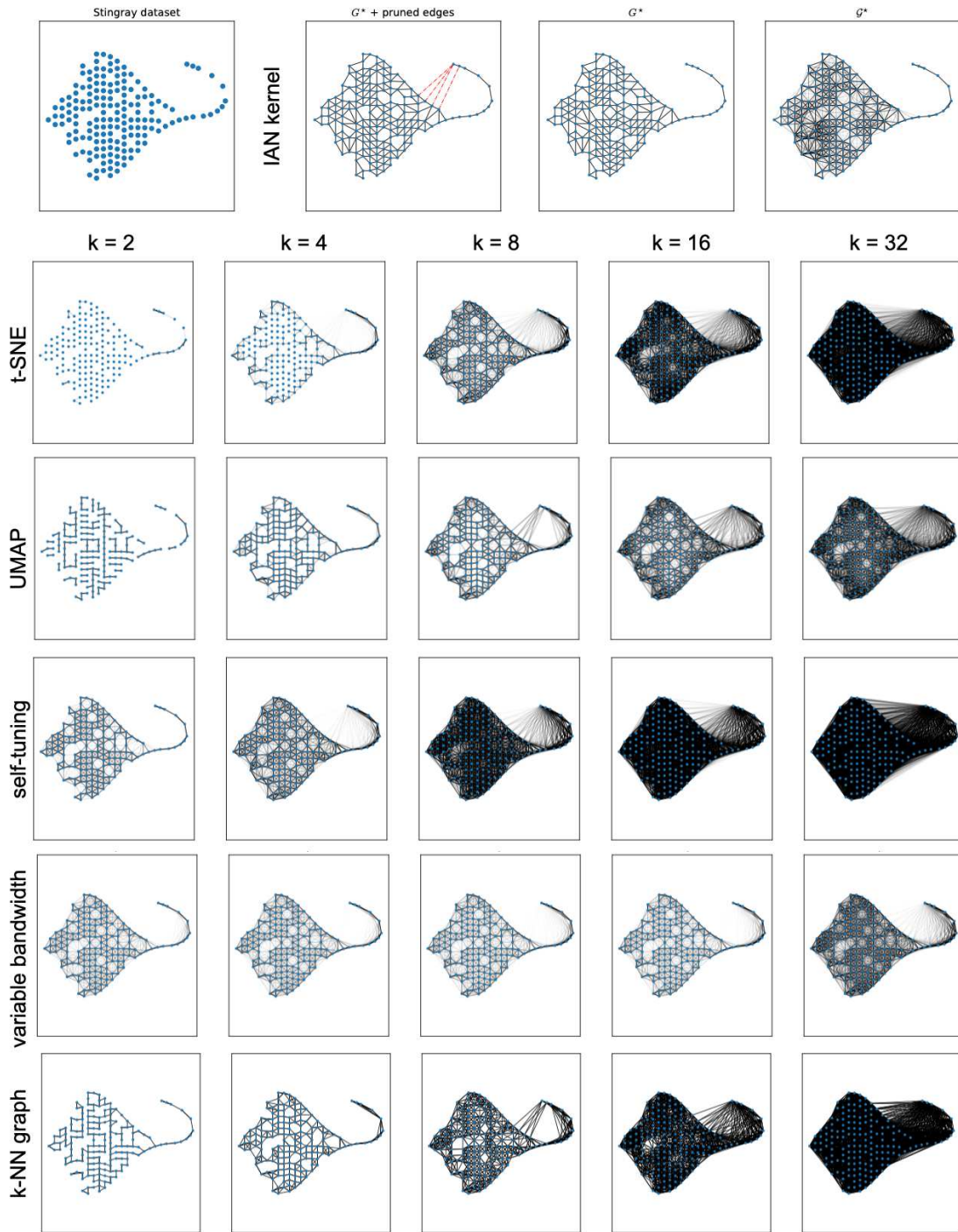


Figure 24: *Top*: The stingray dataset and its converged graphs  $G^*$  and  $\mathcal{G}^*$ ; pruned edges are shown in red. *Bottom*: Other algorithms produce qualitatively different graphs depending on the neighborhood size parameter,  $k$ . All graphs shown are weighted (using a continuous kernel) except for the  $k$ -nearest-neighbors graph (bottom row). Edge weights are visualized as the intensity of the line segments (each  $w_{ij}$  is divided by the kernel value when  $r_{ij}$  equals the scale, for a fair comparison across algorithms).

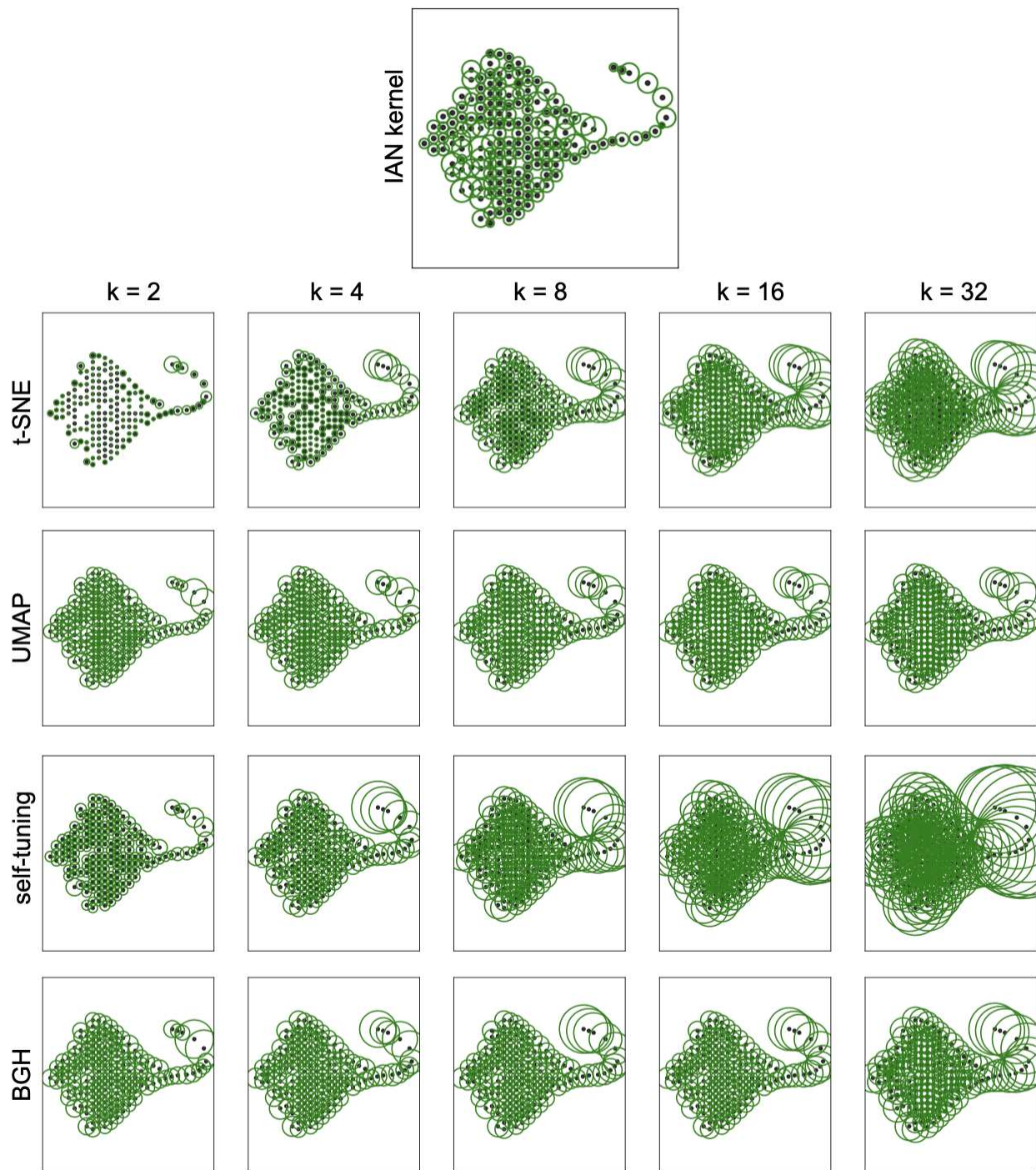


Figure 25: Individual scales obtained using our algorithm (top) compared to other methods (bottom table), as represented by their level sets for a (single-scale) kernel value of 0.75.

## 4 Applications

We now provide examples of application of our kernel to three different manifold learning tasks: dimensionality reduction, by means of non-linear embedding algorithms; geodesic estimation, which typically finds application in computational geometry, vision, and graphics; and local intrinsic dimensionality estimation.

### 4.1 Low-dimensional embeddings

Dimensionality reduction is now ubiquitous in visualization of high-dimensional data. Several methods exist[93, 102, 70, 51], and most of the non-linear methods are manifold-based[88, 96, 78, 58, 101, 89, 112, 10, 28, 37, 109, 81, 95]: given a collection of points in high-dimensional space sampled from a low-dimensional manifold  $\mathcal{M}$ , the goal is to find a good parametrization for the data in terms of intrinsic coordinates over  $\mathcal{M}$ , which in turn can be used to produce a low-dimensional embedding.

In surveying the literature, it is common to find a heuristic or range of values suggested for choosing the neighborhood radius or size, but rarely do we see examples of the sensitivity of the results to that choice. In this section, we ran a few of the most popular methods using a wide range of values for the kernel scale parameter  $k$ , and furthermore compared their results when using our own kernel.

We have limited our comparison to embedding methods that use a neighborhood kernel and for which pairwise information is sufficient as input (i.e., do not require positional information): diffusion maps[28, 29, 30], Isomap[96], t-SNE[101], and UMAP[78]. As shown in Figs. 26–28, results can vary qualitatively depending on the choice of the scale parameter  $k$ . Five values of  $k$  were tested on three synthetic datasets, spanning a wide range of scales and different geometries.

#### 4.1.1 Diffusion maps + self-tuning kernel

Diffusion maps are based on the spectral properties of the random walk matrix (normalized graph Laplacian) over the weighted data graph; integration over all paths in the graph makes diffusion distances in principle more robust to “short-circuiting” than graph geodesics. For better comparison with our own kernel, instead of the standard single-scale Gaussian kernel we use the self-tuning approach of [111] (eq. 6). Our kernel was applied to diffusion maps by directly using  $\mathcal{G}^*$  as the similarity matrix (weighted adjacency matrix), and by setting the additional parameters  $\alpha = 1$  and  $t = 1$ .

With the stingray dataset (Fig. 26, we see that the fully-extended tail at  $k = 2$  becomes progressively more folded and compressed as  $k$  increases. The body is overly contracted at  $k = 2$  but expands with larger  $k$ . Using our own  $\mathcal{G}^*$ , although we obtain excellent embeddings of both body and tail (right-most column), they are represented by separate sets of coordinates (two for the body, and a third for the tail), which happens due to the change in dimensionality. The plot shows a 2-D projection of the 3-D embedding.

When applied to the spiral dataset (Fig. 26), only  $k = 2$  and 4 were able to prevent folding. The bent plane (Fig. 28) was more tolerant, with good results for all  $k$  except 64, for which the plane remained folded. When using our own kernel, a good parametrization was obtained for both datasets.

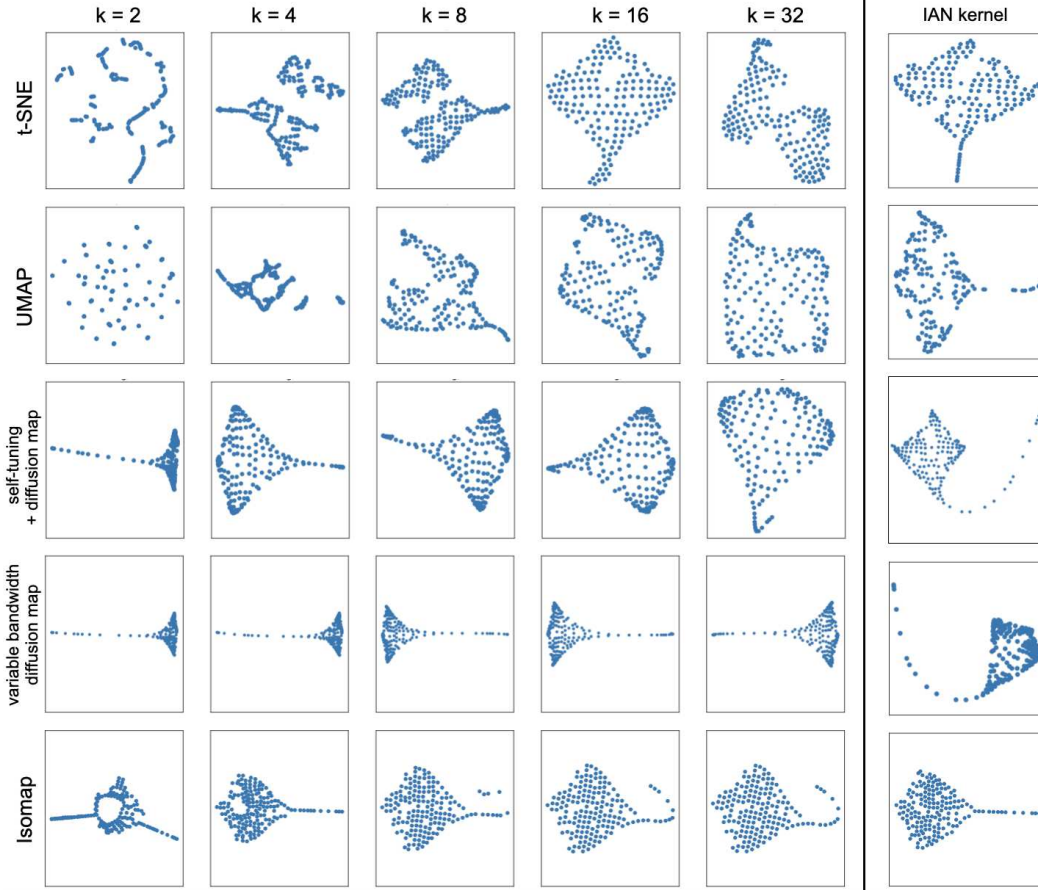


Figure 26: Running different embedding algorithms on the “stingray” dataset (see Fig. 24). Different choices of the neighborhood size,  $k$ , may produce qualitatively different results, depending on the algorithm. Running those same algorithms using our IAN kernel (right) typically gives a reasonable result. Refer to main text for details.

#### 4.1.2 Variable bandwidth diffusion embedding

We also tested a variant of diffusion maps using the variable bandwidth kernel of [16, 17], in which a distinct type of multi-scale kernel is proposed along with a specific normalization of the weighted graph Laplacian. Because it computes an additional global scale  $\epsilon$  based on the individual scales, in order to apply our algorithm to this method we replaced the density estimates  $q_\epsilon$  (eq. 7) with the inverse of our optimal scales. We used  $\alpha = 0$  and  $\beta = -1/2$ , cf. recommended in [17]; eigenvectors were scaled by the square-root of the inverse of their respective eigenvalues [91, 85], following the implementation in [8].

This method produced good embeddings for the stingray, especially for  $k = 8$  (Fig. 26). For the spiral (Fig. 27), using  $k \leq 8$  caused some points to drift apart, and although it returned basically the original curve when  $k = 16$  or  $32$ , a spectral algorithm is expected to “unroll” the spiral, finding a good (1-D) parametrization of it.

The same happened with the bent plane (Fig. 28), which could not be embedded into 2 coordinates for any choice of  $k$ . Using our scales, however, the algorithm managed to find appropriate parametrizations for all three datasets.

### 4.1.3 Isomap

Isomap applies classical multidimensional scaling (MDS) to geodesic distances computed as shortest paths over a  $k$ -nearest neighbors graph (eq. 2). Because the graph is unweighted, this method is particularly sensitive to the choice of  $k$ . Our kernel applied to Isomap by directly replacing the  $k$ -nearest neighbors graph with  $G^*$ .

With the stingray (Fig. 26), Isomap produced a good embedding with  $k = 4$ . The result with  $k = 2$  was completely wrong (an additional tail appears), and with  $k = 8$  the tip of the tail is disconnected. With  $k = 16$  and  $32$ , it essentially returns the original data, without any dimensionality reduction. Using our  $G^*$ , the result of  $k = 4$  was improved by making the points in the body more uniformly spread.

The spiral (Fig. 27) is properly embedded (1-dimensional) only when  $k$  is 2 or 4, while with the bent plane (Fig. 28) a good result is obtained for  $k$  between 4 and 16 ( $k = 2$  produces 1-dimensional curves and  $k = 64$  distorts the unfolding into 2-D). Using our  $G^*$  produces the correct mapping in either case.

### 4.1.4 t-SNE and UMAP

t-SNE and UMAP are related methods that have gained popularity in recent years[9]. Both compute similarities between data points by using individual scales based on  $\log_2 k$  (section 2.1), and adopt a second kernel to compute similarities between embedded points—t-SNE uses a Student t-distribution (Cauchy kernel); UMAP uses a non-normalized variant requiring a hyperparameter, `min_dist`. In t-SNE, embedding coordinates are initialized at random, while UMAP adopts the strategy of refining an initial spectral embedding. Both then optimize their embeddings by running gradient descent on an information-theoretic cost function between similarities in input space and embedded space: t-SNE minimizes the KL-divergence, while UMAP uses a variant of cross-entropy. Alternative initializations are typically used with t-SNE (e.g., PCA) to improve results[64, 65, 73]—in our experiments, for better comparison with UMAP, we used a spectral embedding initialization computed from its own symmetrized similarity matrix (eq. 10).

Our kernel was applied to t-SNE by replacing the individual scales (eq. 8) with those in  $\sigma^*$ ; with UMAP, because a different kernel function is used, we directly replaced the weighted graph (with adjacency given by  $U$  in eq. 12) with our  $G^*$ .

t-SNE was executed for 3000 iterations assigning the various  $k$  values to the perplexity parameter, leaving the remaining parameters to their defaults in the scikit-learn implementation[86] (Barnes-Hut method[100] for cylinder dataset; ‘exact’ method for all others); in UMAP, the `n_neighbors` parameter was set to  $k$ , with remaining parameters using default values (in particular, `min_dist` = 0.1). Because of the stochastic nature of both algorithms (even when using a fixed initialization), different runs will produce slightly different results—in order to avoid “cherry-picking” (unrealistic in a truly unsupervised scenario), both algorithms were executed a single time, using the same random seed.

Results for the stingray (Fig. 26) were quite analogous between the two algorithms: both produced artificial clustering for  $k \leq 8$ , while for  $k \geq 16$  the tail began to fuse with the body. The gaps in sampling within the body were accentuated by both algorithm, even at  $k = 32$ , where we see a big hole in the UMAP embedding, and in t-SNE it almost breaks into two pieces (despite the large neighborhood size). This example is illustrative of how much an embedding algorithm based

on attractive *vs.* repulsive forces can end up exaggerating nonuniform sampling.

The spiral (Fig. 27) was broken into pieces by t-SNE for all values of  $k$  except 8. UMAP produced reasonable results when  $k = 4$  or 8; however, when  $k = 2$  a multitude of clusters was obtained, and when  $k \geq 16$  the curve twisted over itself. Using our kernel (right-most column) produced a connected, non-self-intersecting curve. Neither algorithm was capable of returning a good arc-length parametrization of the spiral, however.

With the bent plane (Fig. 28), although both algorithms succeeded in unfolding it, t-SNE was only able to produce a fully two-dimensional plane (with no gaps) when setting  $k = 32$  (not shown) or 64, while UMAP required  $k \geq 16$ . Both gave reasonable results using our kernel.

#### 4.1.5 A higher dimensional example

Because all of the examples above have  $d \leq 2$ , we also tested our kernel when applied to a higher dimensional manifold, namely a 5-dimensional cylinder ( $\mathbb{R}^1 \times S^4$ ) with radius = 1 and length = 3 sampled uniformly at random ( $N = 8403$ , ambient space  $\mathbb{R}^6$ ). On the other hand, to simplify interpretation we used a pure, connected manifold with no bottlenecks and low curvature.

Fig. 29 shows two-dimensional embeddings obtained using our kernel with different algorithms. Although all correctly produced an oblong, various degrees of mixing of the original color labels were observed, and can be used to qualitatively indicate the quality of the embedding schemes. A quantitative assessment was computed as the rank correlation coefficient (Kendall’s  $\tau$ )[61, 63] between the ranking (positional order) of each point along the main axis in the original *vs.* embedded space.

Use of our IAN kernel gave similar or better results with both t-SNE and UMAP ( $k = 27$  was set as the mean degree in  $G^*$ , compatible with  $d = 5$ ). Both, despite their current popularity (e.g., [9, 65, 108, 64, 27, 47, 6, 36, 107]) produced considerably jittered outputs, implying that the original neighborhoods were not preserved. This appears to be caused by an attempt to reproduce the spherical shape of the cylinder’s base along the main axis, to different “slices” are projected on top of one another. However, UMAP produced nearly identical results even when the set to return the 6 components (as in the original space).

Diffusion maps using IAN resulted in very little mixing except near the boundaries, so neighborhoods were better preserved. Running it with either of the kernels discussed above using  $k = 27$  gave comparable results (not shown). Isomap also produced excellent results, with  $\tau = 0.98$  (not shown); although, because there is no ambient noise added to the data nor bottlenecks, choosing  $k$  large would trivially produce perfect results.

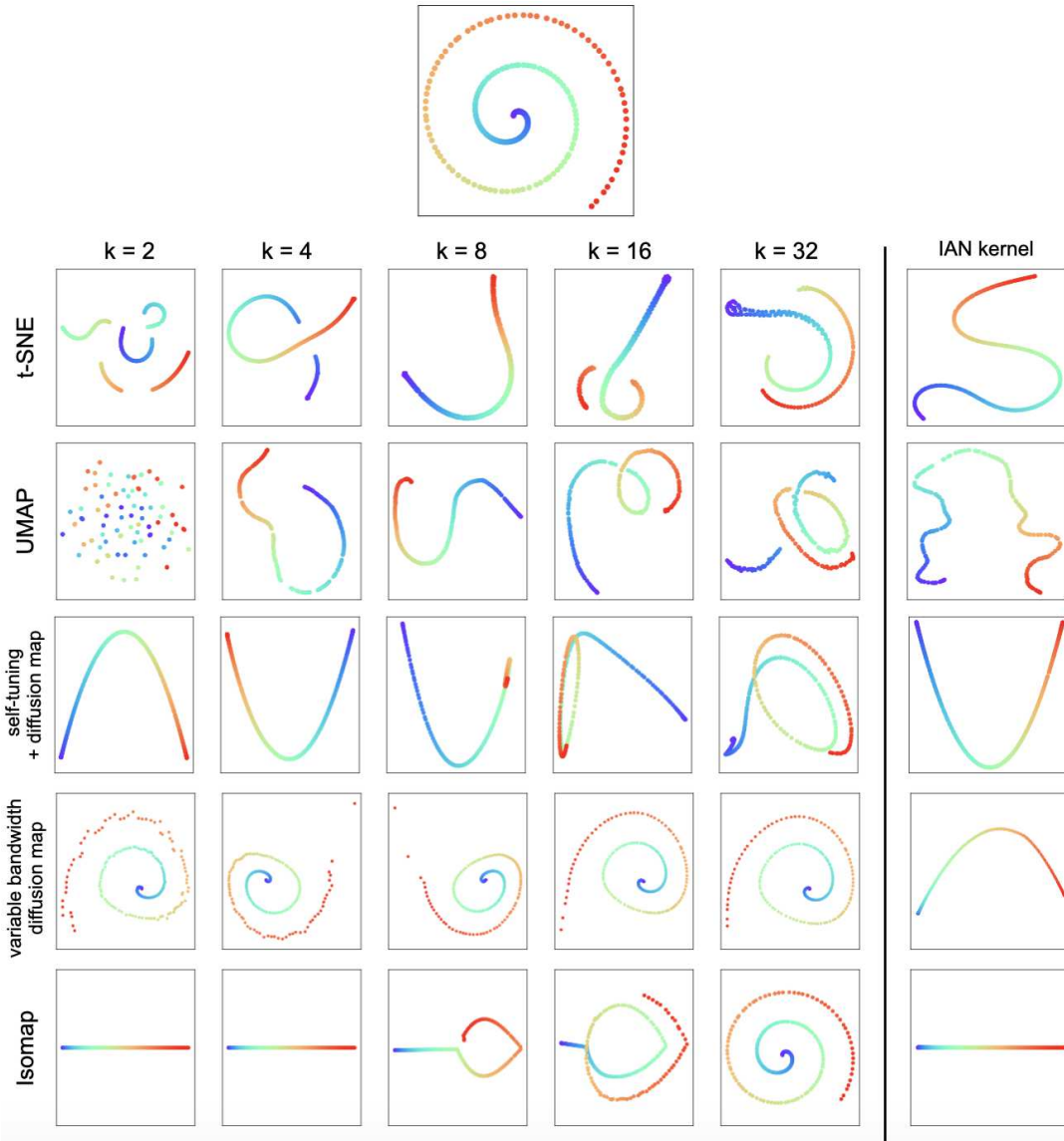


Figure 27: Running different embedding algorithms on the spiral dataset (top), in which points are sampled from a unit-speed parametrized Archimedean spiral. Different choices of the neighborhood size,  $k$ , may produce qualitatively different results, depending on the algorithm. Running those same algorithms using our IAN kernel (right) typically gives a reasonable result. Refer to main text for details.

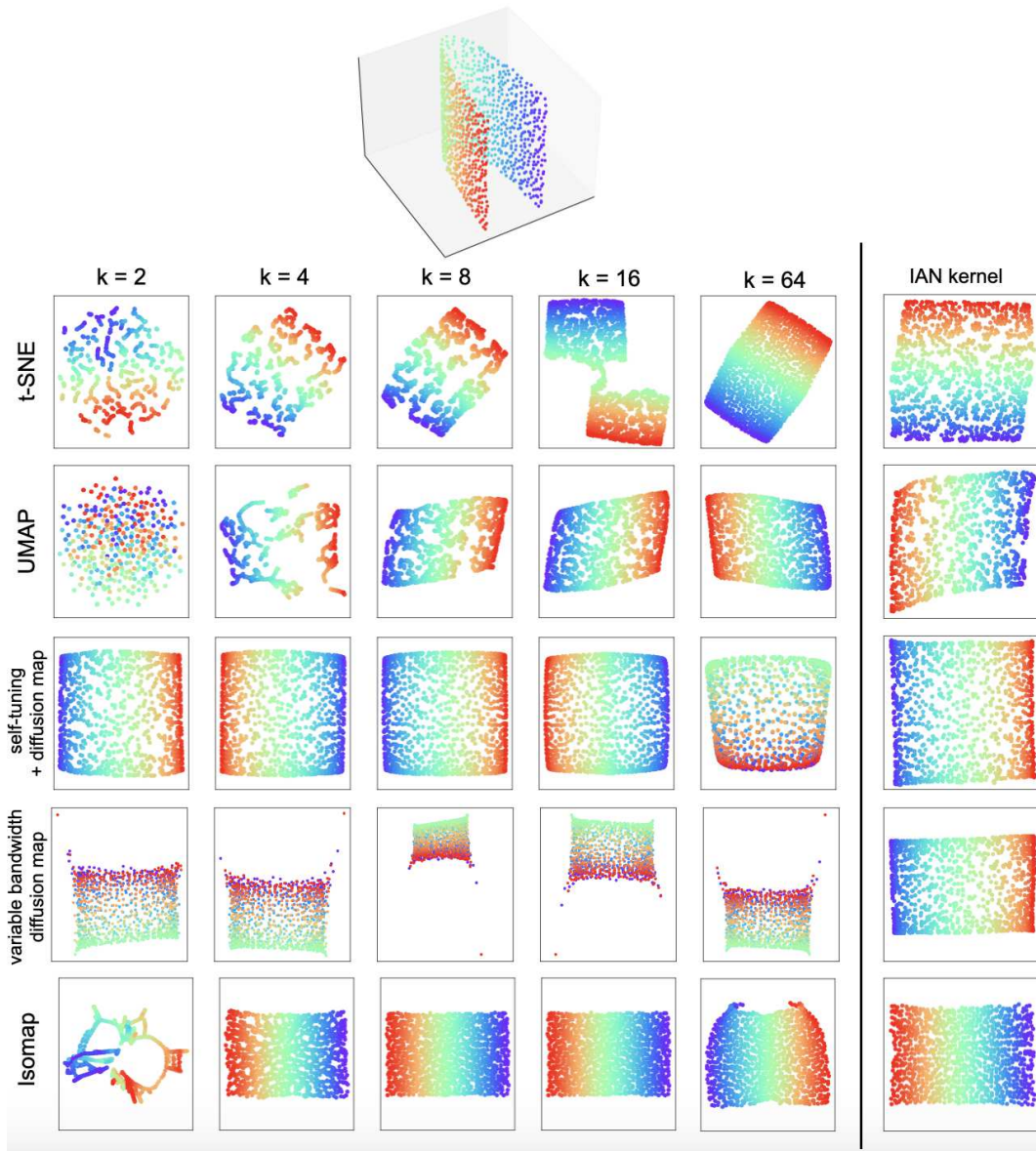


Figure 28: Running different embedding algorithms on the “bent plane” dataset (top), generated by extending a unit-speed parametrized catenary curve into two dimensions. Different choices of the neighborhood size,  $k$ , may produce qualitatively different results, depending on the algorithm. Running those same algorithms using our IAN kernel (right) typically gives a reasonable result. Refer to main text for details.



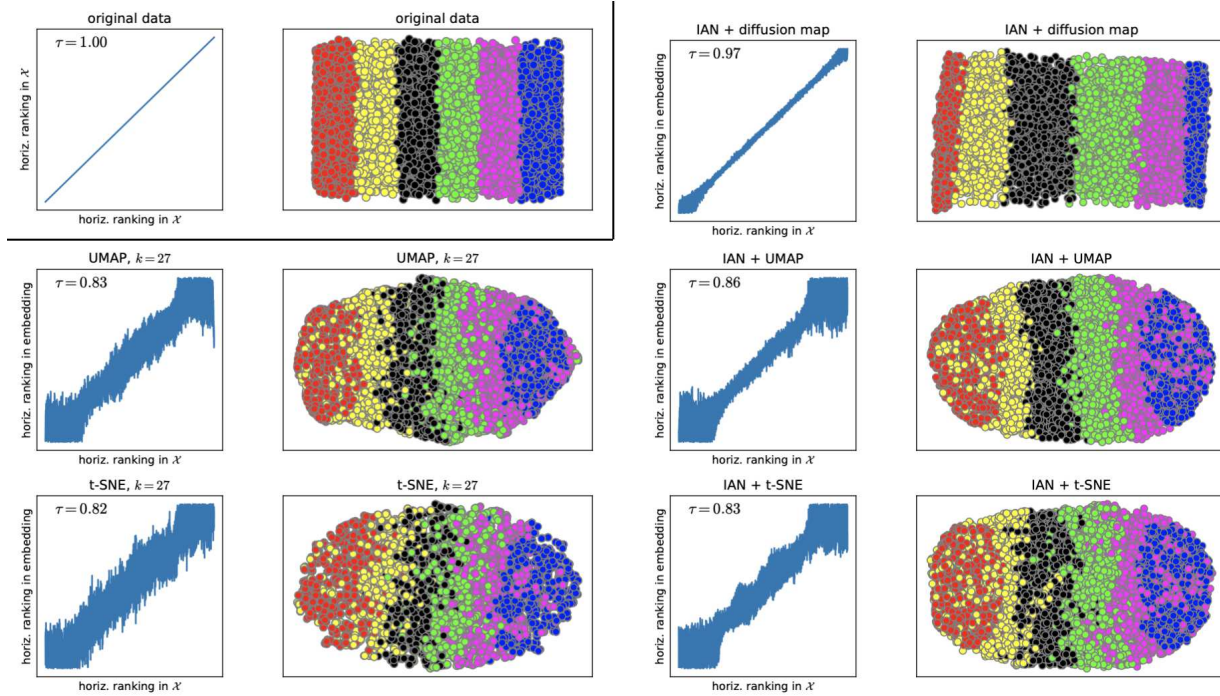


Figure 29: Performance of different embedding algorithms applied to a 5-dimensional cylinder ( $\mathbb{R}^1 \times S^4$ ) sampled uniformly at random ( $N = 8403$ , ambient space  $\mathbb{R}^6$ ). Top left: original data,  $\mathcal{X}$ , projected onto first 2 coordinates (points colored according to their position along the cylinder’s long axis). Other plots show embeddings using different kernels and/or algorithms. The resulting degree of mixing of the original color labels indicates the quality of the embedding scheme. A quantitative assessment (plots to the left of each embedding) was computed as the rank correlation coefficient,  $\tau$  (see main text), between the ranking (positional order) of each point along the horizontal axis in the original vs. embedded space (a value closer to 1 indicates fewer exchanges in the original order). Use of our IAN kernel produced similar or better results with both t-SNE and UMAP ( $k = 27$  was set as the mean degree in  $G^*$ , compatible with  $d = 5$ ). Diffusion maps resulted in very little mixing except near the boundaries.

## 4.2 Geodesic computation

From  $G^*$ , we can immediately compute graph geodesics (shortest paths using distances in ambient space as edge lengths) as an estimate of the true geodesics over  $\mathcal{M}$ [96]. The latter are likely to be underestimated when sampling is sparse[15], even when the graph connectivity is correct, e.g., due to curvature (see section 3.3.2), or when the neighborhood sizes are small (as in  $G^*$ , due to the minimality of neighborhood sizes obtained from the Gabriel connectivity rule, or in a  $k$ -NN graph with a tightly fit  $k$ ). It seems a good idea then to incorporate the continuous kernel values present in its weighted counterpart,  $\mathcal{G}^*$ , as means to improve geodesic estimation. Computing graph geodesics directly on  $\mathcal{G}^*$ , of course, cannot work, since it is a complete graph up to a numerical precision (or an arbitrary tolerance set for the weight values).

Instead, we propose to use the heat method for geodesic computation of [33]. It consists in solving the Poisson equation to find a function  $\phi$  whose gradient follows a unit vector field  $\mathbf{X}$  pointing along geodesics;  $\mathbf{X}$  can be obtained by normalizing the temperature gradient  $\nabla u$  due to a diffusion process in which heat  $u$  is allowed to diffuse for a short time. Although this method is tailored for applications where positional information and dimensionality are known (in particular, surfaces in  $\mathbb{R}^3$ ), here we apply it to  $\mathcal{G}^*$ , since discrete versions of the operators used (Laplacian, gradient, and divergence) can be readily defined on a weighted graph[35].

Despite being restricted to pairwise information, our method produces reasonable estimates, as shown in Figs. 30,31. To understand why, notice that the IAN algorithm indirectly solves for a weighted graph for which a random walk starting at node  $i$  has a higher probability of reaching a node in  $\mathcal{N}(i)$  than any other non-neighbor node. Given that random walks are closely related to diffusion over a graph, we should expect  $\mathcal{G}^*$  to be able to provide reasonable information about how a diffusion process propagates over  $\mathcal{M}$ . In other words, the Laplacian obtained from  $\mathcal{G}^*$  should be a good approximation of a continuous operator over  $\mathcal{M}$ ; this is empirically confirmed by our results.

In Fig. 30, heat geodesics computed from  $\mathcal{G}^*$  for the bent plane dataset approximate well the true geodesics over  $\mathcal{M}$ , and graph geodesics obtained from  $G^*$  follow closely. Comparison with those from a naive  $k$ -NN graph illustrates that the choice of  $k$  is critical (compare with bottom row of Fig. 28).

In Fig. 31, we compare the results using weighted graphs from various kernels on the stingray dataset; interestingly, heat geodesics computed from  $\mathcal{G}^*$  hold reasonably well even when facing a continuous change in dimensionality.

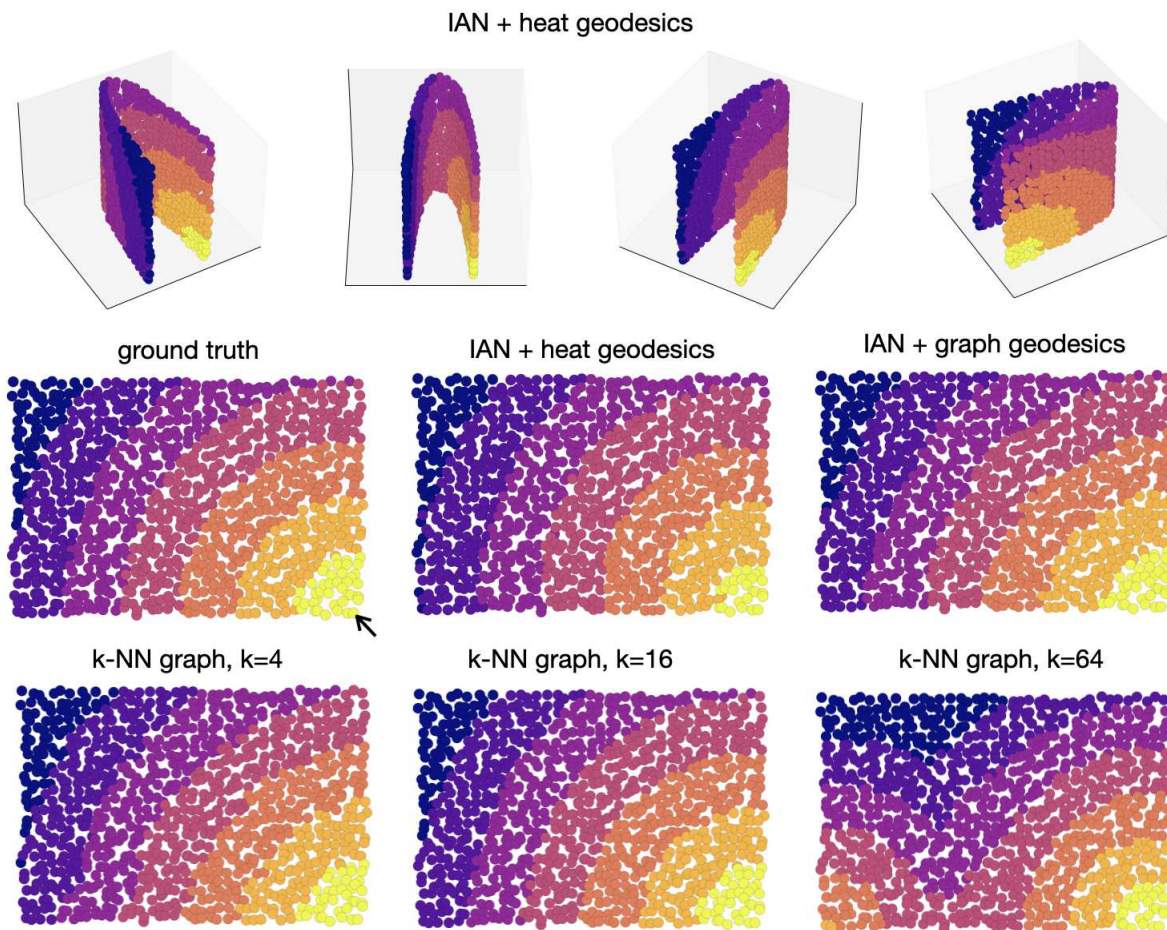


Figure 30: Geodesic estimation for the bent plane from Fig. 28; yellow points are closer to the source (marked with an arrow in the ground truth plot). *Top*: different views of the bent plane in 3-D, with points colored according to the heat geodesics computed from  $\mathcal{G}^*$ . *Middle*: Geodesics displayed on an unbent version of the dataset: heat geodesics approximate well the true geodesics over  $\mathcal{M}$ , and graph geodesics computed from  $G^*$  follow closely. *Bottom*: graph geodesics computed from  $k$ -NN graphs using different choices of  $k$ ; choosing  $k = 16$  gives near-perfect results, but  $k = 4$  shows distortions and  $k = 64$  misses completely.

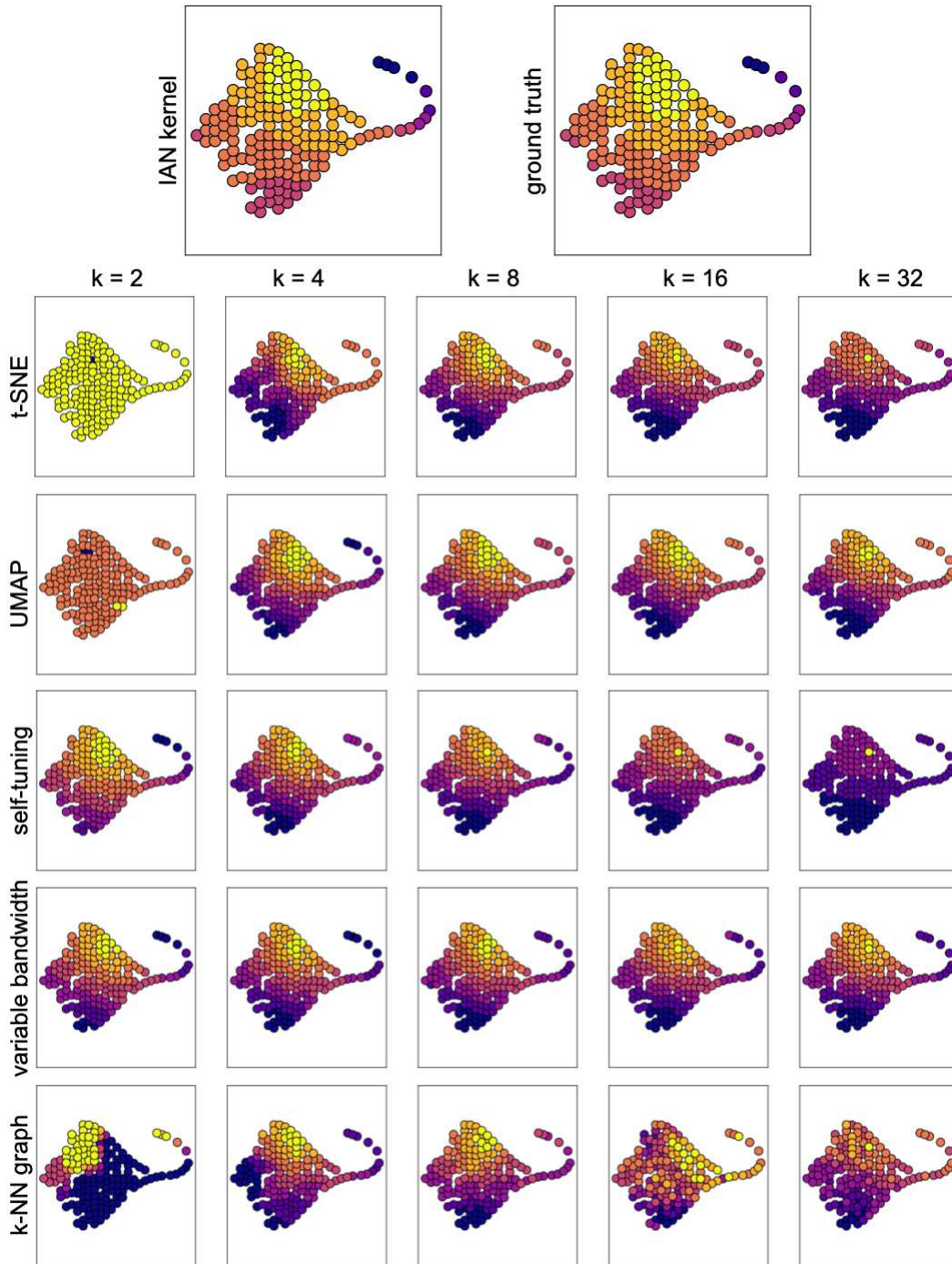


Figure 31: Geodesic estimation using the heat method applied to  $\mathcal{G}^*$  yields results close to the true geodesics (top). Other kernels yield suboptimal results for most choices of  $k$  (bottom); in particular, notice how the tip of the tail is usually inferred to be closer than it should (due to its being directly connected to the body in the underlying graph, cf. Fig. 24). Yellow points are closer to the source (marked with an arrow in the ground truth plot).

### 4.3 Local dimensionality estimation

Intrinsic dimensionality (ID) estimation is tightly associated with dimensionality reduction tasks, especially in manifold learning, where knowledge of  $d$  can help, among others, to determine the appropriate number of embedding dimensions.

There are many different ways to estimate it [24, 25]. Global approaches are typically divided into two. The first group are based on some variant of PCA (e.g., [48, 74]) and use the number of significant eigenvalues to infer dimensionality, and can be applied globally or by combining local estimates. The second group of methods, termed geometric (or fractal, when a non-integer ID is computed), exploit the geometric relationships in the data such as neighboring distances. Some are based on estimating packing numbers [59] or on distances to nearest-neighbors [104, 87, 99, 40, 18, 32]. Among the most popular are the *correlation dimension* methods [52, 26, 56], a variant of which has been specifically applied in the context of determining an appropriate kernel width for manifold learning [31, 16, 53]. The dimension is computed as the slope of a log-log plot of the number of neighboring points vs. neighborhood radius (see section 2.1). A recent variation is [62]. Others cover the difficult case of high ID [26, 90].

In our scenario, since we do not assume a pure manifold (section 3.1), we focus on local (i.e., pointwise) ID estimation approaches, namely those in which dimension is estimated within a neighborhood around each data point (e.g., [41, 55]). This notion can be formalized as the *local Hausdorff* dimension [110, 25], and a global estimate is typically found by averaging over local values.

A popular approach is Levina and Bickel’s maximum likelihood estimator (MLE) [71], which computes the local dimensionality based on  $k$ -nearest neighbors [71]:

$$\hat{m}_k(\mathbf{x}_i) = \left( \frac{1}{k-1} \sum_{j=1}^k \log \frac{T_k(\mathbf{x}_i)}{T_j(\mathbf{x}_i)} \right) \quad (41)$$

where  $T_j(x)$  denotes the distance between  $\mathbf{x}$  and its  $j^{\text{th}}$  nearest neighbor. We shall use this method in our experiments, in which we compute a final  $m_k(\mathbf{x}_i)$  by averaging  $\hat{m}_k(\mathbf{x}_i)$  over  $i$ ’s neighbors in order to reduce the variance of the local estimates (in the original, this is done over all data points). Notice that our kernel can be readily used with this method by simply replacing the  $k$ -NN graph with  $G^*$ , therefore summing over nodes in the neighborhood  $\mathcal{N}(i)$  instead of over the  $k$  nearest. Additionally, we propose a correlation dimension-based method that allows for local estimates. We describe it next, then compare its results with those from the MLE method.

#### 4.3.1 Algorithm: Neighborhood Correlation Dimension

Our proposed method is adapted from the approach used in [56] (also in [31, 53, 16]), where an estimate of correlation dimension is computed by using a general kernel. It consists in computing a curve  $Z(\sigma)$  over all pairwise kernel values (e.g., a Gaussian) at different values of the scale parameter  $\sigma$ :

$$Z = \sum_{i=1}^N \sum_{j=1}^N \exp \frac{-\|\mathbf{x}_i - \mathbf{x}_j\|^2}{2\sigma^2}. \quad (42)$$

As in [31] (and analogously to eqs. 31–29), by assuming that for small values of  $\sigma$  the manifold  $\mathcal{M}$  looks locally like its tangent space  $\mathbb{R}^d$ , we have

$$Z \approx \frac{N^2(\sqrt{2\pi}\sigma)^d}{\text{vol}^2(\mathcal{M})}, \quad (43)$$

which, after taking the logarithm, yields

$$\log Z \approx d \log \sigma + \log \frac{N^2(2\pi)^{d/2}}{\text{vol}(\mathcal{M})}, \quad (44)$$

so the slope of  $\log Z \times \log \sigma$  can be used to estimate of the global dimensionality of the manifold,  $d$ . To do so, one typically looks for a region where this slope is most stable, i.e., the curve is approximately linear. Automated ways of finding the slope of such a region are: by linear regression of the middle portion of the curve [56] or by taking a point of maximum of  $Z'(\sigma)$  [16, 53].

Because we assume intrinsic dimensionality may vary across  $\mathcal{M}$ , global averages cannot work in general. Moreover, nonuniform density, curvature, or multiple connected components may all create multiple peaks, so inspection of the log-log plot cannot be automated. Therefore, we modify this approach to use individual  $Z_i(\sigma)$  curves for each data point  $\mathbf{x}_i$ . To keep the summation local, points are restricted to those in the neighborhood of  $i$  in  $G^*$ . Here, it is advantageous to work with an extended neighborhood (e.g., by also including neighbors-of-neighbors) due to the theoretical limit to the value of the dimension  $d$  that can be accurately estimated given a set of  $N$  points[39], namely  $d < 2 \log_{10} N$ . In fact, if  $N$  is large compared to  $d$ , even additional hops away from  $i$  may be considered. Because such extension is done by following edges in  $G^*$  (as opposed to naively expanding a ball in  $\mathbb{R}^n$ ), we may thus obtain a larger (approximately tubular) neighborhood around  $\mathbf{x}_i$  without ever leaving the manifold. We denote such a neighborhood  $\mathcal{N}'(i)$ , as opposed to the immediate neighborhood  $\mathcal{N}(i)$ , both including  $i$  itself.

Our algorithm involves the following steps:

1. For each data point  $\mathbf{x}_i$  and its extended neighborhood  $\mathcal{N}'_i$ , define  $Z_i$  as

$$Z_i(\sigma) = \sum_{j \in |\mathcal{N}'(i)|} \exp \frac{-\|\mathbf{x}_i - \mathbf{x}_j\|^2}{2\sigma^2}. \quad (45)$$

2. Analogously to 44, by taking the logarithm we have that the slope of the  $\log Z_i \times \log \sigma$  curve,

$$Z'_i(\sigma) \stackrel{\text{def}}{=} \frac{d \log Z_i}{d \log \sigma}, \quad (46)$$

is an estimate of  $d_i$ , the dimension around  $\mathbf{x}_i$  as a function of  $\sigma$ . Computationally, it is desirable to use the closed-form expression, for accuracy:

$$Z'_i(\sigma) = \frac{\sum_{j=1}^{|\mathcal{N}'(i)|} \|\mathbf{x}_i - \mathbf{x}_j\|^2 \exp \frac{-\|\mathbf{x}_i - \mathbf{x}_j\|^2}{2\sigma^2}}{\sigma^2 \sum_{j=1}^{|\mathcal{N}'(i)|} \exp \frac{-\|\mathbf{x}_i - \mathbf{x}_j\|^2}{2\sigma^2}}. \quad (47)$$

3. A region of stability of  $Z'_i$ , i.e. a local maximum, is then an estimate of the apparent dimensionality around  $\mathbf{x}_i$ .

A local maximum (“peak”) in  $Z'_i(\sigma)$  means that, as a ball around  $\mathbf{x}_i$  is expanded, the rate at which neighbors are seen has stopped increasing and must decrease with larger  $\sigma$ , since no more neighbors can be found after the ball encompasses all points in  $\mathcal{N}'(i)$ . Intuitively,  $\mathcal{N}'(i)$  is sufficiently representative of the manifold around  $\mathbf{x}_i$ , i.e., if neighbors are approximately uniformly distributed and dimensionality is constant within it, then  $Z'_i$  should remain constant over some appreciable range of  $\sigma$ , whence the notion of ‘stability’.

Even though we work with a subset of  $\mathcal{X}$ , there may still be multiple maxima in  $Z'_i$ , e.g., when the neighbors of  $\mathbf{x}_i$  are far from uniformly distributed around it. So, operationally, we use the global maximum of  $Z'_i$ , since this takes into account the information given by the majority of neighboring points. Now, because  $Z_i \rightarrow 1$  as  $\sigma \rightarrow 0$ , and  $Z_i \rightarrow N$  as  $\sigma \rightarrow \infty$ , the slope of  $\log Z_i$  must be 0 at both extremes, thus the global maximum of  $Z'_i$  must also be a relative one (a “peak”).

We now proceed to avoid boundary effects by re-centering neighborhoods. The boundary  $\partial\mathcal{M}$  of a  $d$ -dimensional manifold (when present) has dimensionality  $d - 1$  [69]. The correlation integral approach often fails for these points—it typically returns  $d/2$  for points in  $\partial\mathcal{M}$ —since they tend to have half the number of neighbors as interior points. For the same reason, it also tends to underestimate  $d$  for points near the boundary. Since we work locally over a graph, we can regularize the computation by moving the focus to a nearby point (thereby regularizing over sampling artifacts as well):

4. Letting  $\mathcal{N}(i)$  be the set of adjacent nodes to  $i$  in  $G^*$  and including  $i$  itself, define  $\bar{l}$  as the node  $j \in \mathcal{N}(i)$  with smallest median squared distance to all points in the extended neighborhood  $\mathcal{N}'(i)$ :

$$\bar{l} = \operatorname{argmin}_{j \in \mathcal{N}(i)} \operatorname{median} \{ \|\mathbf{x}_j - \mathbf{x}_l\|^2, \forall l \in \mathcal{N}'(i) \}. \quad (48)$$

$\bar{l}$  is, in effect, the most central node in  $i$ ’s immediate neighborhood<sup>8</sup>.

5. Use  $\bar{l}$  as the point from which kernel values are computed for  $Z_i(\sigma)$  (replacing  $\mathbf{x}_i$  with  $\mathbf{x}_{\bar{l}}$  in eq. 45, thereby shifting the center of estimation of  $d_i$ . This assumes dimensionality does not change abruptly across neighboring points. Denote the resulting estimate  $\hat{d}'_i$ .

Finally, recall from section 3.5 that we also obtain a degree-based estimate,  $\tilde{d}_i$ , when computing volume ratios (eq. 36); we can use this information to further improve our results. A final estimate,  $d_i^*$  is obtained as follows:

6. As with the MLE method (section 4.3), we can obtain a smoother estimate  $\hat{d}'_i$  as the average over the estimates among immediate neighbors in  $\mathcal{N}(i)$ :

$$\hat{d}'_i = \frac{1}{|\mathcal{N}(i)|} \sum_{j \in \mathcal{N}(i)} \hat{d}'_j. \quad (49)$$

7. To avoid overestimating the true dimension, we compute an average  $\tilde{d}'_i$  over  $\mathcal{N}(i)$  as

$$\tilde{d}'_i = \frac{1}{|\mathcal{N}(i)|} \sum_{j \in \mathcal{N}(i)} \lfloor \tilde{d}_j \rfloor = \frac{1}{|\mathcal{N}(i)|} \sum_{j \in \mathcal{N}(i)} \lfloor \log_2 \deg(j) \rfloor. \quad (50)$$

---

<sup>8</sup>Since we know  $G^*$ , graph-theoretical quantities such as, e.g., shortest-path betweenness centrality [46, 22] can also be readily employed.

8. Compute the optimal estimate  $d_i^*$  as

$$d_i^* = \max \left\{ \hat{d}_i', \tilde{d}_i' \right\} \quad (51)$$

Application of this technique and comparison with other methods are given next.

### 4.3.2 Experimental results

Results of applying our neighborhood correlation dimension (NCD) algorithm compared to Levina and Bickel’s MLE estimator (eq. 41) are shown in Figs. 32–34. For NCD, we compared results using IAN *vs.* those from  $k$ -NN graphs with various values of  $k$  (a range was chosen that included the best results for each algorithm). The IAN kernel was applied by using the discrete neighborhoods of  $G^*$ , re-centered using neighbors-of-neighbors at most 3 hops away from  $i$  (eq. 48).

Using IAN, we obtained near-optimal results for the stingray and bent plane. For the 5-dimensional cylinder, dimensionality was underestimated (mean 4.6). Methods based on correlation dimension are known to underestimate the true  $d$  when the sample size is not sufficiently large[25]. In these cases, the method of [26] can be applied *a posteriori* to improve results.

For the MLE method, using large values of  $k$  tends to improve results, but only when dimensionality was constant (as in the bent plane and cylinder). For the stingray dataset, however, no value of  $k$  gave correct results; small values of  $k$  increase the estimates due to a bias, and large values tend to produce a uniform value throughout (thus giving better estimates only when  $d$  is constant). We found that computing the neighborhood averages using MacKay and Ghahramani’s correction (averaging the inverse of the estimators to reduce bias when  $k$  is small)[76] gave slightly better results. (We did not use the final smoothing procedure which involves choosing two additional neighborhood size parameters,  $k_1$  and  $k_2$ .)

Finally, we confirm these observations by testing two additional datasets with non-uniform dimensionality (Fig. 35). Again, while our algorithm achieves good results locally, there is no single value of  $k$  that allows MLE to find appropriate local estimates everywhere.



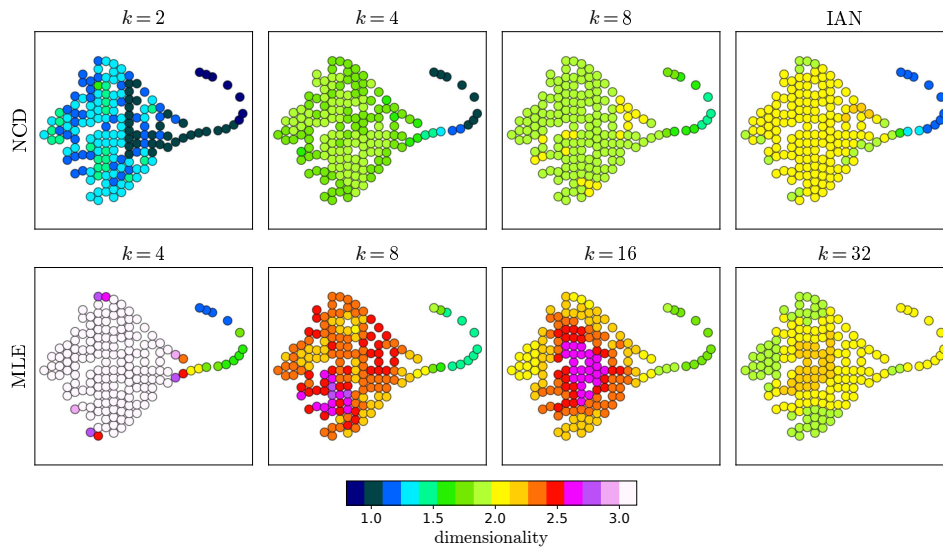


Figure 32: Estimation of local intrinsic dimensionality on the stingray dataset. Top row shows results for our neighborhood correlation dimension (NCD) algorithm using  $k$ -NN graphs for various  $k$  and using adaptive neighborhoods from  $G^*$  (IAN). Bottom row shows results using Levina and Bickel’s MLE estimator, which are quite sensitive to the choice of  $k$ : using a small value grossly overestimates the dimensionality over the body, and a large  $k$  ignores the geometry of the tail. With NCD using IAN gave the best results, estimated a dimension 2 for the body and 1 for the tail, with intermediate values for the transition tail/body and the boundary.

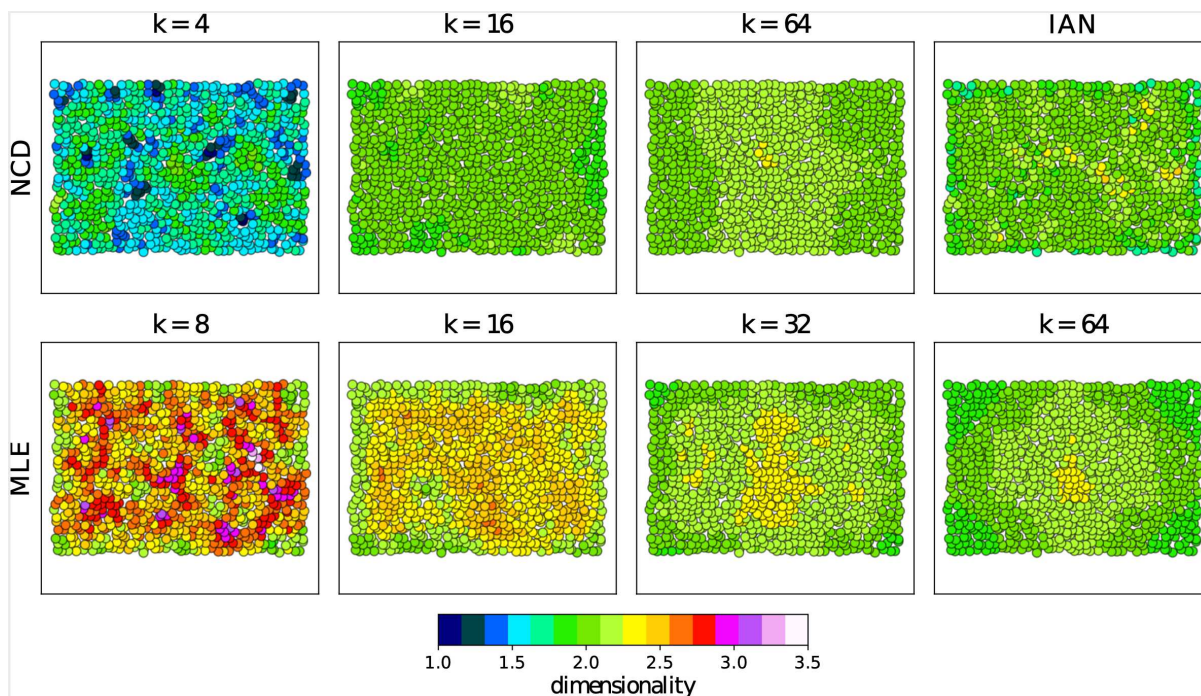


Figure 33: Estimation of local intrinsic dimensionality on the bent plane dataset (cf. Fig. 32). As with the stingray, results are sensitive to the choice of  $k$ , but here a wider range of values work due to the constant dimension. For NCD, results with IAN are comparable to those using the best  $k$ -NN graph ( $k = 16$ ). With MLE, larger  $k$  improved results (comparable to those from NCD).

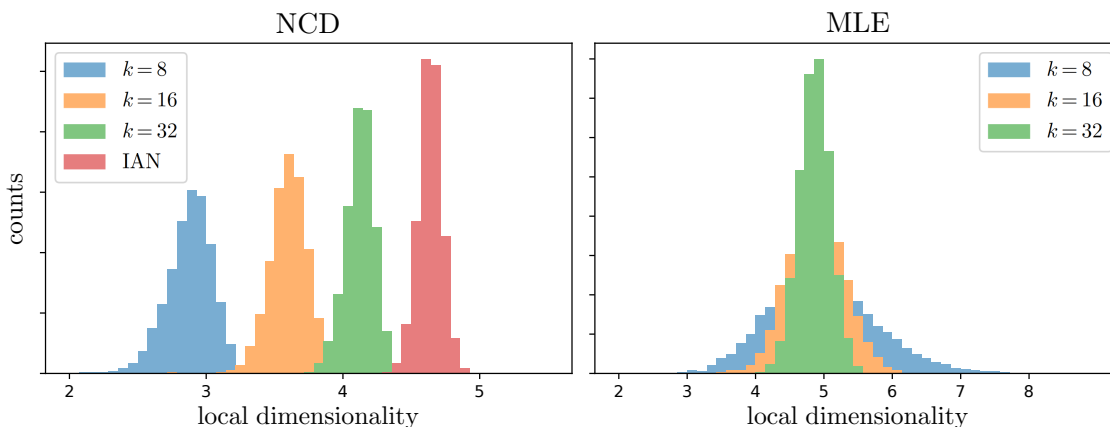


Figure 34: Estimation of local intrinsic dimensionality on the 5-D cylinder dataset (cf. Fig. 32). With NCD, results using IAN underestimated the true dimensionality (mean 4.63), but are still better than using a  $k$ -NN graph with arbitrary  $k$ . With MLE, larger values of  $k$  gave tighter distributions around the correct value (mean 4.86 for  $k = 32$ ).

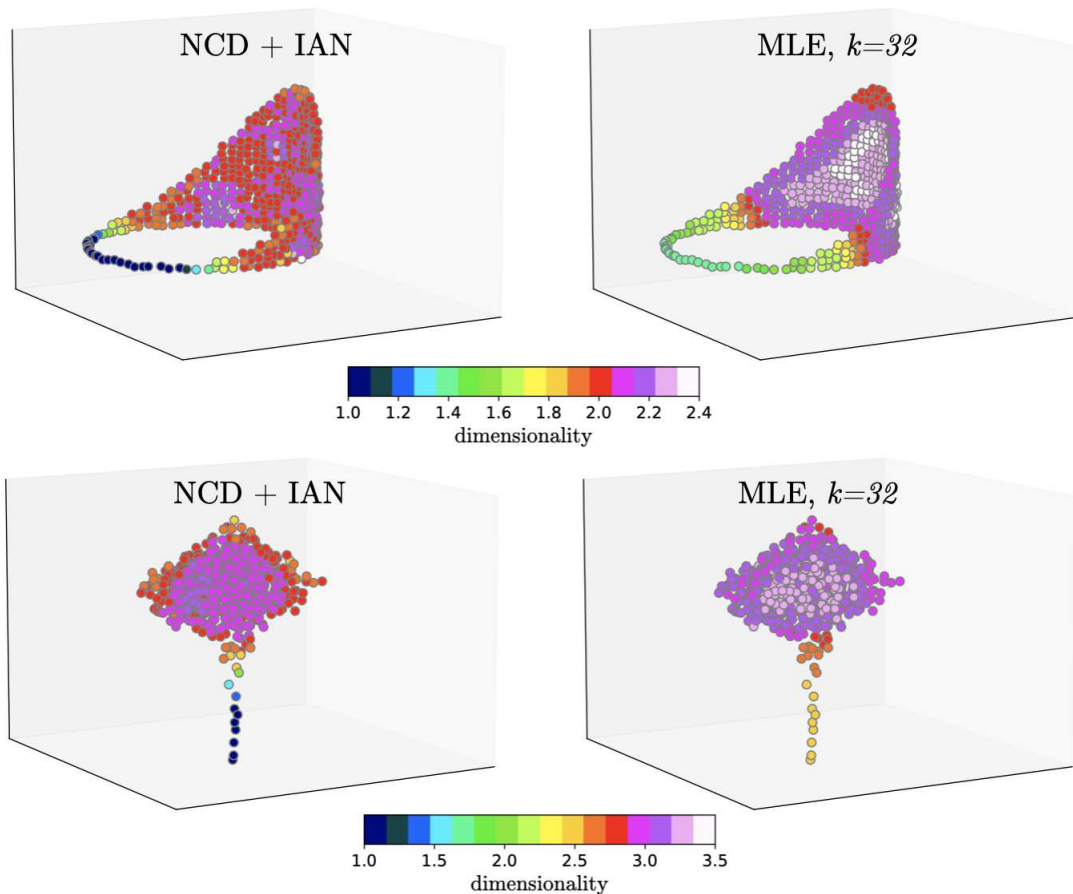


Figure 35: Dimensionality estimation for two datasets with non-uniform local  $d_i$ : a “tiara” (top row), where dimension varies smoothly from 2 to 1, and a “spinning top” (bottom row), where dimension goes from dimensionality reduces from 3 to 1 as one moves from the bulky part toward the tip. Using the optimal  $k$  for MLE cannot give good results for the entire data. Our NCD method, on the other hand, is able to correctly adapt to the local geometry by using the IAN kernel.

## 5 Summary and Conclusions

In theory, applying the manifold assumption requires knowing about the manifold: its geometry, topology, as well as how it was sampled. In practice, however, these manifold properties are rarely known. Instead, one typically applies a reasonable assumption, such as the dimension of the manifold is about  $d$  and therefore about  $k = 2^d$  nearest neighbors suffice. Thus many of the data graphs underlying manifold inference and non-linear dimensionality reduction are built. Since it is essentially impossible to remain completely agnostic, it is alright to choose a few values of  $k$  and choose among the results.

But this cannot work in general. Manifolds may not have a fixed dimension, they may be curved or with boundary, and sampling may vary. Finding a compromise  $k$  is, well, a compromise. We suggest a different tack: that one should build the nearest neighbor graph, and hence the graph-Laplacian approximation, in as data-driven a manner as possible. The number of neighbors, and hence the intrinsic dimensionality, may then vary across the data. A multi-scale approach is required.

Our algorithm of iterated adaptive neighborhoods (IAN) starts with an extremely conservative assumption: that nearest neighbors should have no ‘nearer’ neighbors between them. We alternate between a discrete and a continuous view of neighborhood graphs, and use a volumetric statistic to check for outliers. A linear program keeps the scales minimal while providing a global cover. This optimization is convex, so results are deterministic; other approaches, such as t-SNE, are stochastic so depend critically on the initialization.

Our multi-scale kernel has been applied successfully to a variety of datasets, and compared against many of the most popular algorithms available. In all cases our performance dominates. Furthermore, our multi-scale kernel can be incorporated directly into many of them, including diffusion maps, Isomap, UMAP, and t-SNE. In all of these cases performance is improved. Most of these algorithms involve many free parameters; we have none other than the robust requirement for an outlier.

Other algorithms (e.g. LLE) approximate the tangent space over a local neighborhood around each point. Although not explored here, using  $G^*$  to automatically provide such neighborhoods is straightforward (analogous to what was done in section 4.3 to estimate the local dimensionality). Applications to clustering need to be explored.

Our weighted graph has also been applied to geodesic estimation, achieving comparable results to those obtained from graph geodesics. In contrast, the graphs obtained from other similarity kernels produce less than optimal results.

Our unweighted graph has found application in local dimensionality estimation. Our proposed algorithm, neighborhood correlation dimension (NCD) takes advantage of the adaptive connectivity of our graphs in order to improve correlation dimension-based results, namely by restricting the correlation integral to an approximately tubular neighborhood around  $x_i$  in  $\mathcal{M}$ . As a result, we obtained accurate estimates of the local dimensionality in datasets where it is not uniform.

Much remains to be done. Several theoretical bounds are implied; these need to be proved. Multi-scale kernels, such as those from eqs. 6,7 have been shown to approximate Laplacian operators asymptotically[98, 17]. Using our application examples as evidence, we conjecture that our version also results in good approximations.

## References

- [1] Eddie Aamari, Jisu Kim, Frédéric Chazal, Bertrand Michel, Alessandro Rinaldo, and Larry Wasserman. Estimating the reach of a manifold. *Electronic journal of statistics*, 13(1):1359–1399, 2019.
- [2] Noga Alon, Shai Ben-David, Nicolo Cesa-Bianchi, and David Haussler. Scale-sensitive dimensions, uniform convergence, and learnability. *Journal of the ACM (JACM)*, 44(4):615–631, 1997.
- [3] Andrés Álvarez-Meza, Juliana Valencia-Aguirre, Genaro Daza-Santacoloma, and Germán Castellanos-Domínguez. Global and local choice of the number of nearest neighbors in locally linear embedding. *Pattern Recognition Letters*, 32(16):2171–2177, 2011.
- [4] Nina Amenta and Marshall Bern. Surface reconstruction by voronoi filtering. *Discrete & Computational Geometry*, 22(4):481–504, 1999.
- [5] Nina Amenta, Marshall Bern, and Manolis Kamvyselis. A new voronoi-based surface reconstruction algorithm. In *Proceedings of the 25th annual conference on Computer graphics and interactive techniques*, pages 415–421, 1998.
- [6] Sanjeev Arora, Wei Hu, and Pravesh K Kothari. An analysis of the t-sne algorithm for data visualization. In *Conference On Learning Theory*, pages 1455–1462. PMLR, 2018.
- [7] Sanjeev Arora and Ravi Kannan. Learning mixtures of separated nonspherical gaussians. *The Annals of Applied Probability*, 15(1A):69–92, 2005.
- [8] R. Banisch, E. H. Thiede, and Z. Trstanova. pydiffmap. <https://github.com/DiffusionMapsAcademics/pyDiffMap>, 2017.
- [9] Etienne Becht, Leland McInnes, John Healy, Charles-Antoine Dutertre, Immanuel WH Kwok, Lai Guan Ng, Florent Ginhoux, and Evan W Newell. Dimensionality reduction for visualizing single-cell data using UMAP. *Nature biotechnology*, 37(1):38–44, 2019.
- [10] Mikhail Belkin and Partha Niyogi. Laplacian eigenmaps for dimensionality reduction and data representation. *Neural computation*, 15(6):1373–1396, 2003.
- [11] Mikhail Belkin and Partha Niyogi. Semi-supervised learning on riemannian manifolds. *Machine learning*, 56(1):209–239, 2004.
- [12] Mikhail Belkin, Jian Sun, and Yusu Wang. Discrete laplace operator on meshed surfaces. In *Proceedings of the twenty-fourth annual symposium on Computational geometry*, pages 278–287, 2008.
- [13] Mikhail Belkin, Jian Sun, and Yusu Wang. Constructing laplace operator from point clouds in  $\mathbb{R}^d$ . In *Proceedings of the twentieth annual ACM-SIAM symposium on Discrete algorithms*, pages 1031–1040. SIAM, 2009.

- [14] Fausto Bernardini, Joshua Mittleman, Holly Rushmeier, Cláudio Silva, and Gabriel Taubin. The ball-pivoting algorithm for surface reconstruction. *IEEE transactions on visualization and computer graphics*, 5(4):349–359, 1999.
- [15] M Bernstein, V De Silva, JC Langford, and JB Tenenbaum. Graph approximations to geodesics on embedded manifolds (technical report), 2000.
- [16] Tyrus Berry, Dimitrios Giannakis, and John Harlim. Nonparametric forecasting of low-dimensional dynamical systems. *Physical Review E*, 91(3):032915, 2015.
- [17] Tyrus Berry and John Harlim. Variable bandwidth diffusion kernels. *Applied and Computational Harmonic Analysis*, 40(1):68–96, 2016.
- [18] Adam Block, Zeyu Jia, Yury Polyanskiy, and Alexander Rakhlin. Intrinsic dimension estimation. *Journal of Machine Learning Research*, 22:1–30, 2021.
- [19] Jean-Daniel Boissonnat, Leonidas J Guibas, and Steve Y Oudot. Manifold reconstruction in arbitrary dimensions using witness complexes. *Discrete & Computational Geometry*, 42(1):37–70, 2009.
- [20] Jean-Daniel Boissonnat, André Lieutier, and Mathijs Wintraecken. The reach, metric distortion, geodesic convexity and the variation of tangent spaces. *Journal of applied and computational topology*, 3(1):29–58, 2019.
- [21] Stephen Boyd, Stephen P Boyd, and Lieven Vandenbergh. *Convex optimization*. Cambridge university press, 2004.
- [22] Ulrik Brandes. A faster algorithm for betweenness centrality. *Journal of mathematical sociology*, 25(2):163–177, 2001.
- [23] Christoph Bregler and Stephen Omohundro. Nonlinear image interpolation using manifold learning. *Advances in neural information processing systems*, 7, 1994.
- [24] Francesco Camastra. Data dimensionality estimation methods: a survey. *Pattern recognition*, 36(12):2945–2954, 2003.
- [25] Francesco Camastra and Antonino Staiano. Intrinsic dimension estimation: Advances and open problems. *Information Sciences*, 328:26–41, 2016.
- [26] Francesco Camastra and Alessandro Vinciarelli. Estimating the intrinsic dimension of data with a fractal-based method. *IEEE Transactions on pattern analysis and machine intelligence*, 24(10):1404–1407, 2002.
- [27] David M Chan, Roshan Rao, Forrest Huang, and John F Canny. t-sne-cuda: Gpu-accelerated t-sne and its applications to modern data. In *2018 30th International Symposium on Computer Architecture and High Performance Computing (SBAC-PAD)*, pages 330–338. IEEE, 2018.
- [28] Ronald R Coifman and Stéphane Lafon. Diffusion maps. *Applied and computational harmonic analysis*, 21(1):5–30, 2006.

- [29] Ronald R Coifman, Stephane Lafon, Ann B Lee, Mauro Maggioni, Boaz Nadler, Frederick Warner, and Steven W Zucker. Geometric diffusions as a tool for harmonic analysis and structure definition of data: Diffusion maps. *Proceedings of the national academy of sciences*, 102(21):7426–7431, 2005.
- [30] Ronald R Coifman, Stephane Lafon, Ann B Lee, Mauro Maggioni, Boaz Nadler, Frederick Warner, and Steven W Zucker. Geometric diffusions as a tool for harmonic analysis and structure definition of data: Multiscale methods. *Proceedings of the National Academy of Sciences*, 102(21):7432–7437, 2005.
- [31] Ronald R Coifman, Yoel Shkolnisky, Fred J Sigworth, and Amit Singer. Graph laplacian tomography from unknown random projections. *IEEE Transactions on Image Processing*, 17(10):1891–1899, 2008.
- [32] Jose A Costa, Abhishek Girotra, and AO Hero. Estimating local intrinsic dimension with k-nearest neighbor graphs. In *IEEE/SP 13th Workshop on Statistical Signal Processing, 2005*, pages 417–422. IEEE, 2005.
- [33] Keenan Crane, Clarisse Weischedel, and Max Wardetzky. Geodesics in heat: A new approach to computing distance based on heat flow. *ACM Transactions on Graphics (TOG)*, 32(5):1–11, 2013.
- [34] Sanjoy Dasgupta. Learning mixtures of gaussians. In *40th Annual Symposium on Foundations of Computer Science (Cat. No. 99CB37039)*, pages 634–644. IEEE, 1999.
- [35] Xavier Desquesnes, Abderrahim Elmoataz, and Olivier Lézoray. Eikonal equation adaptation on weighted graphs: fast geometric diffusion process for local and non-local image and data processing. *Journal of Mathematical Imaging and Vision*, 46(2):238–257, 2013.
- [36] George Dimitriadis, Joana P Neto, and Adam R Kampff. t-sne visualization of large-scale neural recordings. *Neural computation*, 30(7):1750–1774, 2018.
- [37] David L Donoho and Carrie Grimes. Hessian eigenmaps: Locally linear embedding techniques for high-dimensional data. *Proceedings of the National Academy of Sciences*, 100(10):5591–5596, 2003.
- [38] Ramsay Dyer, Hao Zhang, and Torsten Möller. Gabriel meshes and delaunay edge flips. In *2009 SIAM/ACM Joint Conference on Geometric and Physical Modeling*, pages 295–300, 2009.
- [39] J-P Eckmann and David Ruelle. Fundamental limitations for estimating dimensions and lyapunov exponents in dynamical systems. *Physica D: Nonlinear Phenomena*, 56(2-3):185–187, 1992.
- [40] Elena Facco, Maria d’Errico, Alex Rodriguez, and Alessandro Laio. Estimating the intrinsic dimension of datasets by a minimal neighborhood information. *Scientific reports*, 7(1):1–8, 2017.

- [41] Amir Massoud Farahmand, Csaba Szepesvári, and Jean-Yves Audibert. Manifold-adaptive dimension estimation. In *Proceedings of the 24th international conference on Machine learning*, pages 265–272, 2007.
- [42] Herbert Federer. Curvature measures. *Transactions of the American Mathematical Society*, 93(3):418–491, 1959.
- [43] Charles Fefferman, Sergei Ivanov, Yaroslav Kurylev, Matti Lassas, and Hariharan Narayanan. Fitting a putative manifold to noisy data. In *Proceedings of the 31st Conference On Learning Theory*, volume 75, pages 688–720. PMLR, 2018.
- [44] Charles Fefferman, Sanjoy Mitter, and Hariharan Narayanan. Testing the manifold hypothesis. *Journal of the American Mathematical Society*, 29(4):983–1049, 2016.
- [45] Steven Fortune. Voronoi diagrams and delaunay triangulations. *Computing in Euclidean geometry*, pages 225–265, 1995.
- [46] Linton C Freeman. A set of measures of centrality based on betweenness. *Sociometry*, pages 35–41, 1977.
- [47] Yasuhiro Fujiwara, Yasutoshi Ida, Sekitoshi Kanai, Atsutoshi Kumagai, and Naonori Ueda. Fast similarity computation for t-sne. In *2021 IEEE 37th International Conference on Data Engineering (ICDE)*, pages 1691–1702. IEEE, 2021.
- [48] Keinosuke Fukunaga and David R Olsen. An algorithm for finding intrinsic dimensionality of data. *IEEE Transactions on Computers*, 100(2):176–183, 1971.
- [49] K Ruben Gabriel and Robert R Sokal. A new statistical approach to geographic variation analysis. *Systematic zoology*, 18(3):259–278, 1969.
- [50] Christopher Genovese, Marco Perone-Pacífico, Isabella Verdinelli, and Larry Wasserman. Minimax manifold estimation. *Journal of Machine Learning Research*, 13(43):1263–1291, 2012.
- [51] Yair Goldberg and Ya’acov Ritov. Local procrustes for manifold embedding: a measure of embedding quality and embedding algorithms. *Machine learning*, 77(1):1–25, 2009.
- [52] Peter Grassberger and Itamar Procaccia. Measuring the strangeness of strange attractors. In *The theory of chaotic attractors*, pages 170–189. Springer, 2004.
- [53] Laleh Haghverdi, Florian Buettner, and Fabian J Theis. Diffusion maps for high-dimensional single-cell analysis of differentiation data. *Bioinformatics*, 31(18):2989–2998, 2015.
- [54] Gloria Haro, Gregory Randall, and Guillermo Sapiro. Translated poisson mixture model for stratification learning. *International Journal of Computer Vision*, 80(3):358–374, 2008.
- [55] Jinrong He, Lixin Ding, Lei Jiang, Zhaokui Li, and Qinghui Hu. Intrinsic dimensionality estimation based on manifold assumption. *Journal of Visual Communication and Image Representation*, 25(5):740–747, 2014.



- [56] Matthias Hein and Jean-Yves Audibert. Intrinsic dimensionality estimation of submanifolds in  $\mathbb{R}^d$ . In *Proceedings of the 22nd international conference on Machine learning*, pages 289–296, 2005.
- [57] Matthias Hein and Markus Maier. Manifold denoising. *Advances in neural information processing systems*, 19, 2006.
- [58] Geoffrey E Hinton and Sam Roweis. Stochastic neighbor embedding. *Advances in neural information processing systems*, 15, 2002.
- [59] Balázs Kégl. Intrinsic dimension estimation using packing numbers. *Advances in neural information processing systems*, 15, 2002.
- [60] Yosi Keller, Ronald R Coifman, Stéphane Lafon, and Steven W Zucker. Audio-visual group recognition using diffusion maps. *IEEE Transactions on Signal Processing*, 58(1):403–413, 2009.
- [61] Maurice George Kendall. *Rank correlation methods*. Griffin, 1948.
- [62] Matthäus Kleindessner and Ulrike Luxburg. Dimensionality estimation without distances. In *Artificial Intelligence and Statistics*, pages 471–479. PMLR, 2015.
- [63] William R Knight. A computer method for calculating kendall’s tau with ungrouped data. *Journal of the American Statistical Association*, 61(314):436–439, 1966.
- [64] Dmitry Kobak and Philipp Berens. The art of using t-SNE for single-cell transcriptomics. *Nature communications*, 10(1):1–14, 2019.
- [65] Dmitry Kobak and George C Linderman. Initialization is critical for preserving global data structure in both t-sne and umap. *Nature biotechnology*, 39(2):156–157, 2021.
- [66] Olga Kouropteva, Oleg Okun, and Matti Pietikäinen. Selection of the optimal parameter value for the locally linear embedding algorithm. *FSKD*, 2:359–363, 2002.
- [67] Stéphane Lafon. *Diffusion maps and geometric harmonics*. PhD thesis, Yale University, 2004.
- [68] Stéphane Lafon, Yosi Keller, and Ronald R Coifman. Data fusion and multicue data matching by diffusion maps. *IEEE Transactions on pattern analysis and machine intelligence*, 28(11):1784–1797, 2006.
- [69] John Lee. *Introduction to topological manifolds*, volume 202. Springer Science & Business Media, 2010.
- [70] John A Lee and Michel Verleysen. *Nonlinear dimensionality reduction*, volume 1. Springer, 2007.
- [71] Elizaveta Levina and Peter Bickel. Maximum likelihood estimation of intrinsic dimension. *Advances in neural information processing systems*, 17, 2004.

- [72] Ofir Lindenbaum, Moshe Salhov, Arie Yeredor, and Amir Averbuch. Gaussian bandwidth selection for manifold learning and classification. *Data mining and knowledge discovery*, 34(6):1676–1712, 2020.
- [73] George C Linderman, Manas Rachh, Jeremy G Hoskins, Stefan Steinerberger, and Yuval Kluger. Fast interpolation-based t-sne for improved visualization of single-cell rna-seq data. *Nature methods*, 16(3):243–245, 2019.
- [74] Anna V Little, Mauro Maggioni, and Lorenzo Rosasco. Multiscale geometric methods for data sets i: Multiscale svd, noise and curvature. *Applied and Computational Harmonic Analysis*, 43(3):504–567, 2017.
- [75] László Lovász. Discrete and continuous: two sides of the same? In *Visions in mathematics*, pages 359–382. Springer, 2010.
- [76] David JC MacKay and Zoubin Ghahramani. Comments on ‘maximum likelihood estimation of intrinsic dimension’ by e. levina and p. bickel (2005). *The Inference Group Website, Cavendish Laboratory, Cambridge University*, 2005.
- [77] David W Matula and Robert R Sokal. Properties of gabriel graphs relevant to geographic variation research and the clustering of points in the plane. *Geographical analysis*, 12(3):205–222, 1980.
- [78] Leland McInnes, John Healy, and James Melville. UMAP: Uniform manifold approximation and projection for dimension reduction, 2018.
- [79] Nathan Mekuz and John K Tsotsos. Parameterless isomap with adaptive neighborhood selection. In *Joint Pattern Recognition Symposium*, pages 364–373. Springer, 2006.
- [80] Gal Mishne and Israel Cohen. Multiscale anomaly detection using diffusion maps. *IEEE Journal of selected topics in signal processing*, 7(1):111–123, 2012.
- [81] Kevin R Moon, David van Dijk, Zheng Wang, Scott Gigante, Daniel B Burkhardt, William S Chen, Kristina Yim, Antonia van den Elzen, Matthew J Hirn, Ronald R Coifman, et al. Visualizing structure and transitions in high-dimensional biological data. *Nature biotechnology*, 37(12):1482–1492, 2019.
- [82] Hariharan Narayanan and Sanjoy Mitter. Sample complexity of testing the manifold hypothesis. *Advances in neural information processing systems*, 23, 2010.
- [83] Partha Niyogi, Stephen Smale, and Shmuel Weinberger. Finding the homology of submanifolds with high confidence from random samples. *Discrete & Computational Geometry*, 39(1):419–441, 2008.
- [84] Partha Niyogi, Stephen Smale, and Shmuel Weinberger. A topological view of unsupervised learning from noisy data. *SIAM Journal on Computing*, 40(3):646–663, 2011.
- [85] F. Noé, R. Banisch, and C. Clementi. Commute maps: separating slowly mixing molecular configurations for kinetic modeling. *Journal of chemical theory and computation*, 12(11):5620–5630, 2016.

- [86] F. Pedregosa, G. Varoquaux, A. Gramfort, V. Michel, B. Thirion, O. Grisel, M. Blondel, P. Prettenhofer, R. Weiss, V. Dubourg, J. Vanderplas, A. Passos, D. Cournapeau, M. Brucher, M. Perrot, and E. Duchesnay. Scikit-learn: Machine learning in Python. *Journal of Machine Learning Research*, 12:2825–2830, 2011.
- [87] Karl W Pettis, Thomas A Bailey, Anil K Jain, and Richard C Dubes. An intrinsic dimensionality estimator from near-neighbor information. *IEEE Transactions on pattern analysis and machine intelligence*, 1(1):25–37, 1979.
- [88] Sam Roweis, Lawrence Saul, and Geoffrey E Hinton. Global coordination of local linear models. *Advances in neural information processing systems*, 14, 2001.
- [89] Sam T Roweis and Lawrence K Saul. Nonlinear dimensionality reduction by locally linear embedding. *science*, 290(5500):2323–2326, 2000.
- [90] Alessandro Rozza, Gabriele Lombardi, Claudio Ceruti, Elena Casiraghi, and Paola Campadelli. Novel high intrinsic dimensionality estimators. *Machine learning*, 89(1):37–65, 2012.
- [91] Marco Saerens, Francois Fouss, Luh Yen, and Pierre Dupont. The principal components analysis of a graph, and its relationships to spectral clustering. In *European conference on machine learning*, pages 371–383. Springer, 2004.
- [92] Oksana Samko, A David Marshall, and Paul L Rosin. Selection of the optimal parameter value for the Isomap algorithm. *Pattern Recognition Letters*, 27(9):968–979, 2006.
- [93] Lawrence K Saul, Kilian Q Weinberger, Fei Sha, Jihun Ham, and Daniel D Lee. Spectral methods for dimensionality reduction. *Semi-supervised learning*, 3, 2006.
- [94] Daniel Spielman. Spectral graph theory. *Combinatorial scientific computing*, 18, 2012.
- [95] Jian Tang, Jingzhou Liu, Ming Zhang, and Qiaozhu Mei. Visualizing large-scale and high-dimensional data. In *Proceedings of the 25th international conference on world wide web*, pages 287–297, 2016.
- [96] Joshua B Tenenbaum, Vin De Silva, and John C Langford. A global geometric framework for nonlinear dimensionality reduction. *science*, 290(5500):2319–2323, 2000.
- [97] Christoph Thäle. 50 years sets with positive reach—a survey. *Surveys in Mathematics and its Applications*, 3:123–165, 2008.
- [98] Daniel Ting, Ling Huang, and Michael I. Jordan. An analysis of the convergence of graph laplacians. In *Proceedings of the 27th International Conference on International Conference on Machine Learning*, ICML’10, page 1079–1086, Madison, WI, USA, 2010. Omnipress.
- [99] Gerard V Trunk. Statistical estimation of the intrinsic dimensionality of a noisy signal collection. *IEEE Transactions on Computers*, 100(2):165–171, 1976.
- [100] Laurens Van Der Maaten. Accelerating t-sne using tree-based algorithms. *The Journal of Machine Learning Research*, 15(1):3221–3245, 2014.

- [101] Laurens Van der Maaten and Geoffrey Hinton. Visualizing data using t-sne. *Journal of machine learning research*, 9(11), 2008.
- [102] Laurens van der Maaten, Eric Postma, and Jaap van den Herik. Dimensionality reduction: a comparative review. *J Mach Learn Res*, 10(66-71):13, 2009.
- [103] Santosh Vempala and Grant Wang. A spectral algorithm for learning mixture models. *Journal of Computer and System Sciences*, 68(4):841–860, 2004.
- [104] Peter J. Verwee and Robert P. W. Duin. An evaluation of intrinsic dimensionality estimators. *IEEE Transactions on pattern analysis and machine intelligence*, 17(1):81–86, 1995.
- [105] Xiang Wan, Wenqian Wang, Jiming Liu, and Tiejun Tong. Estimating the sample mean and standard deviation from the sample size, median, range and/or interquartile range. *BMC medical research methodology*, 14(1):1–13, 2014.
- [106] Jing Wang, Zhenyue Zhang, and Hongyuan Zha. Adaptive manifold learning. *Advances in neural information processing systems*, 17, 2004.
- [107] Yingfan Wang, Haiyang Huang, Cynthia Rudin, and Yaron Shaposhnik. Understanding how dimension reduction tools work: An empirical approach to deciphering t-sne, umap, trimap, and pacmap for data visualization. *J. Mach. Learn. Res.*, 22(201):1–73, 2021.
- [108] Martin Wattenberg, Fernanda Viégas, and Ian Johnson. How to use t-SNE effectively. *Distill*, 1(10):e2, 2016.
- [109] Kilian Q Weinberger and Lawrence K Saul. Unsupervised learning of image manifolds by semidefinite programming. *International journal of computer vision*, 70(1):77–90, 2006.
- [110] Lai-Sang Young. Dimension, entropy and lyapunov exponents. *Ergodic theory and dynamical systems*, 2(1):109–124, 1982.
- [111] Lihi Zelnik-Manor and Pietro Perona. Self-tuning spectral clustering. In *Proceedings of the 17th International Conference on Neural Information Processing Systems, NIPS’04*, page 1601–1608, Cambridge, MA, USA, 2004. MIT Press.
- [112] Zhenyue Zhang and Hongyuan Zha. Principal manifolds and nonlinear dimensionality reduction via tangent space alignment. *SIAM journal on scientific computing*, 26(1):313–338, 2004.

## A Greedy splitting

As an alternative to the optimization from section 3.4 (which can be expensive when the number of edges in  $G$  is very large, mainly due to large  $d$ ), we developed a greedy approach in which we assign scales that “ $C$ -cover” each edge  $e_{ij}$  in decreasing order of length  $r_{ij}$  (the Euclidean distance between  $\mathbf{x}_i$  and  $\mathbf{x}_j$  in  $\mathbb{R}^n$ ).

Starting with the edge  $e_{ij}$  with largest  $r_{ij}$ , set  $\sigma_i = \sigma_j = Cr_{ij}$ , thereby satisfying  $\sigma_i\sigma_j = (Cr_{ij})^2$  (we say  $Cr_{ij}$  is evenly “split” between  $\sigma_i$  and  $\sigma_j$ ). Moreover, since  $r_{ij} \leq \max\{r_i^{\text{FN}}, r_j^{\text{FN}}\}$ , we know the constraints  $\sigma_i \leq r_i^{\text{FN}}$  and  $\sigma_j \leq r_j^{\text{FN}}$  are also satisfied.

Continue with the edge  $e_{ij}$  with the next largest distance,  $r_{ij}$ . Here we are met with 3 possible cases in which a (re)assignment of scales is needed:

1. if neither of the nodes have been assigned a scale yet, evenly split scales as above;
2. if one of the nodes does not have a scale yet (wlog, let that node be  $j$ ), set  $\sigma'_j$  to the minimum scale that ensures  $\sigma_i\sigma'_j \geq (Cr_{ij})^2$ , i.e.,  $\sigma'_j = (Cr_{ij})^2/\sigma_i$ ;
3. if both nodes have previously been assigned a scale but  $e_{ij}$  is not covered by the current values of  $\sigma_i$  and  $\sigma_j$ , then set the quotient  $a = \frac{Cr_{ij}}{\sqrt{\sigma_i\sigma_j}}$  and update the scales:  $\sigma'_i = a\sigma_i$  and  $\sigma'_j = a\sigma_j$  thereby evenly splitting the quotient between the two nodes.

After cases (2) and (3), the updated scales might need to be “re-balanced” in order to meet the constraints  $\sigma'_i \leq r_i^{\text{FN}}$  and  $\sigma'_j \leq r_j^{\text{FN}}$ . Wlog, let  $\sigma'_i > r_i^{\text{FN}}$ . Then, we set  $\sigma''_i > r_i^{\text{FN}}$  and  $\sigma''_j = \sigma'_j \frac{\sigma'_i}{\sigma''_i}$ . Only one of the two scales may exceed its upper bounds: in (2) this is trivially true since only the newly-assigned scale may be greater than  $Cr_{ij}$ ; in (3), since both  $\sigma_i$  and  $\sigma_j$  have been previously assigned, we have  $\sigma_i \leq r_i^{\text{FN}}$  and  $\sigma_j \leq r_j^{\text{FN}}$ , as well as  $r_{ij} \leq r_i^{\text{FN}}$  and  $r_{ij} \leq r_j^{\text{FN}}$ , so therefore it must be the case that  $r_i^{\text{FN}}r_j^{\text{FN}} \geq r_{ij}^2 = \sigma'_i\sigma'_j$ . Note that, as a corollary, both scales must meet their respective constraints after being re-balanced as above.

This is repeated until all edges have been visited. The idea is that, by covering the largest edges first, we assign the largest, most constrained scales first, allowing for the later, less constrained scales, to be as small as possible. Because this tends to equally “split” the scaled edge lengths  $Cr_{ij}$  two scales  $\sigma_i$  and  $\sigma_j$ , it produces reasonable but usually sub-optimal results.